

# Spectroscopic Studies of $\text{N}_2\text{O}$ and $\text{HNO}_4$ : A Window into the Global Biogeochemistry of Nitrogen

Thesis by  
Hui Zhang

In Partial Fulfillment of the Requirements  
for the Degree of  
Doctor of Philosophy



California Institute of Technology  
Pasadena, California

2001

(Submitted June 21<sup>st</sup>, 2000)

© 2001

Hui Zhang

All Rights Reserved

*To my parents and my family,  
for their love and every gift to me.*

## Acknowledgements

I am indebted to many people during my years at Caltech. My dual advisors, Geoff Blake and Paul Wennberg, have provided a unique environment for my learning and growth. Geoff's never-subdued enthusiasm for new ideas and new technology, and Paul's critical thoughtfulness will continue to influence my professional development. I greatly appreciate their help in putting my diverse investigations into a coherent thesis, as well as the personal touches they have shared with me from time to time.

A few other people deserve special notice for making this thesis a reality. I thank Stan Sander for his encouragement and the opportunity to perform my initial work on PNA at JPL. Coleen Roehl has not only shared with me her experimental expertise but also the value of keeping in touch with others. Thom Rahn, Martin Wahlen and Dave Griffith, thank you for the collaboration on the  $N_2O$  isotope work. I want to mention David Rodham because he served as my first mentor for working in the lab. His attention to details has substantially influenced me as an experimentalist. Finishing this thesis would have been impossible without the excellent technical assistance from our machine, electrical and glass shops. I sincerely thank Guy Duremburg (I still remember the tricks you showed me on the mills), Mike Roy and Ray Garcia from Chemistry, Vic Nenow and Stan Cincera from Geology and Rick Gerhart from Biology. They not only have helped me make the parts I needed but also taught me many design considerations. Mike Black, the system administrator in GPS, is greatly appreciated for coming to my rescue on many computer questions over all these years.

As a member of both the Blake and Wennberg groups, I am very fortunate to not only have access to a great deal of talent and help for my thesis projects, but also having the luxury of enjoying the different cultures and social outings of the two groups. To the old Blake gang, Pin Chen, Shuji Matsuura, Sheng Wu, Zulf Morbi and Zifu Wang, when will we eat together again (yes, our big appetite)? To the youthful, Vadym Kapinus (lost in Alhambra) and Brian Meehan (ride to "Dirty" Palace), my best wishes. During my last two years, I had the opportunity to share a lab with two postdocs in the Wennberg group, Karena McKinney and Suresh Dhanyala. Thank you for answering all my questions and

bearing with it when I had to keep my side of the lab in the dark and turn on the noisy Neslab. Lunch with you at the bagel place and that Mexican restaurant has always been a pleasant walk under the sun.

I have always appreciated the openness and friendship from people I encountered as an international student in the U.S. I have great memories of Kay Campbell, Donna Sackett and Andy Ingersoll, showing me around on my first day at Caltech. Thank you, Anthony Toigo for the trip to Huntington Library and Jean Hsieh for pointing out what was what on my first Mexican dinner plate. My appreciation to Yuk and Shao-Mei Yung for opening their house every Thanksgiving, and the really yummy food. Jackie Kessler and Ulyana Dyudina, I will remember, fondly, our laughs in the office as well as those by the swimming pool. Aude, I wish you a happy life somewhere on the other side of the Atlantic and hope that someday our paths will cross again. Jing (and little Carisa), Lijie and Kate (Mom of three), I am sure we will keep in close contact with each other.

My special appreciation goes to Prof. John Baldeschwieler, whose class has inspired me to explore a fulfilling career in industry. His encouragement has made me brave enough to take this rather unusual but exciting path for a GPS graduate.

Finally, my parents deserve all of the credit for every little accomplishment I have ever aspired to. The curiosity, determination and free spirit they instilled in me are the ultimate drive for every endeavor I take in my life. I also have the deepest love for my elder sister, Chun, who is always at the other end of the string as my journey takes me further and further away from home. She has simply given me so much more than I could ever possibly give her back. With that, I dedicate this thesis to my parents and my family.

## Abstract

Nitrogen is an essential nutrient for all living organisms. This thesis focuses on the spectroscopic studies of two species that participate in the global biogeochemical cycle of nitrogen:  $\text{N}_2\text{O}$  and  $\text{HNO}_4$ . Both play important roles in the radiative and chemical processes in the terrestrial atmosphere.

In terms of experimental instrumentation, this thesis takes great advantage of the recent advances in both Optical Parametric Oscillator (OPO) and high power, narrow-linewidth pulsed laser technology. Chapter 1 describes a  $\beta\text{-BaB}_2\text{O}_4$  (BBO) OPO pumped by a high repetition rate Nd:YAG laser (Coherent Infinity<sup>TM</sup>). This combination provides a unique light source with wide tunability and high average output power, making it ideally suited for the photochemical and spectroscopic studies carried out in this thesis.

$\text{N}_2\text{O}$  is a prominent greenhouse gas and the major natural source of NO that initiates the catalytic  $\text{NO}_x$  ozone destruction cycles in the stratosphere. It has been suggested (Yung and Miller 1997, *Science* **78**, 1778, referred to as YM97 hereafter) that  $\text{N}_2\text{O}$  should be isotopically fractionated as a result of photolysis in the upper atmosphere, which represents the primary sink of  $\text{N}_2\text{O}$ . Chapter 2 studies the photolytic fractionation of  $\text{N}_2\text{O}$  in an attempt to test the YM97 model. These measurements have consistently shown large heavy enrichment of the residual  $\text{N}_2\text{O}$  isotopomers. The magnitude of the observed fractionation, however, is significantly larger than predicted but in accord with the sizable fractionation observed in the stratosphere. An attempt to reconcile the differences is given which notes the existence of vibrationally “hot”  $\text{N}_2\text{O}$  molecules at room temperature and the possible involvement of more than two electronic states in the photolysis. A fully quantitative test of YM97 theory will require accurate wavelength and temperature dependent differential cross sections for each of the  $\text{N}_2\text{O}$  isotopomers that are not yet available.

$\text{HNO}_4$  is an important reservoir species coupling the  $\text{HO}_x$  and  $\text{NO}_x$  families in the upper troposphere and lower stratosphere. Chapter 3 investigates the cleavage of the  $\text{HOO-NO}_2$  bond in  $\text{HNO}_4$  via absorption of red/near infrared (NIR) solar radiation. Experiments are designed to determine the cross sections and quantum yields for gas phase  $\text{HNO}_4$  photodissociation.  $\text{HNO}_4$  is found to dissociate at wavelengths as long as 1600 nm. It is argued

that molecular internal energy available for thermal excitation in addition to the photon energy can explain the observed dissociation of  $\text{HNO}_4$  beyond its thermodynamic dissociation threshold. Accordingly, a temperature-dependent quantum yield is predicted. The 1<sup>st</sup> OH stretching overtone is found to be partially dissociative. Because it is significantly brighter than the 2<sup>nd</sup> overtone, it contributes significantly to the photodissociation of  $\text{HNO}_4$ . Based on these experimental results, the strength of the HOO-NO<sub>2</sub> bond is constrained and compared to literature values. The atmospheric significance of the NIR photodissociation of  $\text{HNO}_4$  is then discussed.

# Contents

<b>Acknowledgements</b>	<b>iv</b>
<b>Abstract</b>	<b>vi</b>
<b>1 Optical Parametric Oscillators (OPOs) as Novel Tunable Light Sources for Atmospheric Photochemistry Studies</b>	<b>1</b>
1.1 Introduction . . . . .	2
1.2 A Type II $\beta$ -BaB <sub>2</sub> O <sub>4</sub> (BBO)-Based OPO Laser System . . . . .	3
<b>2 Photolytic Fractionation of N<sub>2</sub>O</b>	<b>10</b>
2.1 Introduction . . . . .	11
2.2 Fractionation of <sup>15</sup> N/ <sup>14</sup> N and <sup>18</sup> O/ <sup>16</sup> O During Photolysis at 193 nm and 207-215 nm . . . . .	19
2.2.1 Experimental Setup and Procedures . . . . .	19
2.2.2 Results and Discussion . . . . .	22
2.2.3 Atmospheric Implications . . . . .	37
2.3 Fractionation of <sup>14</sup> N <sup>15</sup> N <sup>16</sup> O and <sup>15</sup> N <sup>14</sup> N <sup>16</sup> O During Photolysis at 213 nm . . . . .	45
2.3.1 Experimental . . . . .	45
2.3.2 Results and Discussion . . . . .	50
2.3.3 Comparison with Recent Results from Other Groups . . . . .	53
<b>3 Photodissociation of HNO<sub>4</sub> in the near IR</b>	<b>63</b>
3.1 Introduction . . . . .	64
3.2 Experiments and Results . . . . .	70
3.2.1 Overview of the Experimental Design . . . . .	70
3.2.2 HNO <sub>4</sub> 3 $\nu_{OH}$ and 4 $\nu_{OH}$ Cross Sections from Absorption Spectroscopy	72
3.2.3 FTIR Spectrum of HNO <sub>4</sub> . . . . .	82
3.2.4 Quantum Yields . . . . .	88
3.3 Discussion and Conclusions . . . . .	116

3.3.1	Bond Energy of HOO-NO <sub>2</sub> . . . . .	116
3.3.2	Atmospheric Significance . . . . .	118

## List of Figures

1.1	Schematic diagram of the type II BBO OPO cavity layout. Pumped at 355 nm, this OPO resonates on the idler wave and is tunable over the 410 to 2500 nm range. . . . .	5
1.2	Output power of the type II BBO OPO when pumped with 135 mJ of 355 nm radiation. The inset shows the photoacoustic spectrum of NO near 226 nm taken with this OPO. . . . .	6
1.3	Photoacoustic spectrum of water near 1.6 $\mu\text{m}$ taken with an etalon-narrowed BBO OPO. . . . .	8
2.1	Schematic diagram of the processes considered of major importance to the atmospheric cycles of nitrogen compounds. After Stedman, D. H., and Shetter, R. E., "The Global Budget of Atmospheric Nitrogen Species" in <i>Trace Atmospheric Constituents</i> , S. E. Schwartz (Ed.), Wiley, New York (1983). .	12
2.2	Mole fractions of N <sub>2</sub> O (in ppb) for the past 250 years inferred from field measurements. After the WMO 1998 Report (44). . . . .	13
2.3	Isotopic composition of stratospheric N <sub>2</sub> O compared to tropospheric N <sub>2</sub> O, soil gases, and oceanic N <sub>2</sub> O. After Kim and Craig 1993 (17). . . . .	15
2.4	Diagram of the photolysis laser and gas extraction apparatus used in the N <sub>2</sub> O experiments. Marked with A and B are the two manifolds where vacuum manometry was performed. . . . .	20
2.5	Isotopic signature of $\delta^{15}\text{N}$ in N <sub>2</sub> O remaining after photolysis at 193 nm using Cell 1. (a) Samples are fitted in two separate groups. Filled triangles: all samples except the 77% photolysis sample; open triangle: the sample with 77% photolysis extent. The filled triangle samples are fitted with a Rayleigh model (solid line). The open triangle sample is connected with origin (dashed line). (b) All the samples are fitted with a single Rayleigh model (solid line). The derived enrichment factors, in per mil, are shown on the plot. . . . .	25

- 2.6 Isotopic signature of  $\delta^{18}\text{O}$  in  $\text{N}_2\text{O}$  remaining after photolysis at 193 nm using Cell 1. (a) Samples are fitted in two separate groups. Filled triangles: all samples except 77% photolysis sample; open triangle: the sample with the 77% photolysis extent. The filled triangle samples are fitted with a Rayleigh model (solid line). The open triangle sample is connected with origin (dashed line). (b) All the samples are fitted together with a Rayleigh model (solid line). The derived enrichment factors, in per mil, are shown on the plot. . . . . 26
- 2.7 Isotopic signatures in the remaining  $\text{N}_2\text{O}$  following photolysis at 193 nm using Cell 2. Data obtained with Cell 1 are plotted for comparison. (a)  $^{15}\text{N}$  compared to  $^{14}\text{N}$ ; (b)  $^{18}\text{O}$  compared to  $^{16}\text{O}$ . The same denotations are used in both (a) and (b). Open triangles: Cell 2 data; open circles: Cell 1 data. The solid lines are Rayleigh model fit through Cell 2 samples only. The derived enrichment factors, in per mil, are marked on the plots. . . . . 29
- 2.8 Isotopic signatures in the remaining  $\text{N}_2\text{O}$  following photolysis at 207.5 nm. (a)  $^{15}\text{N}$  compared to  $^{14}\text{N}$ ; (b)  $^{18}\text{O}$  compared to  $^{16}\text{O}$ . The same denotations are used in both (a) and (b). Filled triangles: non-photolyzed samples and those with various photolysis extents from 12% to 28%; open triangle: a single sample with 70% photolysis extent; open circles: pure  $\text{N}_2\text{O}$  samples without  $\text{N}_2$  present as a quenching agent; cross: the sample obtained at 268 K; plus: the sample obtained at 343 K. The solid straight line is a Rayleigh model fit of the filled triangle samples. The open circle samples are fitted with a Rayleigh model through origin as represented by the dash line. The derived enrichment factors, in per mil, are marked on the plots. . . . . 31
- 2.9 Isotopic signatures in the remaining  $\text{N}_2\text{O}$  following photolysis at 211.5 nm. (a)  $^{15}\text{N}$  compared to  $^{14}\text{N}$ ; (b)  $^{18}\text{O}$  compared to  $^{16}\text{O}$ . All the samples are fitted with a Rayleigh model as shown by the solid line. The derived enrichment factors, in per mil, are marked on the plots. . . . . 34
- 2.10 Isotopic signatures in the remaining  $\text{N}_2\text{O}$  following photolysis at 215.25 nm. (a)  $^{15}\text{N}$  compared to  $^{14}\text{N}$ ; (b)  $^{18}\text{O}$  compared to  $^{16}\text{O}$ . All samples are fitted with a Rayleigh model. The derived enrichment factors, in per mil, are marked on the plots. . . . . 36

2.11	Calculated cross sections at 298 and 220 K for N <sub>2</sub> O using the temperature-dependent formula from Selwyn <i>et al.</i> (37). The inset plot is the high-resolution experimental N <sub>2</sub> O absorption cross section data obtained by Yoshino <i>et al.</i> (50), showing vibrational structure at wavelengths shorter than 185 nm.	38
2.12	Comparison of the calculated and measured enrichment factors. (a) $\epsilon^{18}\text{O}$ ; (b) $\epsilon^{15}\text{N}$ .	39
2.13	Comparison of the measured enrichment factors for <sup>15</sup> N (shown in open circles with a dot at the center) with those derived from experimental N <sub>2</sub> O isotopic cross section data taken from Selwyn <i>et al.</i> (38) (the curve). Also plotted is the calculation from Figure 2.12 (the line across the plot).	40
2.14	Calculated $\epsilon^{15}\text{N}$ using the cross sections in Figure 2.11 at 298 and 220 K. “456” stands for <sup>14</sup> N <sup>15</sup> N <sup>16</sup> O while “546” for <sup>15</sup> N <sup>14</sup> N <sup>16</sup> O. “avg” is the arithmetic average of “456” and “546”.	41
2.15	Light from a Nd:YAG laser is directed into the sample compartment of an FTIR spectrometer via a side port. Gas samples are located inside the cell.	46
2.16	FTIR spectra of the three N <sub>2</sub> O isotopomers, taken between 2650 cm <sup>-1</sup> and 2900 cm <sup>-1</sup> , at 0.5 cm <sup>-1</sup> resolution.	49
2.17	The fractionation data from 213 nm photolysis, fitted to a Rayleigh fractionation model. $\delta = (R_i / R_{\text{std}} - 1) \times 1000$ , where the R’s are the slow-to-fast photolysis isotopic ratios. R <sub>std</sub> is for the pre-photolysis samples and R <sub>i</sub> is for the photolyzed samples. f is the fraction of N <sub>2</sub> O remaining. $\epsilon(^{15}\text{N}^{14}\text{N}^{16}\text{O}) = \epsilon(^{15}\text{N}^{14}\text{N}^{16}\text{O} / ^{14}\text{N}^{14}\text{N}^{16}\text{O})$ and $\epsilon(^{14}\text{N}^{15}\text{N}^{16}\text{O}) = \epsilon(^{14}\text{N}^{15}\text{N}^{16}\text{O} / ^{14}\text{N}^{14}\text{N}^{16}\text{O})$ . (a) In Experiment I, three N <sub>2</sub> O isotopomers are photolyzed; (b) In Experiment II, a mixture of <sup>14</sup> N <sup>15</sup> N <sup>16</sup> O and <sup>14</sup> N <sup>14</sup> N <sup>16</sup> O is photolyzed; while in Experiment III, a mixture of <sup>15</sup> N <sup>14</sup> N <sup>16</sup> O and <sup>14</sup> N <sup>14</sup> N <sup>16</sup> O is photolyzed.	51
2.18	The observed fractionation data at different wavelengths. Filled symbols are for $\epsilon(^{14}\text{N}^{15}\text{N}^{16}\text{O} / ^{14}\text{N}^{14}\text{N}^{16}\text{O})$ , and the corresponding open symbols are for $\epsilon(^{15}\text{N}^{14}\text{N}^{16}\text{O} / ^{14}\text{N}^{14}\text{N}^{16}\text{O})$ .	55
2.19	The observed and calculated $\epsilon(^{15}\text{N}^{14}\text{N}^{16}\text{O} / ^{14}\text{N}^{15}\text{N}^{16}\text{O})$ at different wavelengths.	56

3.1	Photochemical loss rates of ozone for the major chemical cycles in the lower stratosphere from ER-2 measurements in May 1993. Adapted from (48). . .	65
3.2	A depiction of the optimized HNO <sub>4</sub> structure. The heavy atom frame is nearly planar, with the H atom oriented perpendicular to the plane. From (25). . . . .	66
3.3	Schematic diagram of the two-color absorption experiment setup. D2, deuterium lamp; DA, diode array detector; DC1, DC2, dichroic mirrors; FT, long-pass filter; L1, L2, focusing lenses; L3, L4, collimating lenses; M1, M2, M3, White Cell mirrors; NIR MC, near-IR monochromator; OC, optical chopper; OMA, optical multichannel analyzer; PMT, photon multiplier tube; QTH, quartz tungsten halogen lamp; RF1, RF2, RF3, RF4, reflectors; UV MC, UV monochromator. . . . .	73
3.4	Raw spectra of HNO <sub>4</sub> . (curve a) Initial spectrum; (curve b) after about 5 min of flow, when the HNO <sub>3</sub> impurity has been significantly reduced. The negative-going spikes may be due to the nonlinearity of the detector. . . .	77
3.5	Plot of the band strength for 3ν <sub>OH</sub> as a function of column density derived from the absorbance measurements at 250 nm and/or 260 nm. (a) H <sub>2</sub> O <sub>2</sub> , including samples taken at both room temperature and ~273 K; (b) HNO <sub>3</sub> ; and (c) HNO <sub>4</sub> , after accounting for H <sub>2</sub> O <sub>2</sub> . . . . .	78
3.6	Spectrum of 3ν <sub>OH</sub> for H <sub>2</sub> O <sub>2</sub> , HNO <sub>3</sub> , and HNO <sub>4</sub> at a resolution of ~1 nm, taken at room temperature for H <sub>2</sub> O <sub>2</sub> and HNO <sub>3</sub> and at ~273 K for HNO <sub>4</sub> .	79
3.7	FTIR spectrum of HNO <sub>4</sub> from 1200 - 1900 cm <sup>-1</sup> . . . . .	84
3.8	FTIR spectrum of HNO <sub>4</sub> from 2850 - 3850 cm <sup>-1</sup> . . . . .	85
3.9	FTIR spectrum of HNO <sub>4</sub> from 4550 - 7540 cm <sup>-1</sup> . . . . .	86
3.10	FTIR spectrum of HNO <sub>4</sub> from 7900 - 8600 cm <sup>-1</sup> . . . . .	87
3.11	Schematic diagram of the action spectrum experimental apparatus. F: long-pass filter; L1, L2, L3, L4: lenses; M1, M2, M3, M4: vis/NIR reflectors; M5, M6: 532 nm reflectors; M7, M8, M9: 266 nm reflectors; P: pressure transducer; S: shutter; T: thermister; and W: waveplate. . . . .	91
3.12	Sensitivity test for NIR/UV beam overlap with the Pellin Broca prism. . .	94
3.13	Spectroscopy and energy transfer in the LIF detection scheme used for OH. From (49). . . . .	95

3.14	OH transitions observed with the LIF apparatus. The $Q_1(2)/Q_{21}(2)$ doublet is used for OH detection in this study. . . . .	98
3.15	Cross sectional diagram of the LIF detection axis used in this study. In this view, the gas flow is pointing out of the paper. RR: retro-reflector; W: quartz window; L1 and L2: lenses; F: interference filter; R: UV reflector. The signal from PMT is registered with a SRS photon counter and the data are stored in a PC. . . . .	99
3.16	Temporal profile of the OH LIF signal from NIR photolysis obtained at 3.5 torr. The decay time constant is found to be $\sim 1.6$ msec. . . . .	102
3.17	Tests of the linearity of the counting system with a continuous OH source. .	104
3.18	Non-linearity in the $2\nu_1$ photolysis with increased NIR power. Marked are the laser powers at the center wavelength of the $2\nu_1$ band. Power variation is within 15% of these values across the entire band. . . . .	106
3.19	LIF signal in Figure 3.18 normalized with NIR laser power. . . . .	107
3.20	LIF signal at the $2\nu_1$ peak as a function of the NIR and UV laser power. . .	108
3.21	An action spectrum of $3\nu_1$ overlaid on an absorption spectrum. . . . .	110
3.22	An action spectrum of $2\nu_1 + \nu_3$ overlaid on an absorption spectrum. . . . .	111
3.23	An action spectrum of $2\nu_1$ overlaid on an absorption spectrum. . . . .	112
3.24	Comparison of product of the quantum yield, $\Phi$ , and the absorption cross section, $\sigma$ , for three $\text{HNO}_4$ bands at 278 K. The intensity of the $2\nu_1$ band is scaled down by a factor of 5. The band shape for $2\nu_1$ is from an FTIR spectrum, that for $2\nu_1 + \nu_3$ is from an action spectrum, and that for $3\nu_1$ is also from an action spectrum. . . . .	114
3.25	Peak-to-peak quantum yield for $2\nu_1$ relative to $3\nu_1$ , determined as a function of pressure. . . . .	115
3.26	Atmospheric transmission spectrum at the top of Mauna Kea, Hawaii. The location of the $\text{HNO}_4$ $2\nu_1$ band is marked. . . . .	121
3.27	The 24-hour averaged loss rates for $\text{HNO}_4$ . The calculation is conducted at equinox for a latitude of $60^\circ$ N. . . . .	123
3.28	Comparison of the relative importance of the NIR photolysis of $\text{HNO}_4$ at two different latitudes. . . . .	124

## List of Tables

2.1	Photolysis experiments at 193 nm using Cell 1. . . . .	23
2.2	Photolysis experiments at 193 nm using Cell 2. . . . .	28
2.3	Photolysis experiments at 207.5 nm. . . . .	30
2.4	Photolysis experiments at 211.5 nm. . . . .	33
2.5	Photolysis experiments at 215.25 nm. . . . .	35
2.6	Partial pressures of different gases in the sample mixtures used in the 213 nm photolysis experiments. . . . .	47
3.1	OH Overtones in H <sub>2</sub> O <sub>2</sub> , HNO <sub>3</sub> , and HNO <sub>4</sub> . . . . .	80
3.2	Vibrational frequencies of HNO <sub>4</sub> . . . . .	83
3.3	Relative strength of the $\nu_1$ , $\nu_2$ , $\nu_3$ and $\nu_4$ modes of HNO <sub>4</sub> . . . . .	89
3.4	Integrated strength of NIR HNO <sub>4</sub> bands from the FTIR spectrum. . . . .	90
3.5	Quantum yields for HNO <sub>4</sub> bands observed in action spectrum experiment. . . . .	113
3.6	Temperature-dependent quantum yields predicted for $2\nu_1$ and 1599 nm. . . . .	119
3.7	NIR Photolysis Rate of HNO <sub>4</sub> at 230 K. . . . .	120

**Chapter 1 Optical Parametric Oscillators (OPOs)  
as Novel Tunable Light Sources for Atmospheric  
Photochemistry Studies**

## 1.1 Introduction

It has been realized for three decades that all solid-state, widely tunable radiation sources can be constructed using the principles of Optical Parametric Oscillator (OPO) technology. In OPOs, nonlinear optical crystals are used to “split” a single shorter wavelength photon into two longer wavelength photons, called the signal (shorter wavelength) and idler (longer wavelength) waves. The tuning range is limited in principle only by the phase matching and transparency of the OPO medium. It is, however, only recently that difficulties associated with crystal growth and high damage threshold optics have been overcome (3). Advances in the fabrication of nonlinear optical materials have led to the discovery of several promising crystal candidates for high power applications. These advances, coupled with the rapid progress in high power pulsed pump laser technology, have made practically possible widely tunable laser sources based on nonlinear optical conversion.

The OPO constructed and used for atmospheric photochemistry studies carried out in this thesis is based on  $\beta$ -BaB<sub>2</sub>O<sub>4</sub> (BBO) crystals. Historically, much of the crystal growth research related to nonlinear optics has been focused on the phosphate crystals (KDP, ADP and KTP). BBO as a nonlinear optical crystal material was established only in the mid-1980’s (1; 2). BBO has a relatively large birefringence and a wide transmission range from 190 nm to 3500 nm. It is phase-matchable from 409.6 nm to 3500 nm for Second Harmonic Generation (SHG), and from 189 nm to 3500 nm for Sum Frequency Generation (SFG). It also has a higher damage threshold than do KTP and LiNbO<sub>3</sub> when pumped in the visible and near-ultraviolet (UV). The nonlinear optical coefficient of BBO is several times larger than that of KDP for harmonic generation at UV wavelengths. Since its discovery, BBO (and the related material lithium triborate or LBO) has received great attention and has become the first commercially available crystal that can be used in UV-pumped OPO devices to generate tunable laser radiation from the UV to the near IR (5).

To achieve high nonlinear conversion efficiencies, there are certain requirements both in terms of power and mode for the pump source. The pulsed Nd:YAG laser chosen as the pump laser in this study is a commercial product from Coherent (Infinity<sup>TM</sup>). Like conventional high-performance YAG lasers, it is based on an oscillator/amplifier configuration. Instead of using continuous wave, or cw, seeders in tandem with a slave Q-switched oscillator to eliminate the mode-beat noise inherent in multimode designs, the Infinity<sup>TM</sup> incorporates a

unique, Q-switched, Diode-Pumped Master Oscillator (DPMO) for single frequency, TEM<sub>00</sub> mode and long-term stability. The 2-rod, double-pass amplifier consists of relay imaging and phase-conjugate optics, and is designed to eliminate birefringence losses and phase-front distortions. Such a system architecture promises delivery of large pulses with good spatial mode qualities over repetition rates that can vary from single shot up to 100 Hz. This combination of capabilities makes the Infinity<sup>TM</sup> an attractive pump laser for OPO-based photochemical studies such as those described in this thesis.

An array of nonlinear schemes can be employed for OPOs. The BBO OPO presented here utilizes a type II configuration, in which the signal beam has a polarization direction perpendicular to that of the idler beam. Details of this type II BBO OPO design have been discussed elsewhere (4). The second section of this chapter therefore provides only a brief description of the cavity structure and the spectroscopic performance demonstrated by this OPO.

## 1.2 A Type II $\beta$ -BaB<sub>2</sub>O<sub>4</sub> (BBO)-Based OPO Laser System

As shown in Figure 1.1, the cavity consists of three mirrors: a plano rear mirror M1, which is a standard near-IR metallic reflector with a Ag protective coating; a plano output coupling mirror M2, which is a standard normal incidence 355 nm high reflector; and a pump input coupler M3, which is a standard 45° high reflector for P-polarized 355 nm light. Two BBO crystals are placed inside the cavity. They counter-rotate to cancel the walk-off losses and provide stable and fine wavelength tunability over 410 - 2500 nm. With respect to the surface of M3, the 355 nm pump beam from the Infinity<sup>TM</sup> is P-polarized. Therefore, with type II phase matching the resulting signal wave is S-polarized and the idler is P-polarized. A long wave pass filter (RG715, Schott Glass) is mounted behind M3 to absorb the signal wave. Since it is at a 45° angle of incidence for the P-polarized wave, i.e., close to Brewster's angle for the idler, the OPO is formed by resonating on the idler wave.

The BBO crystals are cut for type II phase matching at  $\theta = 37^\circ$  and  $\phi = 30^\circ$  with a dimension of 6 (height) x 12 (width) x 12 (length) mm. They are coated with high damage threshold ( $>500$  MW/cm<sup>2</sup> at 355 nm for nanosecond pulses) protective coating, which also serves as a broadband AR coating. The motion of the crystals are controlled by a pair of digital DC servo actuators (850F, Newport), which receive commands from

an in-house developed Labview (National Instruments) program through an OEM motion control PC plug-in card (DCX-PC100, Precision Motion Control). The motors have high translational resolution ( $0.5 \mu\text{m}$ ) and repeatability ( $\pm 2 \mu\text{m}$ ). Each motion card can control up to 8 motors. The two crystals are controlled independently and the angles of incidence for each crystal must be synchronized for stable lasing. This is achieved through calibrating the crystal positions and the corresponding wavelengths using a wavemeter (WA4500, Burleigh).

Operated at 100 Hz, this system can generate up to 600 mWatt of  $1 \mu\text{m}$  radiation, limited by the pump power damage threshold of the BBO crystals. The resulting pulse has a duration of  $\sim 2$  ns and a linewidth of  $\sim 1.5\text{-}2.5 \text{ cm}^{-1}$  that, unlike type I phase matched BBO OPOs, is largely independent of wavelength. The tunability of this OPO can be extended to as short as 205 nm with SHG. Since the OPO output has narrow linewidth and divergence compared to the spectral and angular acceptance requirements of the doubling crystal, high doubling efficiency has been achieved. Figure 1.2 depicts the power output from this OPO along with a 226 nm photoacoustic spectrum of NO obtained with a 7 mm long AR-coated BBO doubling crystal.

Much effort has been made to further reduce the linewidth of the type II BBO OPO. One attempt is to insert an etalon inbetween the filter and the rear mirror M1 (see Figure 1.1). By varying the finesse, any linewidth down to the transform limit can be achieved. To ensure the etalon-inserted cavity runs only on a single resonant frequency of the etalon, the relationship between etalon thickness,  $d$  (in cm), and the bandwidth of the etalon-free OPO,  $\nu$  (in  $\text{cm}^{-1}$ ), must satisfy the following

$$\nu < 1/(2nd)$$

where  $n$  is the index of refraction of the etalon substrate. With the etalon in place, the OPO linewidth should be narrowed to

$$\nu' = \alpha/(2ndF)$$

where  $F$  is the finesse of the etalon, or  $1/\sqrt{(1-R)}$ , with  $R$  being the reflectivity.  $\alpha$  is a factor ( $< 1$ ) that accounts for the further reduction of bandwidth due to multipassing inside

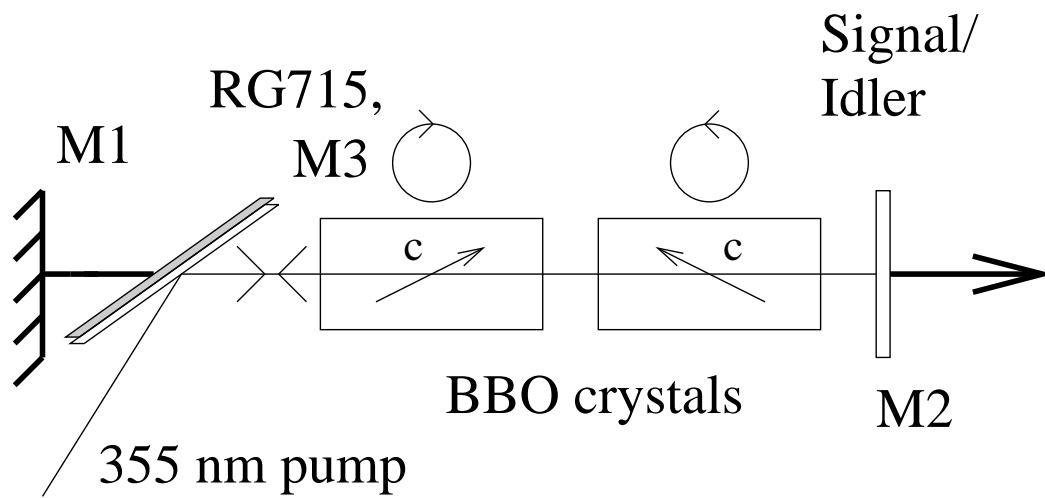


Figure 1.1: Schematic diagram of the type II BBO OPO cavity layout. Pumped at 355 nm, this OPO resonates on the idler wave and is tunable over the 410 to 2500 nm range.

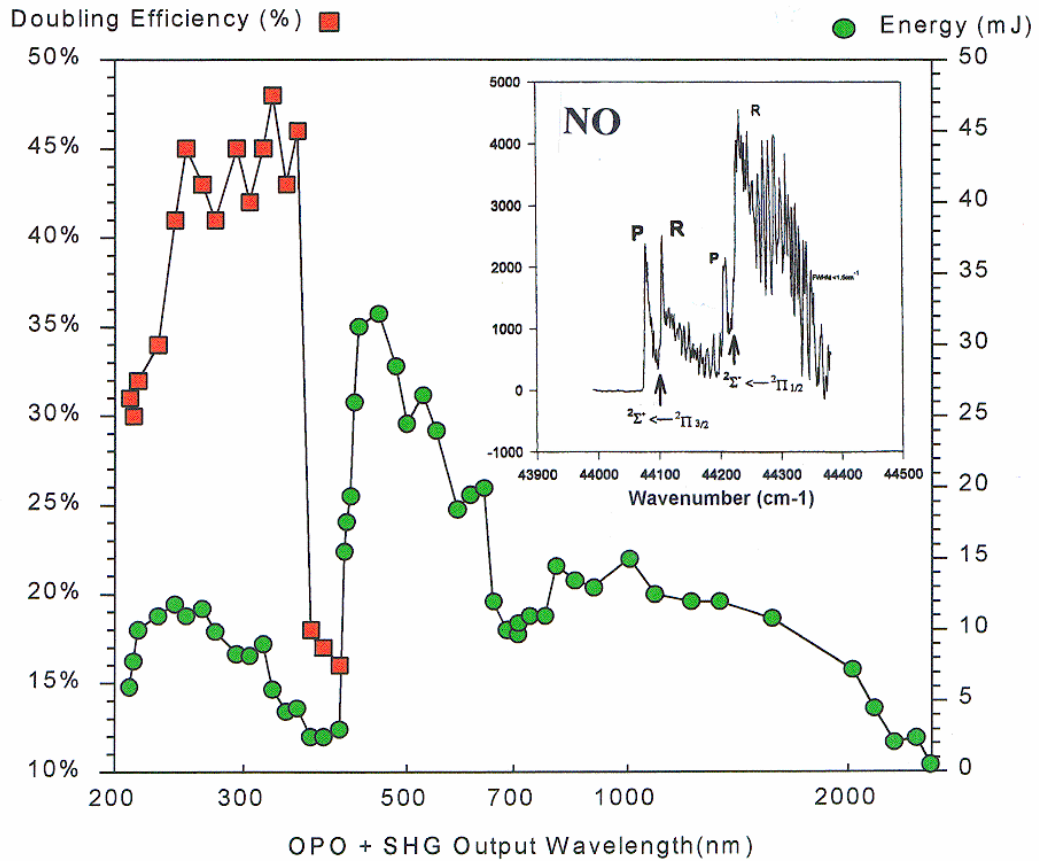


Figure 1.2: Output power of the type II BBO OPO when pumped with 135 mJ of 355 nm radiation. The inset shows the photoacoustic spectrum of NO near 226 nm taken with this OPO.

the cavity. When the cavity's free spectral range (FSR)

$$FSR = 1/(2l) \quad ,$$

where  $l$  = optical pathlength of the OPO cavity, is larger than  $(2ndF)^{-1}$ , and the center frequency of the etalon is matched to that of the OPO cavity, single longitudinal mode (SLM) operation can be established. The center frequency tuning of the etalon is synchronized with the crystal angle tuning. At the same time, a piezo attached to the rear mirror M1 is used to servo control the cavity length. Despite the complexity of the control mechanism, narrowband performance of such an OPO cavity has been demonstrated. For nearly fixed wavelength operation, the efficiency loss is only 15-20% when the etalon position is highly optimized. For a 3 dB scan ranges of 10-20  $\text{cm}^{-1}$ , linewidths between 0.1 and 0.005  $\text{cm}^{-1}$  have been achieved. Scans of longer length can be "stitched" together by slightly overlapping successive etalon scans. Figure 1.3 shows a photoacoustic spectrum of water near 1.6  $\mu\text{m}$ . It is obtained with an etalon of 1.5 mm thickness and a finesse of 20 at 1.6  $\mu\text{m}$ . The spectrum shows that the second OH overtone vibration of water is easily resolved with this etalon-narrowed OPO.

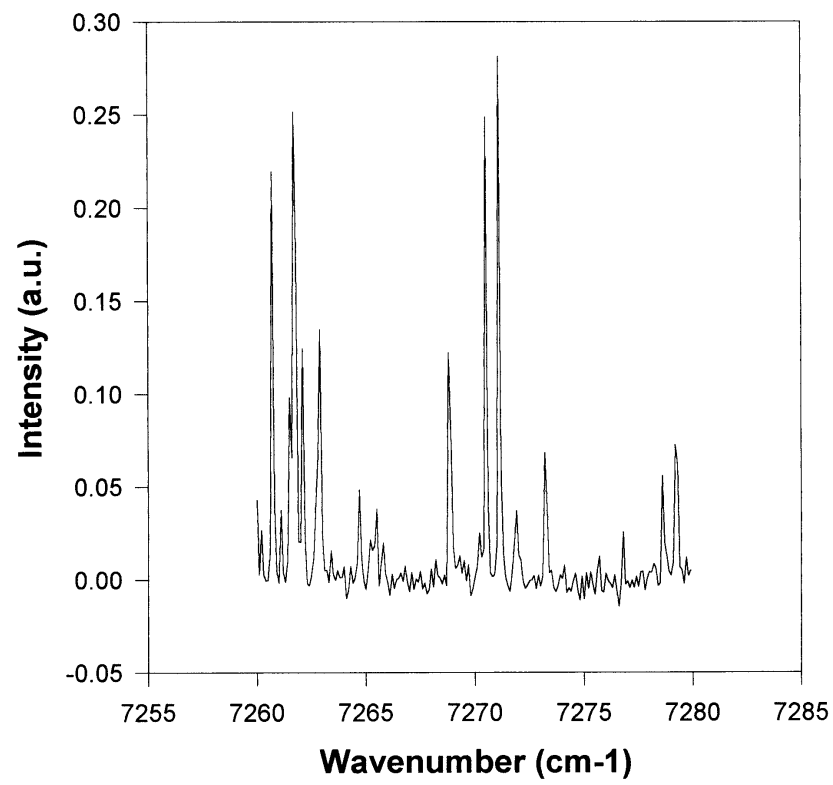


Figure 1.3: Photoacoustic spectrum of water near  $1.6 \mu\text{m}$  taken with an etalon-narrowed BBO OPO.

## Bibliography

- [1] Chen, C., B. Wu, A. Jiang, and G. You, “A new type of ultraviolet SHG crystal -  $\beta$ -BaB<sub>2</sub>O<sub>4</sub>”, *Sientia Sinica, Ser. B*, 28 (1983) 235-243.
- [2] Liang, J. K., Y. L. Zhang, and Q. Z. Huang, “A kinetic study of the BaB<sub>2</sub>O<sub>4</sub> Phase-transition”, *Acta Chimica Sinica*, 40 (1982) 994-1000.
- [3] Tang, C. L., W. Bosenberg, T. Ukachi, R. Lane, and L. K. Cheng, “Optical Parametric Oscillators”, *Proc. I.E.E.E.*, 80 (1992) 365-373.
- [4] Wu, S., G. A. Blake, Z. Y. Sun, and J. W. Ling, “Simple, high-performance type II beta-BaB<sub>2</sub>O<sub>4</sub> optical parametric oscillator”, *Applied Optics*, 36 (1997) 5898-5901.
- [5] Yariv, A., “Optical Electronics”, 4th ed., Saunders College Publishing, New York, 1991.

## Chapter 2 Photolytic Fractionation of N<sub>2</sub>O

## 2.1 Introduction

Nitrogen-containing compounds are essential to life on the Earth. Figure 2.1 depicts our current understanding of the global nitrogen cycle, which both drives and responds to climate change.

Of the various compounds that make up the nitrogen cycle, nitrous oxide, or  $\text{N}_2\text{O}$ , is one of the most important trace gases in the Earth's atmosphere. It is produced primarily by anaerobic biological processes in soils and the oceans. In the troposphere, it is chemically inert.  $\text{N}_2\text{O}$  is an important greenhouse gas with an infrared radiative forcing of approximately 300 times that of  $\text{CO}_2$  on a per molecule basis in the present atmosphere. In the stratosphere,  $\text{N}_2\text{O}$  is photolyzed by ultraviolet radiation, oxidized by excited atomic oxygen, or returned to the troposphere during stratosphere-troposphere exchange processes (STEs). Reaction of  $\text{N}_2\text{O}$  with  $\text{O}(^1\text{D})$  provides the principal natural source of stratospheric  $\text{NO}_x$  ( $= \text{NO} + \text{NO}_2$ ), which is involved in catalytic ozone destruction. Because of its long lifetime (estimated to be  $118 \pm 25$  years (23)),  $\text{N}_2\text{O}$  has been found to be a useful tracer for transport and aging of air masses in stratospheric ozone studies (13).

Because of its importance to the Earth's radiative budget and ozone chemistry,  $\text{N}_2\text{O}$  has drawn significant research attention. As illustrated in Figure 2.2, the mixing ratio of  $\text{N}_2\text{O}$  has grown steadily in the troposphere from an estimated 275 ppb in preindustrial times to 299 ppb by 1976 and 311-312 ppb by 1996 (44). The current rate of increase is about  $0.6 \text{ ppb yr}^{-1}$  (8). The increase of  $\text{N}_2\text{O}$  is thought to arise primarily from the application of fertilizers to cultivated soils, with animal waste, biomass burning, fuel combustion and industrial processes also contributing. To date, the global budget for  $\text{N}_2\text{O}$  has not been well characterized. In 1994, the Intergovernmental Panel on Climate Change (IPCC) suggested that the strength of identified global sources accounted for approximately two-thirds of the sum of the well-established sinks and the accumulation in the atmosphere (14). Recent upward revisions in the strength of various agricultural sources have brought the global  $\text{N}_2\text{O}$  budget closer to balance, however (1; 25; 27). According to a 1998 World Meteorological Organization (WMO) assessment, the median value of the total sources ( $16 \text{ Tg (N) yr}^{-1}$ ) now matches the estimates of the total atmospheric removal ( $12 \text{ Tg (N) yr}^{-1}$ ) and atmospheric accumulation ( $4 \text{ Tg (N) yr}^{-1}$ ), though large uncertainty in the magnitude of individual sources remains (44).

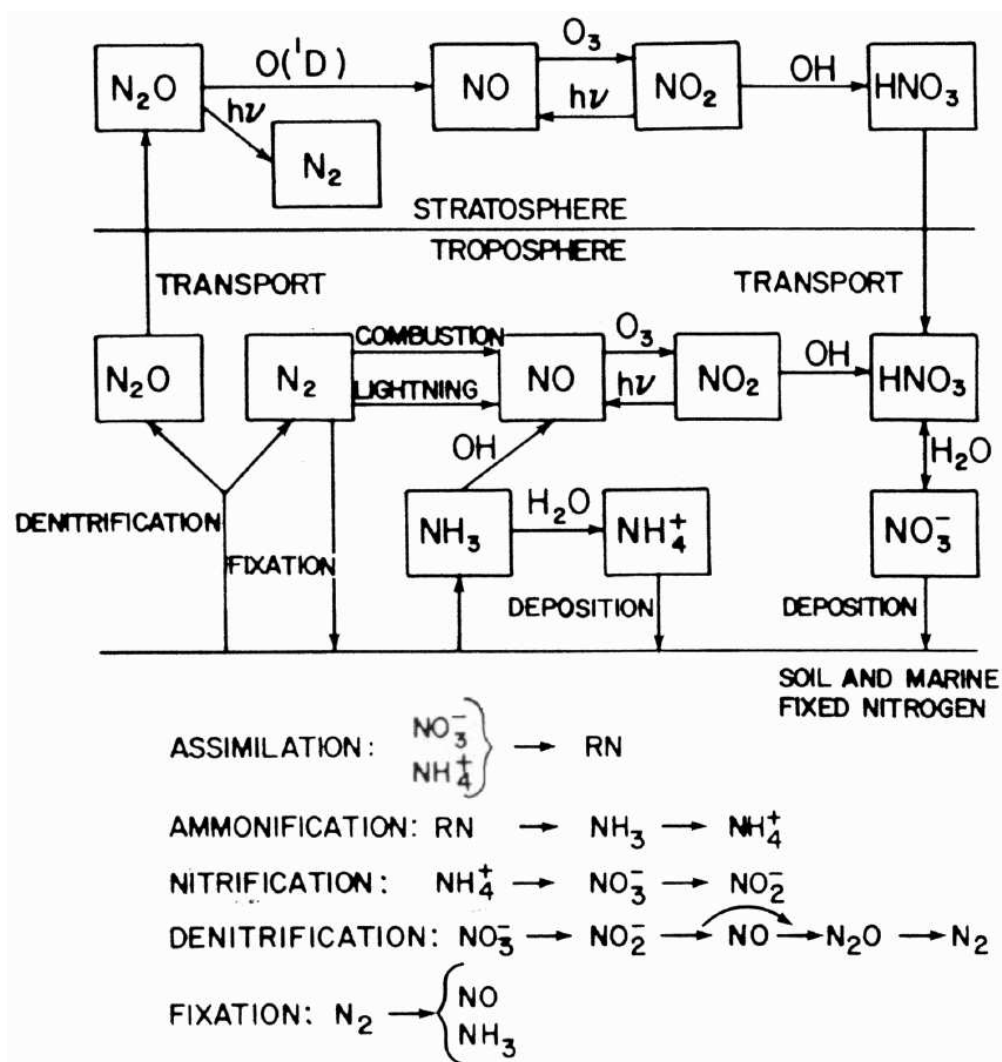


Figure 2.1: Schematic diagram of the processes considered of major importance to the atmospheric cycles of nitrogen compounds. After Stedman, D. H., and Shetter, R. E., "The Global Budget of Atmospheric Nitrogen Species" in *Trace Atmospheric Constituents*, S. E. Schwartz (Ed.), Wiley, New York (1983).

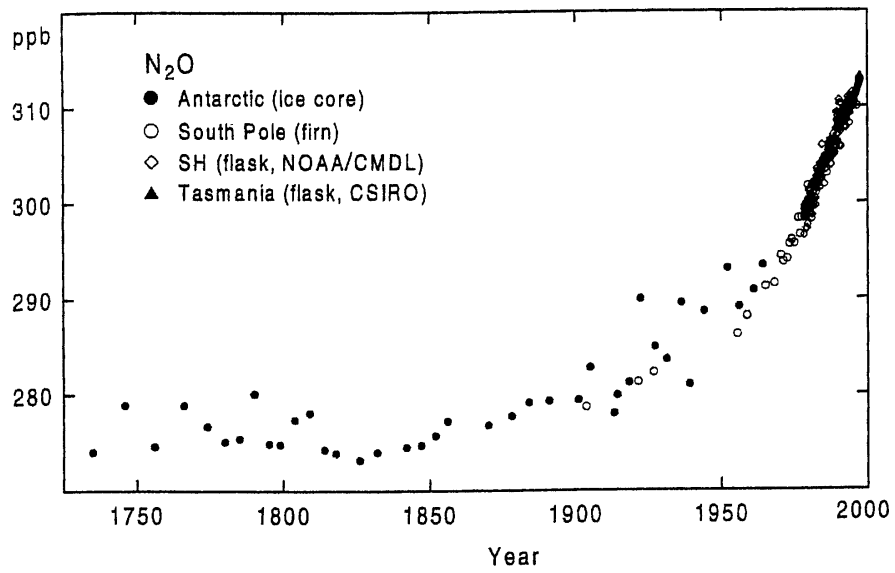


Figure 2.2: Mole fractions of  $N_2O$  (in ppb) for the past 250 years inferred from field measurements. After the WMO 1998 Report (44).

$\text{N}_2\text{O}$  is one of the six gases slated for regulation by the 1997 Kyoto Protocol on Climate Change. This task can not be accomplished until an accurate budget of the individual sources is established. Efforts to determine the global budget of  $\text{N}_2\text{O}$  have included investigations of the stable isotopic signatures of various production and loss processes (3; 12; 16; 17; 24; 26; 33; 42; 45; 46; 47; 48; 49). The goal of these studies was to identify the fractionation patterns for different sources and sinks, and to use such distinctions to constrain the strength of each process. Summarized in Figure 2.3 are atmospheric observations of  $\text{N}_2\text{O}$  from various locations. These measurements show that, relative to tropospheric  $\text{N}_2\text{O}$ , the major biological sources of  $\text{N}_2\text{O}$  are depleted in both  $^{15}\text{N}$  and  $^{18}\text{O}$ , while stratospheric  $\text{N}_2\text{O}$  is found to be substantially enriched. The isotopic analysis approach has not yet been successful in resolving the global budget of  $\text{N}_2\text{O}$ . The extensive sources and long atmospheric lifetime have made it difficult to assemble a comprehensive database. On the other hand, the wide range of observed isotopic values for each of the major natural sources and the incomplete understanding of the isotopic fractionation mechanisms during both biological and photolytical processes also hinder this effort.

The stratospheric data have revealed a coherent trend with concentration that is consistent with a single-stage Rayleigh distillation model (12; 17; 33; 47). Since it is used throughout this chapter to report isotopic fractionation data, a brief description of the model follows.

Rayleigh distillation describes the expected fractionation resulting from an irreversible sink. In this model, isotopic enrichment is related to the remaining fraction of a compound by the expression

$$R = R_0 f^{(\alpha-1)}, \quad (2.1)$$

where  $R$  and  $R_0$  are the residual and initial heavy-to-light isotope ratios,  $f$  is the fraction of the molecule remaining (for example, the stratospheric concentration of  $\text{N}_2\text{O}$  divided by the tropospheric concentration for atmospheric samples, or the post-photolysis concentration divided by the pre-photolysis concentration in the case of a laboratory photolysis experiment), and  $\alpha$  is the ratio of the heavy-to-light reaction or photolysis rates. This relationship can be approximated by  $\delta \cong \delta_0 + \epsilon \times \ln(f)$ , where the slope,  $\epsilon = 1000 (\alpha - 1)$ ,

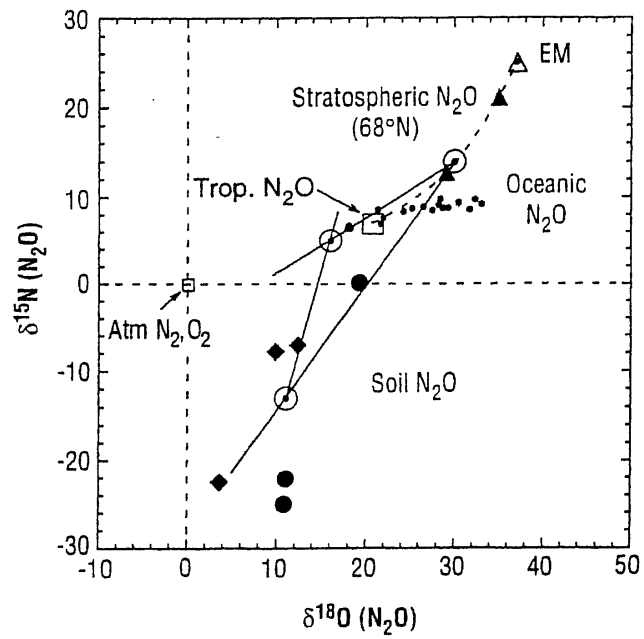
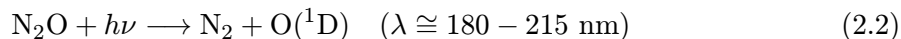


Figure 2.3: Isotopic composition of stratospheric  $N_2O$  compared to tropospheric  $N_2O$ , soil gases, and oceanic  $N_2O$ . After Kim and Craig 1993 (17).

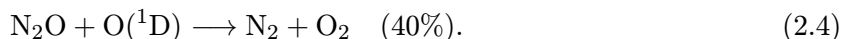
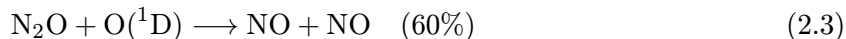
is the enrichment factor expressed in per mil. The  $\delta$  and  $\delta_0$  terms, also expressed in per mil, are the residual and initial delta values, with  $\delta_i$  (for  $\delta$  or  $\delta_0$ ) =  $(R_i / R_{\text{std}} - 1) \times 1000$ , where  $R_i$  and  $R_{\text{std}}$  are the heavy-to-light isotopic ratios in the sample and in the standard.

To my knowledge, there have been five measurements of stratospheric  $\text{N}_2\text{O}$  isotopes. Four of them used laboratory mass spectrometry to analyze air samples retrieved cryogenically from the lower stratosphere (4; 17; 33; 47). Another study performed least squares fitting to  $\text{N}_2\text{O}$  spectra collected by JPL MkIV Fourier Transform Infrared Spectrometer from a balloon platform at 33-40 km altitude in solar occultation mode (12). The enrichment factors determined from these measurements have shown an altitude dependence.  $\epsilon^{15}\text{N}$  of -14.5 per mil and  $\epsilon^{18}\text{O}$  of -12.9 per mil were reported for samples collected between 14.4 and 18.3 km altitude (33), while higher values were obtained in the MkIV measurement by applying weighted least squares regressions over an altitude range of approximately 15 - 30 km (12). The latter yielded enrichment factors, for  $^{15}\text{N}$  and  $^{18}\text{O}$ , of  $\epsilon = -42.3$  and  $-42.6$  per mil, respectively. The difference was explained as a result of the transport and mixing of tropospheric air into the lower stratosphere (12).

The large isotopic enrichments observed in the stratosphere have led to speculation about the validity of the currently accepted stratospheric chemistry of  $\text{N}_2\text{O}$ . The “standard” model assumes that all  $\text{N}_2\text{O}$  sources are biospheric and that there are no significant atmospheric sources of  $\text{N}_2\text{O}$ . It also suggests that 90% of the  $\text{N}_2\text{O}$  loss in the stratosphere occurs via the photolytic reaction



with the remaining 10% lost via the two branches of the reaction with  $\text{O}(^1\text{D})$ :



Experiments by Johnston *et al.* (15) found negligible  $^{18}\text{O}$  fractionation during photolysis reaction (2.2) at 185 nm and an  $\epsilon^{18}\text{O} = -6$  per mil enrichment for the photo-oxidation

reactions (2.3) and (2.4). The lack of large enrichments led a number of researchers to propose the existence of significant unknown stratospheric sources of  $\text{N}_2\text{O}$  (19; 30; 31; 32; 53). They proposed that these hypothetical sources had large enrichment factors as a means of explaining the observed fractionation. Nevertheless, none of these hypotheses have been experimentally demonstrated to be valid. A recently discovered mass-independent fractionation (MIF) of  $^{17}\text{O}$  relative to  $^{18}\text{O}$  indicates some unknown MIF processes for oxygen isotopes in  $\text{N}_2\text{O}$  (3; 4; 39). A coupling to  $\text{O}_3$  chemistry could provide this  $^{17}\text{O}$  MIF in  $\text{N}_2\text{O}$ ; however, such a process will not impact the overall  $\text{N}_2\text{O}$  budget since the  $\Delta^{17}\text{O}$  value is only about 0.5 - 1 per mil ( $\Delta^{17}\text{O} = \delta^{17}\text{O} - 0.515 \delta^{18}\text{O}$ ). On the other hand, the stratospheric data are compatible with a single stage loss process, indicating that the mechanism responsible for the observed enrichment is most likely a sink (4; 12; 33; 47).

Yung and Miller (YM97) (51) have put forward a mechanism for the isotopic fractionation of  $\text{N}_2\text{O}$  during UV photolysis. They propose that the observed stratospheric enrichment in heavy  $\text{N}_2\text{O}$  can be accounted for within the cohesive framework of the standard photochemical model. The theory is based on the subtle differences in the molecular zero point energies (ZPEs) with isotopic substitution. While the cross sections are essentially identical at the absorption peak, a clear separation is manifest on both shoulders with heavy isotopomers shifted to the blue compared to the normal  $\text{N}_2\text{O}$  (i.e.,  $^{14}\text{N}^{14}\text{N}^{16}\text{O}$ ). Analogous to determining the kinetic fractionation for a chemical reaction, the photolysis fractionation factor will be equal to the ratio of the cross sections for different isotopomers. At wavelengths shorter than  $\sim 182$  nm,  $\epsilon$  is initially positive, but passes through zero at the cross section maximum and gets progressively more negative with increasing wavelength.

The YM97 theory also offers an explanation for the apparent incompatibility of the observations and laboratory results. The photolysis experiments of Johnston *et al.* (15) were performed with a Hg arc lamp at 184.9 nm, near the peak of the  $\text{N}_2\text{O}$  absorption continuum, where the influence of the ZPE differences is close to zero. Johnston *et al.* extrapolated their results at 185 nm to other wavelengths by citing the small shifts in the  $\text{N}_2\text{O}$  UV cross sections with isotopic substitution observed by Selwyn and Johnston (38), and concluded that fractionation should be inconsequential when averaged across the continuum. Previous work by Froidevaux and Yung (11) and Minschwaner *et al.* (22) had shown, however, that while the  $\text{N}_2\text{O}$  cross section does indeed peak at  $\sim 182$  nm, the photolysis in the stratosphere occurs principally at longer wavelengths, specifically in the

190-210 nm window. This window is defined by the O<sub>2</sub> Schumann-Runge bands to the blue and O<sub>2</sub> Herzberg continuum plus ozone Hartley and Huggins band absorption to the red. The integration of  $\epsilon$  over this range results in the enrichment of heavy N<sub>2</sub>O isotopomers, as shown in YM97, with values quantitatively comparable to the stratospheric data.

This chapter contains experimental investigations of the photolytic fractionation of N<sub>2</sub>O in an attempt to test the YM97 theory. A series of UV photolysis experiments were conducted at various wavelengths. The isotopic analysis was performed either by Mass Spectrometry (MS) after the photolysis was finished, or by Fourier Transform InfraRed (FTIR) spectroscopy in real-time with the photolysis. Section 2.2 examines the fractionation of <sup>15</sup>N/<sup>14</sup>N and <sup>18</sup>O/<sup>16</sup>O during photolysis at 193 nm and 207-215 nm with MS, while Section 2.3 addresses the fractionation of the structural isotopomers <sup>14</sup>N<sup>15</sup>N<sup>16</sup>O and <sup>15</sup>N<sup>14</sup>N<sup>16</sup>O during photolysis at 213 nm with FTIR.

These measurements have consistently shown large heavy enrichment of the residual N<sub>2</sub>O isotopomers. Qualitatively, the wavelength-dependent fractionation follows the same trend as predicted by YM97, and the observed isotopomer-specific fractionations scale with the ZPE differences noted by YM97. These results support YM97's suggestion that this mechanism is significant and may account for the isotopic fractionation observed in the stratosphere. The magnitude of the observed fractionation, however, is significantly larger than predicted but in accord with the sizable fractionation observed in the stratosphere. In Section 2.3.2, an attempt to reconcile the differences is given which notes the existence of vibrationally "hot" N<sub>2</sub>O molecules at room temperature and the possible involvement of more than two electronic states in the photolysis. A fully quantitative test of YM97 theory will require accurate wavelength and temperature dependent differential cross sections for each of the N<sub>2</sub>O isotopomers that are not yet available.

## 2.2 Fractionation of $^{15}\text{N}/^{14}\text{N}$ and $^{18}\text{O}/^{16}\text{O}$ During Photolysis at 193 nm and 207-215 nm

[Some of the results presented in this section have appeared in “Stable Isotope Fractionation During Ultraviolet Photolysis of  $\text{N}_2\text{O}$ ” by Rahn, T., H. Zhang, M. Wahlen, and G. A. Blake in *Geophys. Res. Lett.*, 25, 4489-4492, 1998. Copyright by the American Geophysical Union. This work is the result of a collaboration with Drs. T. Rahn and M. Wahlen from the Scripps Institution of Oceanography at the University of California at San Diego.]

### 2.2.1 Experimental Setup and Procedures

Figure 2.4 is a schematic of the experimental setup, illustrating the UV light source, the photolysis cell, and the gas preparation and extraction glassware. The photolysis of nitrous oxide was performed at 193 nm and 207-215 nm. A Lambda Physik LPX 120i excimer laser was used to provide the 193 nm photons. Tunable radiation between 207-215 nm was generated by doubling the visible output of a type II BBO OPO described in Chapter 1. The frequency-doubling of the output was accomplished with a type I BBO crystal. After the doubling stage, a Pellin Broca (PB) prism was used to separate the UV beam from the other wavelengths. A ceramic hard aperture was placed to ensure that only UV light entered the photolysis cell. The photolysis wavelength was obtained by directing the visible light leaking through an OPO mirror into a wavemeter (Burleigh, WA4500). The photolysis power was recorded after the beam exited the photolysis cell.

To determine the robustness of the experimental results, the irradiance flux of the photolysis was varied at each wavelength by changing the laser power, repetition rate and duration of photolysis. All OPO experiments were conducted at 100 Hz.

Two pyrex cells were fabricated for use in the photolysis of nitrous oxide. Both cells were equipped with similar ports for sample inlets and vacuum lines and UV fused silica windows. Cell 1 had a jacketed outer layer to allow temperature control while Cell 2 could be used only at room temperature. In addition, the two cells were of different geometry. Cell 1 had a volume of  $\sim 310\text{ cm}^3$  with a 4 cm I.D. and a length of 25 cm. The clear aperture of its window was about 1 cm in diameter. This cell was used for photolysis experiments at all wavelengths. Because of its dimensions, the gas in the cell could not be uniformly illuminated. This caused concern that diffusion-driven isotopic fractionation could cause

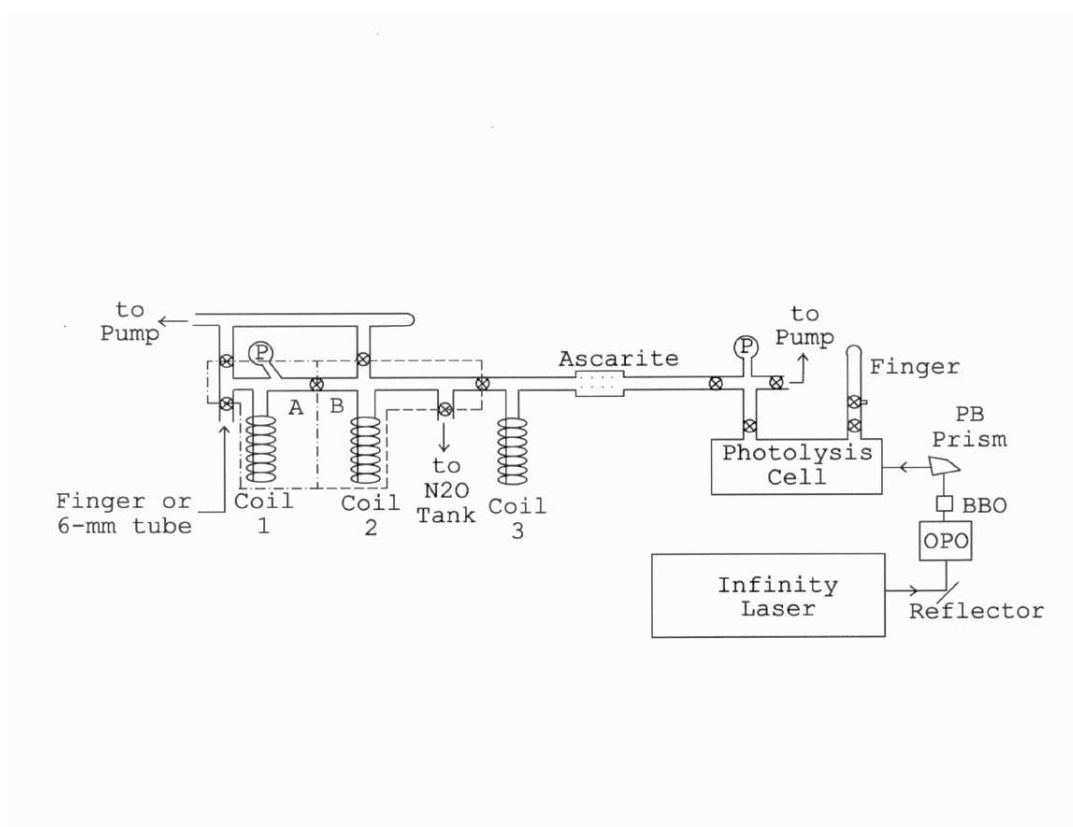


Figure 2.4: Diagram of the photolysis laser and gas extraction apparatus used in the  $\text{N}_2\text{O}$  experiments. Marked with A and B are the two manifolds where vacuum manometry was performed.

an artifact in the experiment. For example, the OPO output beam was about 0.5 cm in diameter and when directly sent into Cell 1, it only illuminated  $\sim 2\%$  of the cross sectional area of the cell. At 193 nm, the UV beam was tailored to a diameter of  $\sim 1$  cm when Cell 1 was used. In even this case, only a small fraction of the cross sectional area was illuminated by the photolysis beam. Cell 2 was designed to address this problem in that it was made of thick-wall pyrex with a 2 cm I.D. and a length of 25 cm. The clear aperture of the windows were thus the same as the cross section of the cell. In some of the photolysis runs at 193 nm, where the excimer output was reshaped to a diameter of 2 cm with a pair of quartz lenses, the entire column of Cell 2 could be illuminated uniformly. Results from these experiments provide a test for a diffusion-driven fractionation artifact. Such tests were not performed for wavelengths 207-215 nm because the low UV power at those wavelengths did not allow efficient beam reshaping.

The photolysis yield was determined from the initial and final amounts of nitrous oxide by vacuum manometry in the A and B manifolds (see Figure 2.4). The volumes of A and B were carefully calibrated against a finger of known volume. The initial sample of  $\text{N}_2\text{O}$  was prepared by cryogenically trapping the gas into a finger and then adding it to the cell. At the end of each photolysis run, the gas mixture was slowly bled into the vacuum line where it was purified. In the first stage, it passed through a column of ascarite to remove  $\text{NO}_x$  and other possible impurities such as  $\text{CO}_2$ . Coil 3, immersed in an acetone/liquid  $\text{N}_2$  slush kept at  $-80^\circ\text{C}$ , then acted as a trap for  $\text{H}_2\text{O}$  and residual  $\text{CO}_2$ . After this stage, the mixture should contain only  $\text{N}_2\text{O}$ ,  $\text{O}_2$  and  $\text{N}_2$ . Finally, Coil 1 and Coil 2 were alternatively used to trap  $\text{N}_2\text{O}$  with liquid  $\text{N}_2$  while  $\text{N}_2$  and  $\text{O}_2$  were pumped off. The amount of  $\text{N}_2\text{O}$  remaining was determined by manometry before the gas was flame-sealed in a 6 mm glass tube. In order to verify the gas handling procedures, several samples were processed without irradiation. It is found that the extraction procedure allows at least a 97% recovery rate. That corresponds to a  $\ln(f)$  precision of  $\pm 3\%$ .

Subsequent isotopic analysis was performed on a VG-Prism II mass spectrometer at the Scripps Institute of Oceanography. The methodology for the direct injection of  $\text{N}_2\text{O}$  into the VG triple collector mass spectrometer has been described elsewhere and includes monitoring of peaks at  $M/z = 12$  and  $22$  for possible  $\text{CO}_2$  contamination (33). The analyses of the  $^{15}\text{N}$  data are complicated by the fact that there are three additional isotopomers to be accounted for (i.e.,  $^{14}\text{N}^{15}\text{N}^{16}\text{O}$ ,  $^{15}\text{N}^{14}\text{N}^{16}\text{O}$  and  $^{14}\text{N}^{14}\text{N}^{17}\text{O}$ ). The first two of these are

not distinguishable with the conventional mass spectrometric method used in this study. It should be pointed out that a molecular and fragment ion analysis technique was later developed by several groups to determine the  $^{15}\text{N}$  position-dependent fractionation (2; 36; 40; 47). The  $^{14}\text{N}^{14}\text{N}^{17}\text{O}$  isotopomer was accounted for by applying a variation of the standard correction which assumes mass dependent enrichment (5). This treatment is considered valid since any mass independent enrichment on the order of that observed by Cliff and Thiemens (3) would result in additional corrections which are smaller than the experimental precision reported here (see, for instance, Rockmann and Brenninkmeijer (35)). For the combined extraction procedure and mass spectrometric analysis, the reported data have a precision of  $\pm 0.2$  and  $\pm 0.4$  for  $\delta^{15}\text{N}$  and  $\delta^{18}\text{O}$ , respectively.

In order to suppress reaction of the  $\text{N}_2\text{O}$  sample with  $\text{O}(^1\text{D})$  formed during photolysis, ultra-high purity  $\text{N}_2$  gas was added as a quenching agent, typically at an  $\text{N}_2:\text{N}_2\text{O}$  ratio of 150:1. The rate constant for the reaction of  $\text{O}(^1\text{D})$  and  $\text{N}_2$  to form  $\text{N}_2\text{O}$  has been shown to be extremely slow due to an electronic curve crossing (6). Production of  $\text{N}_2\text{O}$  via heterogeneous reactions involving  $\text{N}_2$  and atomic oxygen is also expected to be negligible relative to the sample size (15; 18). Varying amounts of  $\text{N}_2$  were added to test whether varying the quenching efficiency influenced the fractionation.

## 2.2.2 Results and Discussion

Since there is no single universally accepted  $\text{N}_2\text{O}$  isotopic standard as of yet, it is worthwhile to first clarify the standard used to report all the results here. All the  $\delta$  values are calculated relative to the starting  $\text{N}_2\text{O}$  sample, which happens to be one of the standards, the Standard Nitrous Oxide Working gas (SNOW), and can be related to another frequently used standard, atmospheric  $\text{N}_2$  and  $\text{O}_2$ . The conversion relationship is that SNOW has  $\delta^{15}\text{N} = 1.31$  per mil and  $\delta^{18}\text{O} = 18.46$  per mil relative to atmospheric  $\text{N}_2$  and  $\text{O}_2$ , respectively.

*193 nm:* Table 2.1 contains the details of various photolysis experiments conducted at 193 nm with the large diameter cell (Cell 1). Listed under pulse energy is the range of the observed power fluctuation during the course of a photolysis run. “np” (for “no photolysis”) in the table denotes samples collected without irradiance. The initial  $\text{N}_2\text{O}$  sample was approximately 400  $\mu\text{l}$  at one atmosphere. The total pressure in the cell was varied from 150 to 250 torr for different  $\text{N}_2:\text{N}_2\text{O}$  mixing ratios. All data were collected at room temperature.

Table 2.1: Photolysis experiments at 193 nm using Cell 1.

Sample #	Rep Rate (Hz)	Pulse Energy (mJ)	Duration (minutes)	N <sub>2</sub> :N <sub>2</sub> O	Residual Fraction	ln(f)	$\delta^{15}\text{N}$ (per mil)	$\delta^{18}\text{O}$ (per mil)
56	np	np	np	200	0.99	-0.01	-0.2	-0.4
55	100	0.5-1.2	12	150	0.63	-0.47	9.9	7.7
62	100	3.5-4.5	1.2	180	0.83	-0.18	3.9	2.8
49	100	1.0-1.2	3	150	0.85	-0.17	3.5	2.7
51	100	3.8-4.0	3	160	0.79	-0.24	5.2	4.0
50	100	1.6-2.0	6	150	0.61	-0.50	10.4	7.9
57	100	4.5-5.2	5	250	0.43	-0.84	15.3	12.0
58	100	4.4-5.0	5	160	0.44	-0.81	15.3	11.9
52	100	4.4-4.6	1.5	160	0.75	-0.29	6.1	4.7
53	100	4.4-4.6	3	150	0.59	-0.53	10.8	8.3
54	100	4.6-4.8	5	200	0.43	-0.83	15.7	12.2
59	10	0.8-1.0	60	220	0.82	-0.20	4.4	3.2
61	10	2.5-3.5	12	155	0.83	-0.19	3.9	2.7
63	1	3.5-4.5	120	160	0.79	-0.24	5.1	3.8
60	1	4.0-6.0	600	160	0.23	-1.46	33.5	26.4

Figures 2.5 and 2.6 present the data from Table 2.1 graphically. Two ways of data fitting were attempted to explore whether sample #60 (the sample with the highest photolysis extent) was a valid sample. In Figure 2.5(a) and Figure 2.6(a), a Rayleigh fit was performed using all the samples except #60. This gave  $\epsilon^{15}\text{N} = -18.4$  per mil and  $\epsilon^{18}\text{O} = -14.6$  per mil at 193 nm, as we previously reported (34). Sample #60 was not included in this fit because of its apparently high enrichment factor (as illustrated by the dashed lines in the figures). There was concern about whether the amount of  $\text{N}_2$  used had provided adequate quenching at 77% photolysis. Without adequate quenching, reaction of  $\text{N}_2\text{O}$  with  $\text{O}(^1\text{D})$  would also contribute to the loss of  $\text{N}_2\text{O}$ ; however, this should have resulted in a smaller enrichment than with a pure photolysis reaction according to Johnston *et al.* (15). Another possibility was that a significant amount of  $\text{NO}_x$  was produced and was not completely removed during the gas extraction (the final sample size was as small as  $\sim 80 \mu\text{l}$  in this case). That could lead to an underestimate of the photolysis extent. All the samples underwent similar cleaning stages at Scripps before being introduced into the mass spectrometer and there were no significant amounts of impurities found, however. On the other hand, a close look at the solid line fit in Figure 2.5 (a) and Figure 2.6 (a) reveals that it is heavily biased toward less steep slope due to a cluster of samples around  $\ln(f) = -0.83$ . If a Rayleigh fit is applied to all the data,  $\epsilon^{15}\text{N} = -21.4$  per mil and  $\epsilon^{18}\text{O} = -17.0$  per mil at 193 nm is obtained. This appears to be a reasonable fit as shown in Figure 2.5 (b) and Figure 2.6 (b). We also note here that the photolysis for sample #60 occurred on a relatively slow timescale (1 Hz laser repetition rate for 10 hours).

Regardless of whether #60 was a valid sample, this set of data have shown enrichment of  $^{15}\text{N}$  and  $^{18}\text{O}$  in the remaining  $\text{N}_2\text{O}$  samples following photolysis at 193 nm. The Rayleigh fit demonstrates that the observed enrichments scale consistently with the flux of the photolysis radiation. The sample with no photolysis falls very close to the origin, showing good gas handling protocols. Mindful of the concerns that the fractionation observed might be diffusion-driven, Cell 2 was used in a series of experiments at 193 nm to test this possibility. Shown in Table 2.2 are the details of these experiments. Samples started with  $100 \mu\text{l}$  at one atmosphere. Since the volume of Cell 2 was four times smaller than Cell 1, the total pressure inside the cell was comparable with that in Cell 1.

Figure 2.7 is a plot of these data. Data obtained with Cell 1 are also plotted for comparison. The solid line fits through all the Cell 2 samples only. It demonstrates the

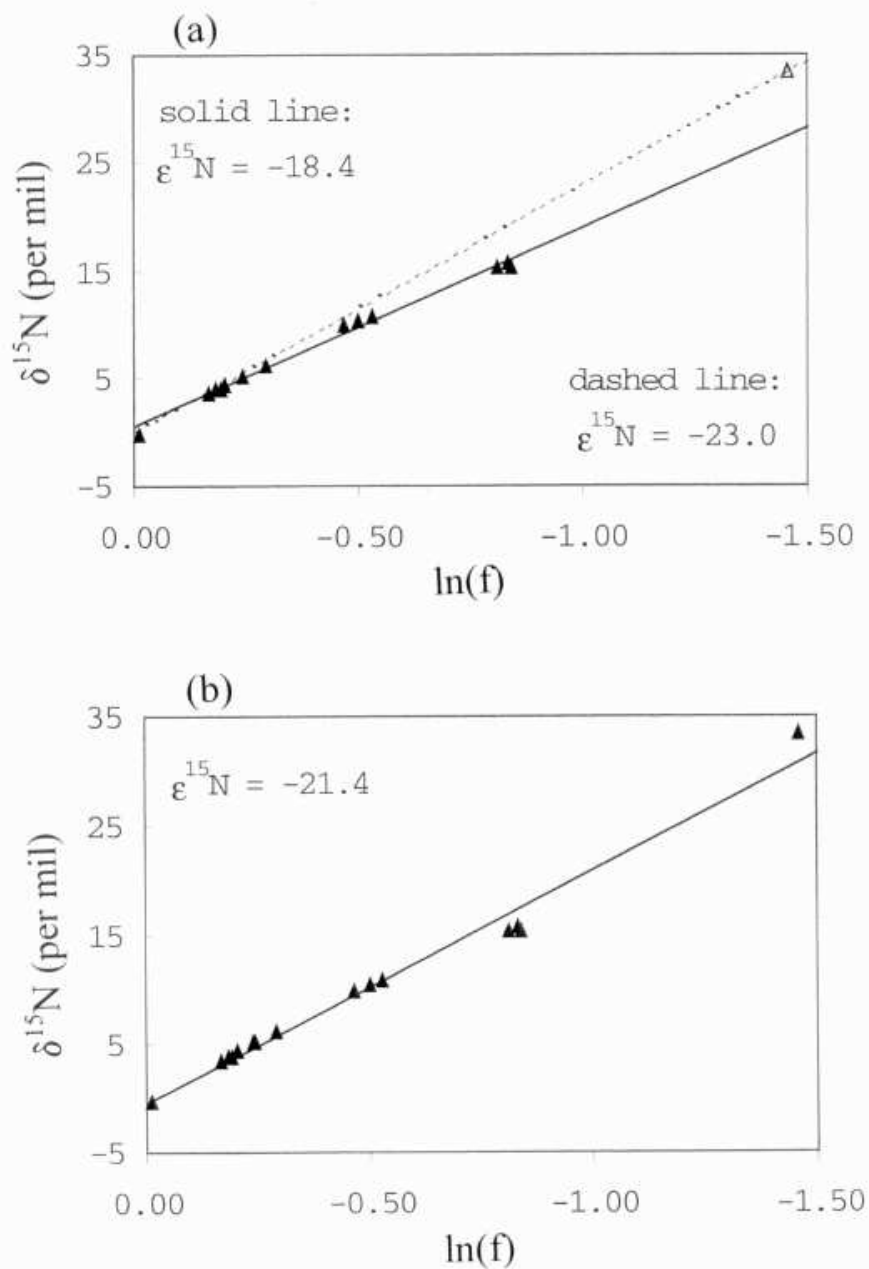


Figure 2.5: Isotopic signature of  $\delta^{15}\text{N}$  in  $\text{N}_2\text{O}$  remaining after photolysis at 193 nm using Cell 1. (a) Samples are fitted in two separate groups. Filled triangles: all samples except the 77% photolysis sample; open triangle: the sample with 77% photolysis extent. The filled triangle samples are fitted with a Rayleigh model (solid line). The open triangle sample is connected with origin (dashed line). (b) All the samples are fitted with a single Rayleigh model (solid line). The derived enrichment factors, in per mil, are shown on the plot.

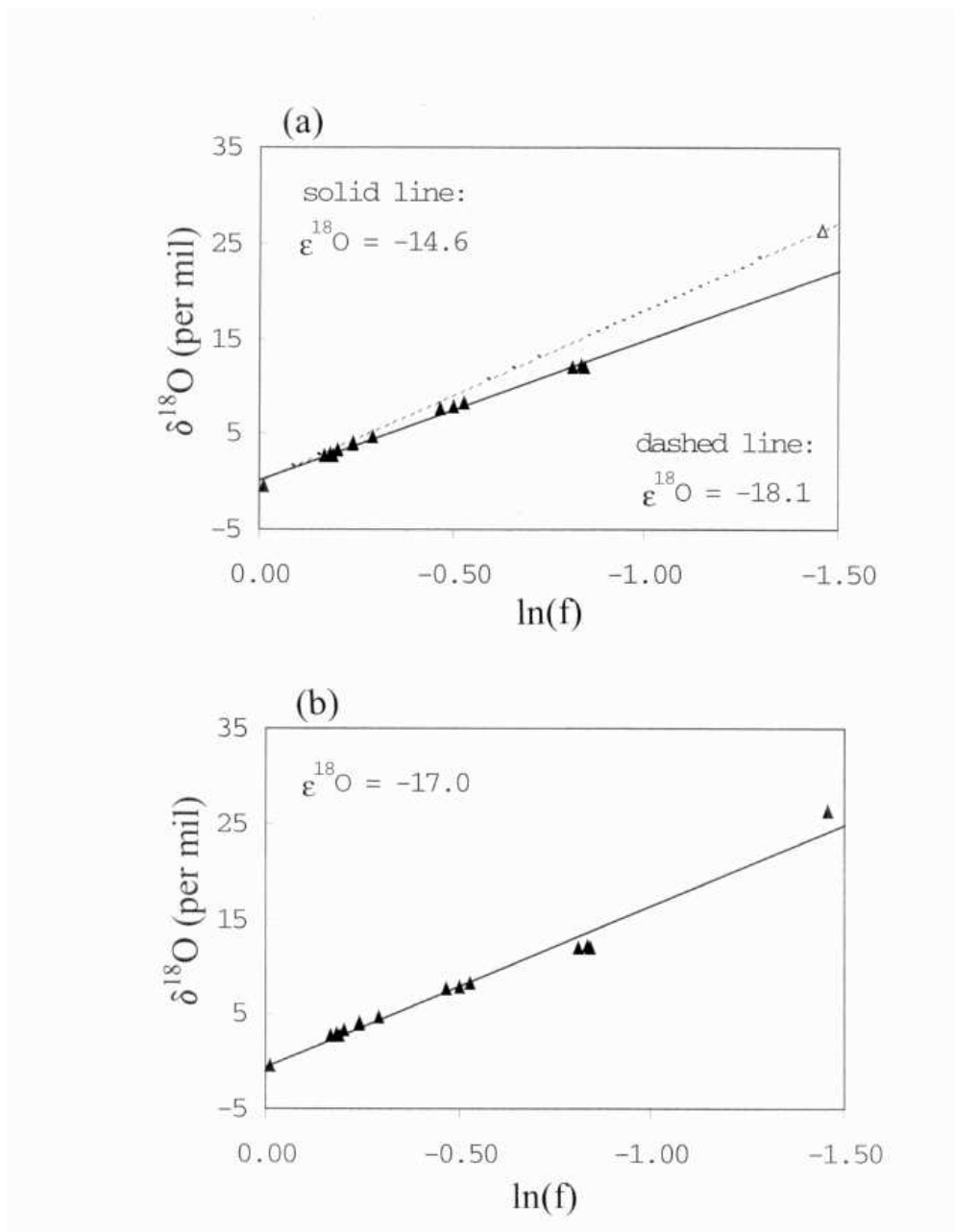


Figure 2.6: Isotopic signature of  $\delta^{18}\text{O}$  in  $\text{N}_2\text{O}$  remaining after photolysis at 193 nm using Cell 1. (a) Samples are fitted in two separate groups. Filled triangles: all samples except 77% photolysis sample; open triangle: the sample with the 77% photolysis extent. The filled triangle samples are fitted with a Rayleigh model (solid line). The open triangle sample is connected with origin (dashed line). (b) All the samples are fitted together with a Rayleigh model (solid line). The derived enrichment factors, in per mil, are shown on the plot.

consistency of Cell 2 data with a Rayleigh fit despite the wide variation of the total photolysis flux. Cell 1 data lie close to Cell 2 data and their fit. The ratio of the derived enrichment factors (i.e.,  $\epsilon^{15}\text{N} = -20.6$  per mil and  $\epsilon^{18}\text{O} = -16.2$  per mil) are in good agreement with data obtained with Cell 1. The similarity implies that the same process is responsible for the fractionation observed in both cells, therefore, the diffusion mechanism is unlikely to introduce a significant source of error. Cell 2 results also imply that including sample #60 is reasonable. Applying the Rayleigh fit to all the data on Figure 2.7 yields  $\epsilon^{15}\text{N} = -20.8$  per mil and  $\epsilon^{18}\text{O} = -16.4$  per mil at 193 nm. These are the enrichment factors we report for 193 nm.

*207.5 nm:* For the remaining OPO experiments, all of the data presented below were obtained with Cell 1. The initial  $\text{N}_2\text{O}$  sample size was always  $\sim 400 \mu\text{l}$  (at one atmosphere). The OPO was run at a constant repetition rate (100 Hz), but the pulse energy and photolysis duration were varied to test for multi-photon effects.

Table 2.3 summarizes the results of the photolysis experiments at 207.5 nm. Unless noted in the table, all samples were photolyzed at room temperature. The enrichment data are plotted in Figure 2.8.

Photolysis at 207.5 nm unambiguously shows that larger enrichments are observed at longer wavelengths. Except for the high photolysis sample (marked with an open triangle), all the samples with  $\text{N}_2$  quenching can be fitted with the Rayleigh model, yielding  $\epsilon^{15}\text{N}$  of -50.1 per mil and  $\epsilon^{18}\text{O}$  of -47.4 per mil. No trend with laser power was observed. For the photolysis yield of these samples, an  $\text{N}_2:\text{N}_2\text{O}$  ratio of 150 seems adequate for efficient quenching. Increasing the quenching ratio to 300 (sample #34) did not change the isotopic signature compared to samples with an  $\text{N}_2:\text{N}_2\text{O}$  ratio of 150. These results rule out any significant production of  $\text{N}_2\text{O}$  by reaction with atomic oxygen, in either third body or heterogeneous reactions, as any production would be expected to depend on both the reactant concentrations and on the reaction rates. Therefore, the observed fractionation is that due to photolysis alone.

Two samples (#35 and #33) were photolyzed with no quenching gas. A straight line fits these two data points through origin, giving  $\epsilon^{15}\text{N}$  of -28.5 per mil and  $\epsilon^{18}\text{O}$  of -29.2 per mil. These values are smaller than from those  $\text{O}(^1\text{D})$ -quenched samples, implying that the oxidation of  $\text{N}_2\text{O}$  by  $\text{O}(^1\text{D})$  involves much smaller enrichment, in agreement with the

Table 2.2: Photolysis experiments at 193 nm using Cell 2.

Sample #	Rep Rate (Hz)	Pulse Energy (mJ)	Duration (minutes)	N <sub>2</sub> :N <sub>2</sub> O	Residual Fraction	ln(f)	δ <sup>15</sup> N (per mil)	δ <sup>18</sup> O (per mil)
64	np	np	np	150	0.97	-0.03	0.3	0.2
71	100	0.65-0.85	1	300	0.80	-0.22	3.0	2.4
68	100	0.65-0.85	2	150	0.69	-0.37	6.8	5.6
65	100	0.55-0.65	20	150	0.17	-1.75	35.5	27.9
67	10	0.55-0.65	10	150	0.89	-0.12	2.1	1.5
72	10	0.60-0.75	10	150	0.87	-0.14	2.9	2.2
73	10	0.30-0.45	20	150	0.85	-0.16	2.8	2.1
66	10	0.55-0.65	20	150	0.78	-0.25	4.0	3.3
70	10	0.60-0.75	20	150	0.79	-0.24	5.4	4.1

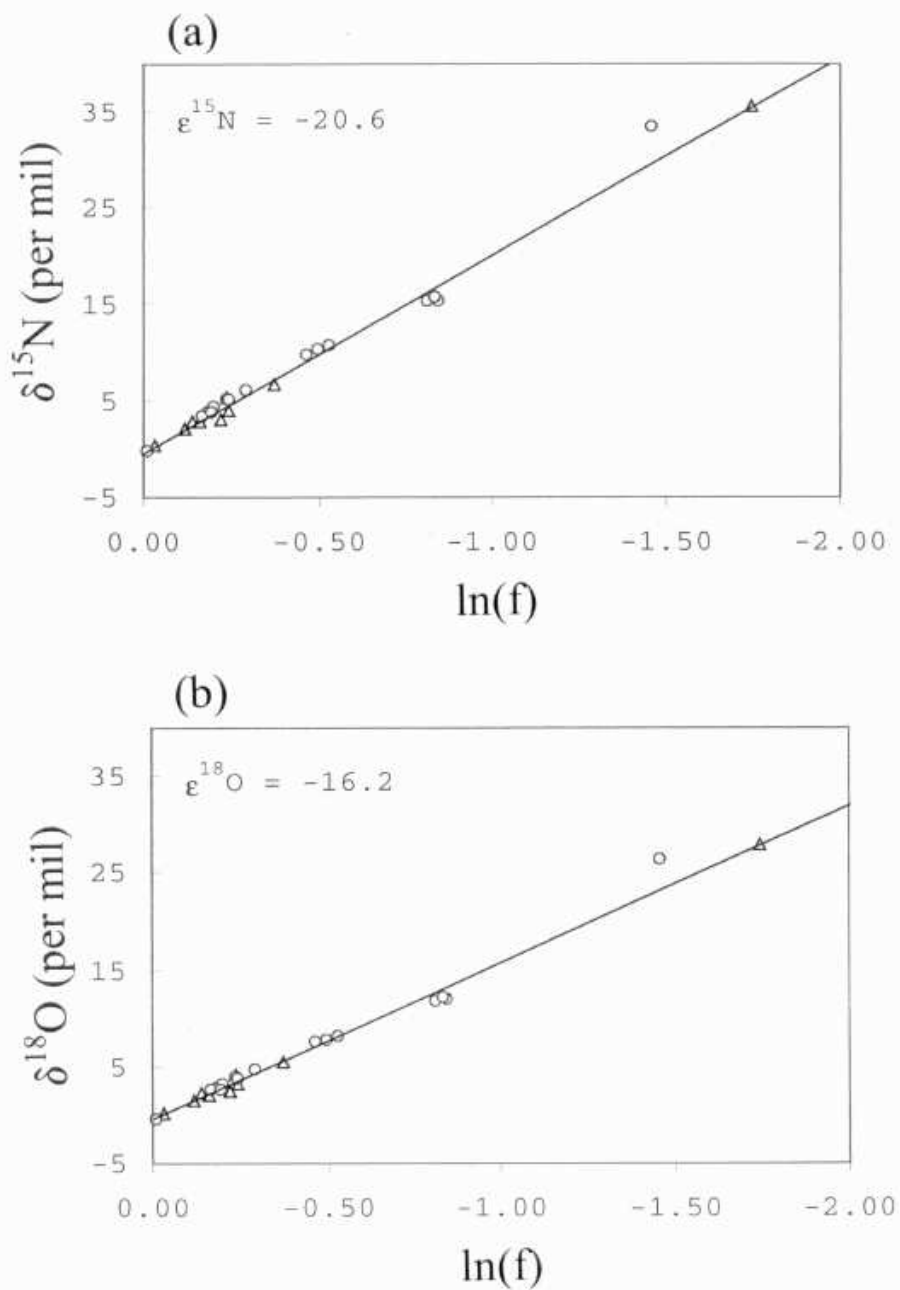


Figure 2.7: Isotopic signatures in the remaining  $N_2O$  following photolysis at 193 nm using Cell 2. Data obtained with Cell 1 are plotted for comparison. (a)  $^{15}N$  compared to  $^{14}N$ ; (b)  $^{18}O$  compared to  $^{16}O$ . The same denotations are used in both (a) and (b). Open triangles: Cell 2 data; open circles: Cell 1 data. The solid lines are Rayleigh model fit through Cell 2 samples only. The derived enrichment factors, in per mil, are marked on the plots.

Table 2.3: Photolysis experiments at 207.5 nm.

Sample #	Duration (minutes)	Pulse Energy (mJ)	N <sub>2</sub> :N <sub>2</sub> O	Residual Fraction	ln(f)	δ <sup>15</sup> N (per mil)	δ <sup>18</sup> O (per mil)	Note
32	90	np	150	0.99	-0.01	-0.1	-0.2	
24	60	0.20	150	0.88	-0.13	5.4	5.3	
34	60	0.45	300	0.85	-0.16	7.3	6.9	
26	120	0.20	150	0.81	-0.21	9.9	9.4	
27	120	0.35	150	0.76	-0.27	12.5	11.9	
29	180	0.26	150	0.72	-0.33	16.0	15.0	
28	180	0.30	150	0.72	-0.33	17.1	16.1	-5° C
31	90	0.18	150	0.82	-0.19	6.6	6.3	70° C
30	480	0.26	150	0.30	-1.21	39.2	36.7	
35	60	0.45	0	0.79	-0.24	6.9	7.0	
33	120	0.35	0	0.67	-0.40	11.5	11.8	

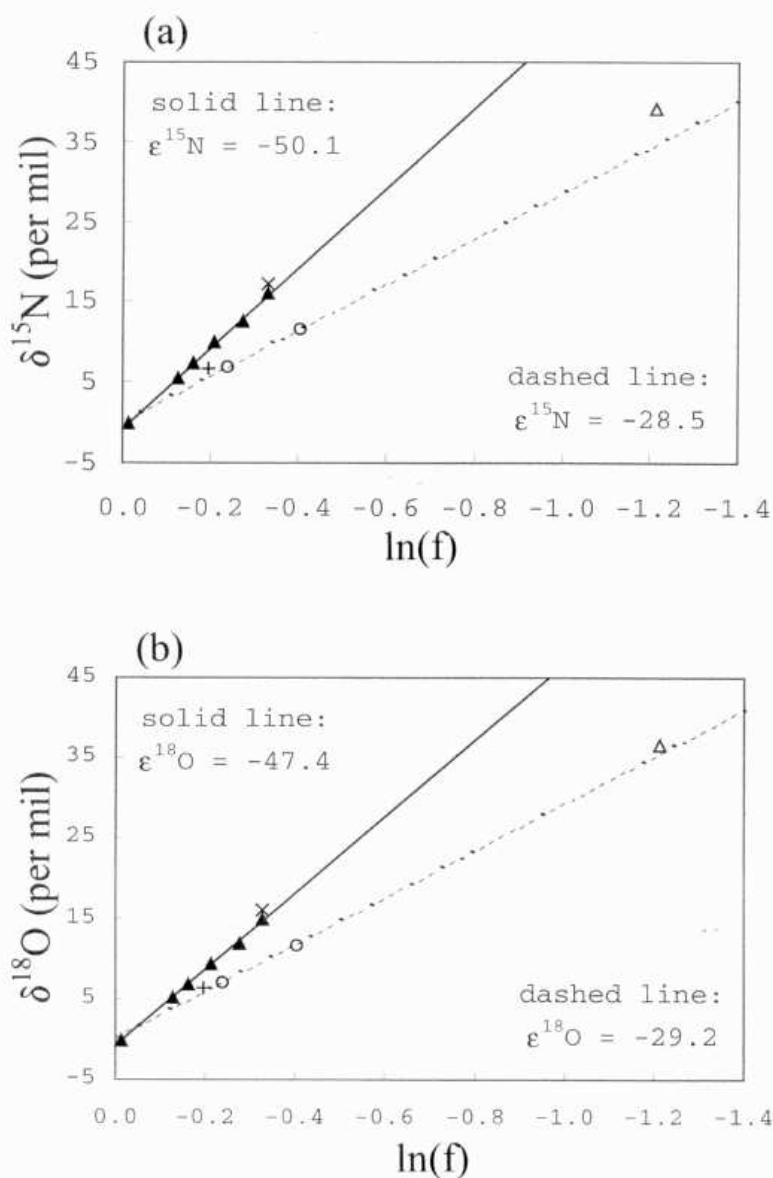


Figure 2.8: Isotopic signatures in the remaining  $\text{N}_2\text{O}$  following photolysis at 207.5 nm. (a)  $^{15}\text{N}$  compared to  $^{14}\text{N}$ ; (b)  $^{18}\text{O}$  compared to  $^{16}\text{O}$ . The same denotations are used in both (a) and (b). Filled triangles: non-photolyzed samples and those with various photolysis extents from 12% to 28%; open triangle: a single sample with 70% photolysis extent; open circles: pure  $\text{N}_2\text{O}$  samples without  $\text{N}_2$  present as a quenching agent; cross: the sample obtained at 268 K; plus: the sample obtained at 343 K. The solid straight line is a Rayleigh model fit of the filled triangle samples. The open circle samples are fitted with a Rayleigh model through origin as represented by the dash line. The derived enrichment factors, in per mil, are marked on the plots.

previous measurements of Johnston *et al.* (15). Sample #30 also supports this conclusion. This sample had an N<sub>2</sub>:N<sub>2</sub>O ratio of 150 and was 70% photolyzed. Its enrichment falls between the presumably fully quenched and zero quenching agent samples.

A crude estimate of the temperature dependence of the fractionation is obtained from two samples, #28 (cross in Figure 2.8) and #31 (plus in Figure 2.8). The enrichment at 268 K is slightly greater than at room temperature while the enrichment at 343 K is less than at room temperature ( $\sim 295$  K). The consistency of the temperature dependent fractionation factors with model calculations will be discussed later.

*211.5 nm and 215.25 nm:* Photolysis experiments at longer wavelengths were also attempted. Because of the rapid drop in the UV cross section of N<sub>2</sub>O towards longer wavelengths, it was difficult to collect sufficient data at  $\lambda \geq 215$  nm, however. Table 2.4 and Table 2.5 include details of the experiments at 211.5 nm and 215.25 nm, respectively. Results from these experiments are shown in Figure 2.9 and Figure 2.10.

These data confirm that larger enrichment occurs at longer wavelengths and that the observed enrichment is robust in regard to multi-photon effects.  $\epsilon^{15}\text{N}$  at 211.5 nm is measured to be -53.5 per mil and  $\epsilon^{18}\text{O} = -50.8$  per mil, while the 215.25 nm experiments give enrichment factors of  $\epsilon^{15}\text{N} = -52.1$  per mil and  $\epsilon^{18}\text{O} = -49.3$  per mil. The latter is quite uncertain as it is based on only three samples with photolysis extent of 9% to 12%. The small photolysis extent and narrow dynamic range suggest that the magnitude of the enrichment observed at 215.25 nm is inconclusive.

Shown in Figure 2.11 is the UV cross section of N<sub>2</sub>O calculated using the temperature-dependent formula recommended by Selwyn *et al.* (37). The inset plot is the high-resolution experimental N<sub>2</sub>O absorption cross section data obtained by Yoshino *et al.* (50), showing vibrational structure at wavelengths shorter than 185 nm. Based on this cross section profile and using the ZPE difference from YM97, the epsilon values for <sup>15</sup>N and <sup>18</sup>O are calculated according to

$$F(\lambda) = \frac{1}{\sigma(\lambda)} \frac{d\sigma(\lambda)}{d\lambda}. \quad (2.5)$$

It is assumed that the cross sections are identical for all isotopomers. The calculated result is shown in Figure 2.12. Also included in the figure are the experimental data for

Table 2.4: Photolysis experiments at 211.5 nm.

Sample #	Duration (minutes)	Pulse Energy (mJ)	N <sub>2</sub> :N <sub>2</sub> O	Residual Fraction	ln(f)	$\delta^{15}\text{N}$ (per mil)	$\delta^{18}\text{O}$ (per mil)
40	90	np	210	0.99	-0.01	0.2	0.6
37	70	0.45	150	0.93	-0.07	4.7	4.2
36	70	0.68	170	0.87	-0.14	6.1	5.0
39	105	0.57	210	0.81	-0.21	10.6	10.4
38	150	0.60	150	0.73	-0.31	17.0	15.3
41	180	0.60	220	0.74	-0.30	16.0	15.7
42	270	0.60	320	0.65	-0.43	23.7	22.9

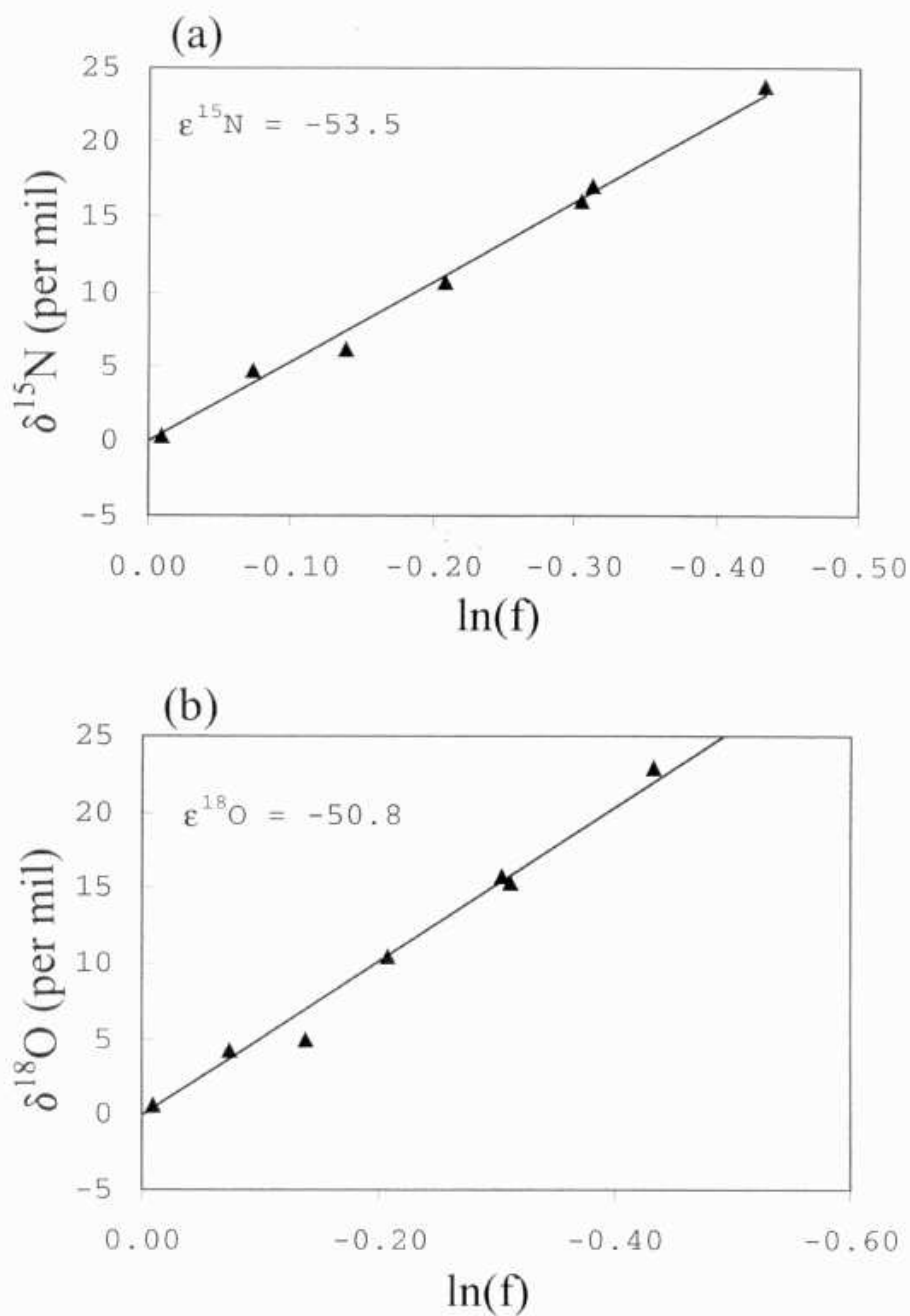


Figure 2.9: Isotopic signatures in the remaining  $N_2O$  following photolysis at 211.5 nm. (a)  $^{15}N$  compared to  $^{14}N$ ; (b)  $^{18}O$  compared to  $^{16}O$ . All the samples are fitted with a Rayleigh model as shown by the solid line. The derived enrichment factors, in per mil, are marked on the plots.

Table 2.5: Photolysis experiments at 215.25 nm.

Sample #	Duration (minutes)	Pulse Energy (mJ)	N <sub>2</sub> :N <sub>2</sub> O	Residual Fraction	ln(f)	$\delta^{15}\text{N}$ (per mil) (per mil)	$\delta^{18}\text{O}$ (per mil) (per mil)
46	np	np	0	0.98	-0.02	0.1	0.2
44	95	0.5	230	0.91	-0.09	6.8	6.8
47	100	0.5	135	0.91	-0.09	4.6	4.4
43	120	0.4	180	0.88	-0.13	5.0	5.1

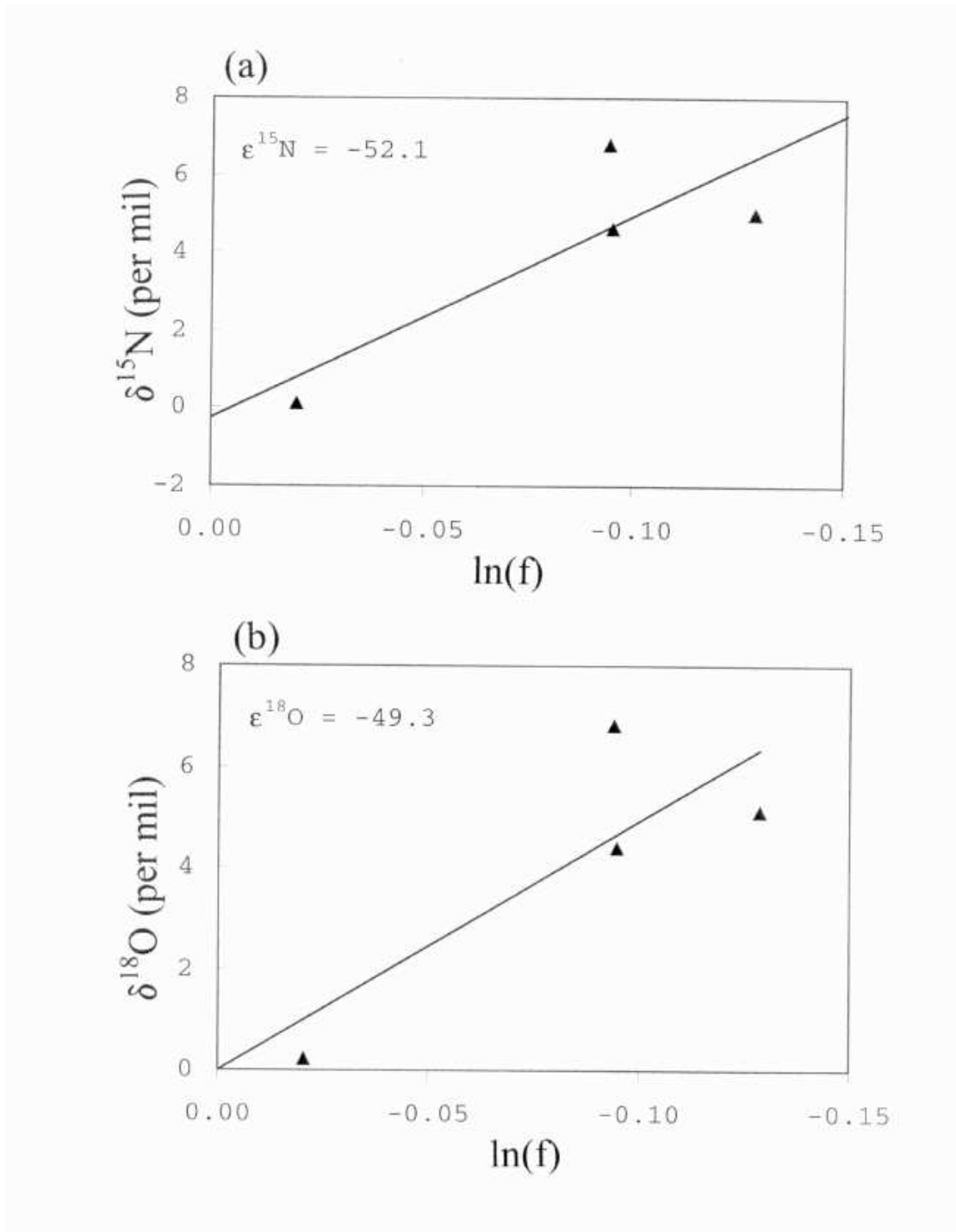


Figure 2.10: Isotopic signatures in the remaining  $\text{N}_2\text{O}$  following photolysis at 215.25 nm. (a)  $^{15}\text{N}$  compared to  $^{14}\text{N}$ ; (b)  $^{18}\text{O}$  compared to  $^{16}\text{O}$ . All samples are fitted with a Rayleigh model. The derived enrichment factors, in per mil, are marked on the plots.

comparison. Of the work performed by other groups, Rockmann *et al.* use the fragment ion technique to study the  $^{15}\text{N}$  positional fractionation of  $\text{N}_2\text{O}$  during photolysis at 193 nm (36), while Turatti *et al.* have analyzed the photolysis samples collected in this thesis with high resolution FTIR spectroscopy (41). It is clear that the trend of the observed heavy isotope enrichment with wavelength is consistent with that predicted by YM97. The enrichment factors observed both in this work and by others are consistently about a factor of two times larger than that calculated for both  $^{15}\text{N}$  and  $^{18}\text{O}$ .

As shown in Figure 2.13, however, the same calculation performed using the laboratory cross section data for  $\text{N}_2\text{O}$  isotopes (38) yields larger enrichment factors, and thus compares more favorably with experimental data at 193 nm and 207 nm. This suggests that the general mechanism proposed by YM97 is indeed responsible for the observed fractionation. The assumption used in the calculation that identical cross sections can be applied to different isotopomers is, however, likely not true. A fully quantitative test will require a comparison between YM97's prediction and laboratory measurements of the isotope-specific cross sections. These remain to be measured at all relevant wavelengths and temperatures.

The temperature dependence observed at 207 nm is qualitatively consistent with the same calculation discussed above. At lower temperature the enrichment is calculated to be larger, as illustrated in Figure 2.14 for  $^{15}\text{N}$ , in agreement with the results from sample #28 and #31 in Table 2.3 and Figure 2.8. The implication of this qualitative relationship for stratospheric  $\text{N}_2\text{O}$  is unclear. Again, isotope-specific cross sections should be obtained at various temperatures. A better understanding of stratospheric  $\text{N}_2\text{O}$  enrichment as a result of photolysis process can then be formed.

### 2.2.3 Atmospheric Implications

The results of this study verify that UV photolysis of  $\text{N}_2\text{O}$  ( $193 \text{ nm} \leq \lambda \leq 215 \text{ nm}$ ) yields significant isotopic enrichment in the residual gas. Furthermore, a comparison of the enrichments of  $^{15}\text{N}$  to  $^{18}\text{O}$  yields ratios of slightly greater than unity. This is nearly identical to the ratio of the enrichments observed in stratospheric samples (33) and close to that predicted by YM97. It is clear that photolysis is the mechanism responsible for the observed stratospheric enrichments and that the standard model of stratospheric  $\text{N}_2\text{O}$  chemistry is essentially complete. While the absolute magnitude of the fractionation observed in the laboratory is significantly different from that predicted by YM97, the general concept of

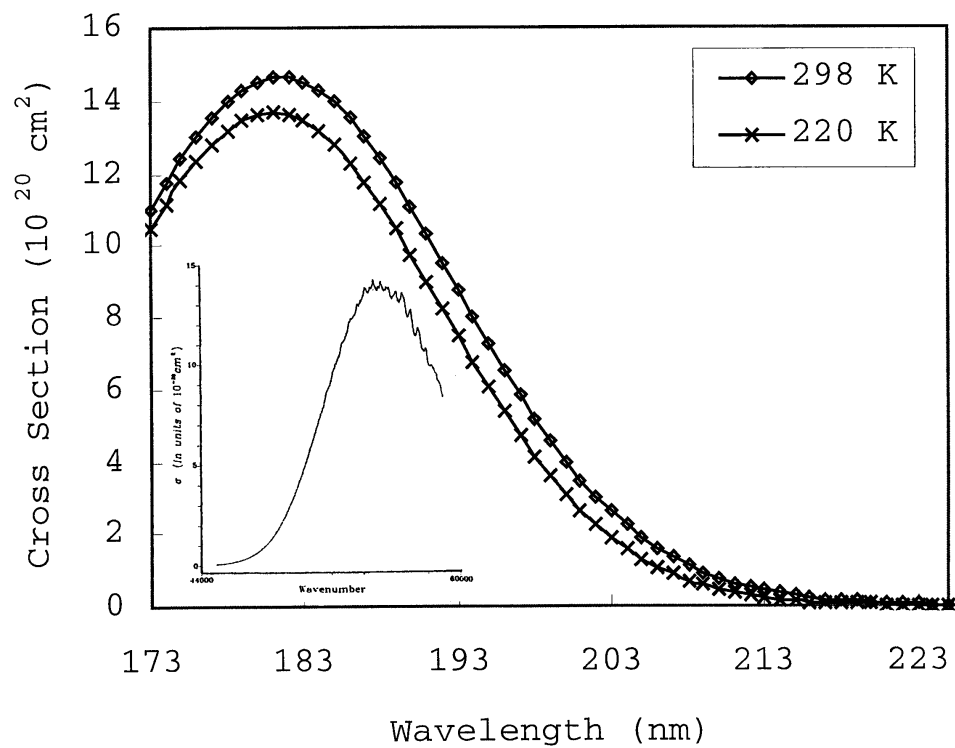


Figure 2.11: Calculated cross sections at 298 and 220 K for N<sub>2</sub>O using the temperature-dependent formula from Selwyn *et al.* (37). The inset plot is the high-resolution experimental N<sub>2</sub>O absorption cross section data obtained by Yoshino *et al.* (50), showing vibrational structure at wavelengths shorter than 185 nm.

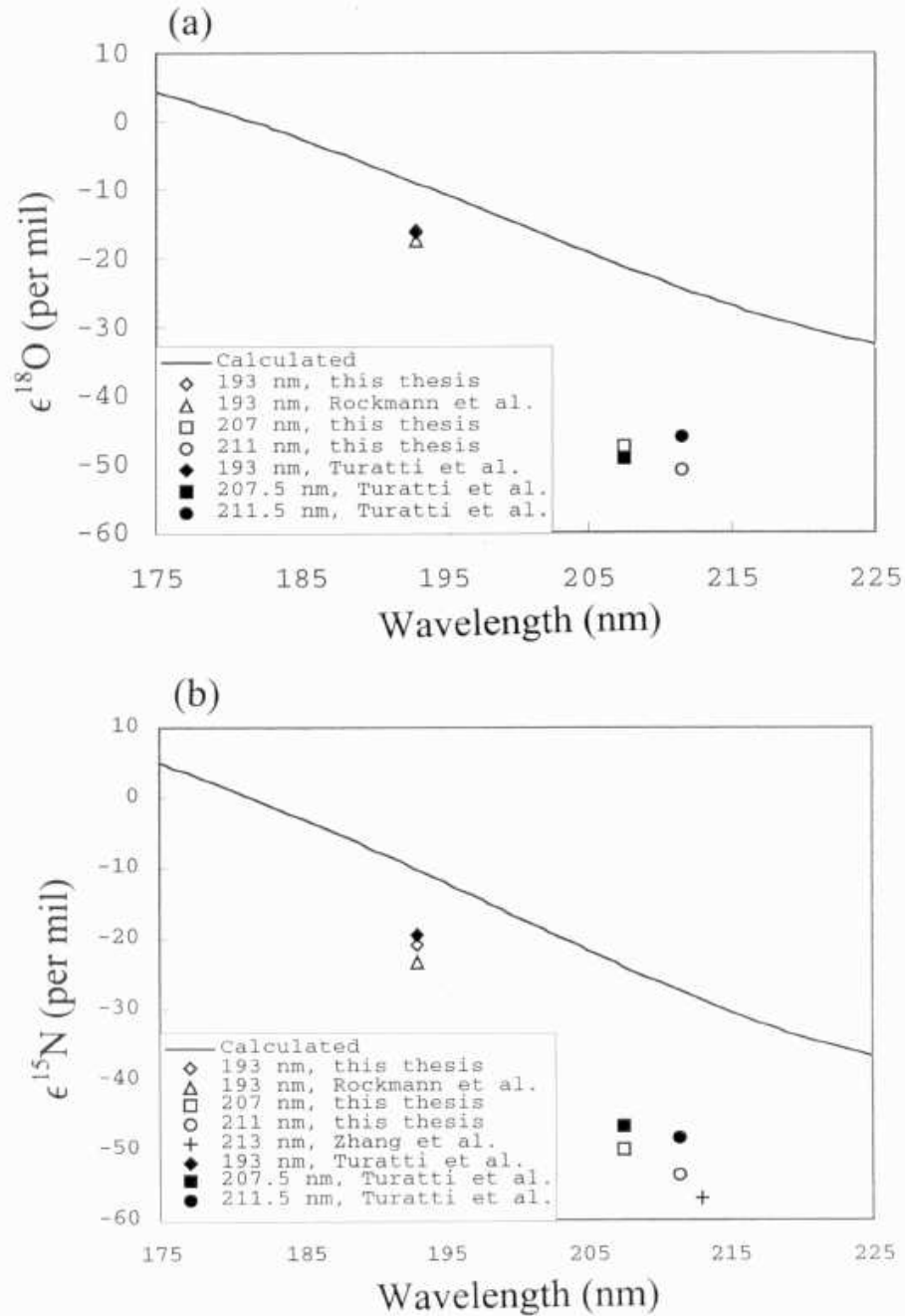


Figure 2.12: Comparison of the calculated and measured enrichment factors. (a)  $\epsilon^{18}\text{O}$ ; (b)  $\epsilon^{15}\text{N}$ .

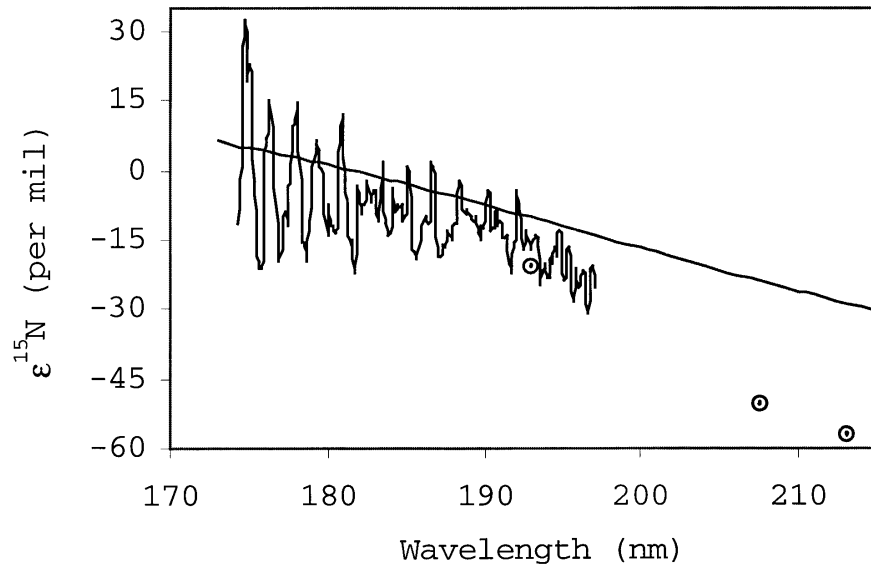


Figure 2.13: Comparison of the measured enrichment factors for  $^{15}\text{N}$  (shown in open circles with a dot at the center) with those derived from experimental  $\text{N}_2\text{O}$  isotopic cross section data taken from Selwyn *et al.* (38) (the curve). Also plotted is the calculation from Figure 2.12 (the line across the plot).

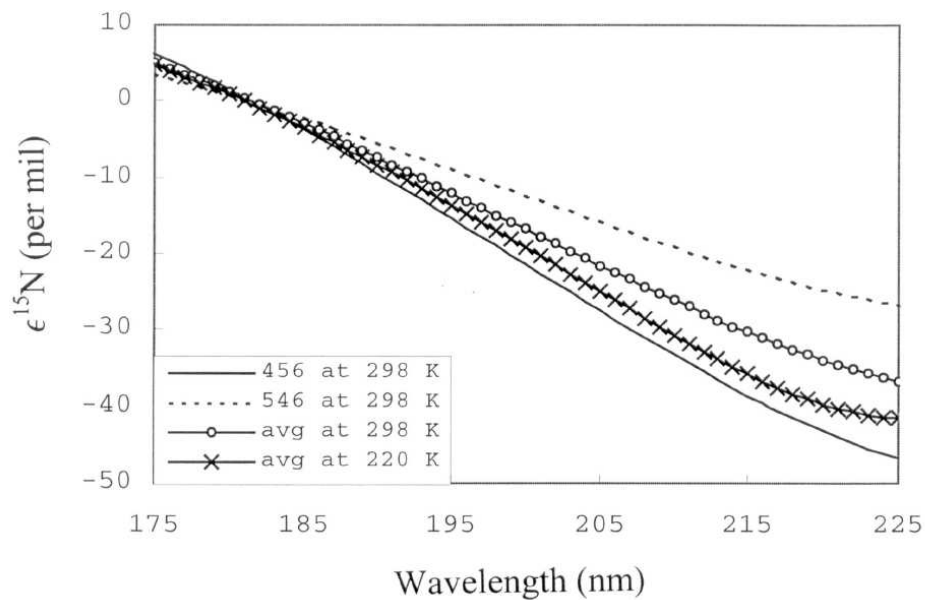


Figure 2.14: Calculated  $\epsilon^{15}\text{N}$  using the cross sections in Figure 2.11 at 298 and 220 K. “456” stands for  $^{14}\text{N}^{15}\text{N}^{16}\text{O}$  while “546” for  $^{15}\text{N}^{14}\text{N}^{16}\text{O}$ . “avg” is the arithmetic average of “456” and “546”.

enrichment being caused by a spectral shift with isotopic substitution is still a valid and likely mechanism. A more rigorous theoretical treatment of the zero point energy shifts proposed by YM97, including non-Born-Oppenheimer effects, multiple excited states and dipole moment surface variations, might yield a more quantitative agreement.

The absolute magnitude of the laboratory enrichments are not in agreement when compared to the enrichments observed earlier in the lower stratospheric samples (33), but are similar to recent stratospheric measurements obtained from higher altitudes (12). This suggests that transport both from the higher altitudes (higher fractionation due to more UV photolysis) and the troposphere (no photolysis air) play a role in the isotopic concentration of stratospheric N<sub>2</sub>O. To determine how stratospheric mixing processes might influence the observed isotopic enrichment factors for a tracer which has a decay constant  $\lambda_A$  and no *in situ* production, we consider the one-dimensional (1D) diffusion-limited case where the steady state continuity equation for trace species A is reduced to

$$K_D \frac{\partial^2[A]}{\partial z^2} - \lambda_A \frac{\partial[A]}{\partial z} = 0, \quad (2.6)$$

$K_D$  being the eddy diffusion coefficient and  $z$  being the height above the tropopause. With the boundary conditions  $A = A_0$  at  $z(0)$  and  $A = 0$  at  $Z(\infty)$ . Eq. (2.6) has the solution

$$A = A_0 \exp\left(-z \sqrt{\frac{\lambda_A}{K_D}}\right). \quad (2.7)$$

If B is the isotopically substituted species, then  $R = B/A$  and

$$\frac{R}{R_0} = \exp\left[-z \left(\frac{\sqrt{\lambda_B} - \sqrt{\lambda_A}}{\sqrt{K_D}}\right)\right]. \quad (2.8)$$

Recognizing that  $f = A/A_0$  and  $\ln(f) = -z \sqrt{\lambda_A/K_D}$ , Eq. (2.8) yields

$$R = R_0 f^{(\sqrt{\lambda_B/\lambda_A}-1)}$$

which is of the form of Eq. (2.1). Since  $\alpha$  is equal to the ratio of the heavy-to-light reaction rates, it is apparent that the effective fractionation in this 1D diffusion-controlled system is

$$\alpha_{\text{eff}} = \sqrt{\frac{\lambda_B}{\lambda_A}}, \quad \text{or} \quad \alpha_{\text{eff}} = \alpha^{1/2};$$

and, since  $\alpha = (1 + \epsilon/1000)$ ,  $\epsilon_{\text{eff}} \sim \epsilon/2$  (see also Eriksson (9)). If we consider the fractionation at 205 nm to be representative of the integrated stratospheric fractionation (as in YM97) and further assume a linear dependence between the laboratory results at 193 nm and 207 nm, the effective enrichment factors are then  $\epsilon_{15,\text{eff}} = -21.8$  per mil and  $\epsilon_{18,\text{eff}} = -20.4$  per mil, in much closer agreement with the stratospheric measurements of Rahn *et al.* (33). A choice of 200 nm as the representative wavelength brings the effective enrichments into even closer agreement with  $\epsilon_{15,\text{eff}} = -16.7$  per mil and  $\epsilon_{18,\text{eff}} = -15.1$  per mil. In either case, the actual fractionation measured in the laboratory ( $\alpha$ ) far exceeds the observed *in situ* fractionation as it must in order to account for eddy diffusion in the stratosphere as described above.

In regard to the wavelength chosen to be representative of the integrated stratospheric fractionation, it is important to note that the stratospheric isotopic signature is the result of the mid-stratosphere radiation field integrated over the range of N<sub>2</sub>O UV absorption and that the polynomial expression used by YM97 for the cross section spectral dependence is only an approximation. Indeed, a significant amount of vibrational structure is seen in the cross section at wavelengths below 190 nm (38) which results in multiple curve crossings with small spectral shifts. Since the YM97 enrichment factors change sign below a cross section maximum, and since there are well defined transmission windows in the Schumann-Runge bands, enrichments of opposite sign below 190 nm may compensate for the large negative  $\epsilon$ 's at longer wavelengths. The ratio of the measured enrichment factors for <sup>15</sup>N and <sup>18</sup>O at 193 nm is rather different than those measured at  $\lambda > 207$  nm, and may in part be due to the continuation of such vibrational structure, structure that is not accounted for in the spectral function of Selwyn *et al.* (37) nor in the YM97 model, yet which is clearly present in the laboratory cross section data (38; 50). Since this structure is dominated by the  $\nu_2 = 1$  mode, however, such differences will be much reduced at 220 K.

The fact that one of the dominant isotopic signatures in atmospheric nitrous oxide arises from UV photolysis not only obviates the need for “exotic” chemistry, it makes this species a powerful tool for addressing important issues in global climate change. For example, it should provide a unique signature to distinguish between fractionation occurring in the

upper atmosphere and that resulting from biological or anthropogenic processes, thereby helping in N<sub>2</sub>O budgetary analyses and quantifying the flux of stratospheric air into the troposphere. Further, because the photolytic isotope fractionation only occurs in the mid-to upper-stratosphere, the extent to which the integrated photolytic fractionation exceeds the *in situ* stratospheric observations may help to determine the degree of mixing between “aged” and “new” stratospheric air.

## 2.3 Fractionation of $^{14}\text{N}^{15}\text{N}^{16}\text{O}$ and $^{15}\text{N}^{14}\text{N}^{16}\text{O}$ During Photolysis at 213 nm

[Section 2.3.1 and 2.3.2 are part of “Fractionation of  $^{14}\text{N}^{15}\text{N}^{16}\text{O}$  and  $^{15}\text{N}^{14}\text{N}^{16}\text{O}$  During Photolysis at 213 nm” by Zhang, H., P. O. Wennberg, V. H. Wu, and G. A. Blake, *Geophys. Res. Lett.*, 27, 2481-2484, 2000. Copyright by the American Geophysical Union.]

### 2.3.1 Experimental

Figure 2.15 presents a schematic of our experimental set up. UV photons are generated by a Nd:YAG laser, while IR spectra are collected with an FTIR spectrometer. The general experimental procedure is to photolyze the  $\text{N}_2\text{O}$  sample continuously while taking IR spectra to monitor the concentration of the isotopomers.

The photolysis is conducted at 212.8 nm (abbreviated as 213 nm hereafter). This wavelength is chosen primarily because it is conveniently produced by the 5<sup>th</sup> harmonic generation of a Nd:YAG laser. The fundamental output of the YAG laser (Infinity<sup>TM</sup> 40-100, Coherent) is first doubled to 532 nm. The 532 nm is then doubled using a 2-mm thick BBO crystal ( $C_1$ ). In a second thin BBO crystal ( $C_2$ ), 266 nm light is mixed with the residual 1064 nm radiation to generate 213 nm pulses. The two crystals are cut for type I phase matched 4<sup>th</sup> and 5<sup>th</sup> harmonic generation of the 1064 nm fundamental. A single quartz PB prism is used to separate 213 nm from the other wavelengths, which are intercepted by beam stops.

The photolysis beam enters the FTIR spectrometer (Magna-IR 560 from Nicolet) through a quartz window ( $W_1$ ) after the 45° turning mirror ( $M_1$ ). It passes into the sample compartment aperture at a steep angle and is redirected by a 0° mirror ( $M_2$ ) towards a 45° mirror ( $M_3$ ). Mirror  $M_3$  and another 0° mirror ( $M_4$ ) together pass the UV beam through the sample cell twice. The exiting beam is intercepted by the  $M_3$  mirror mount. All four mirrors ( $M_1$ ,  $M_2$ ,  $M_3$  and  $M_4$ ) are 213 nm high reflectors from Coherent. The spectrometer is oriented so that reflective losses of the photolysis beam on the windows are minimized. During the experiment, the stability of the UV power is monitored with a photodetector (UDT-555UV) through the reflection off window  $W_1$ .

The sample cell is made of thick-wall Pyrex glass. It has an inner diameter of  $\sim 4$  cm and a length of 15 cm.  $\text{CaF}_2$  is chosen as the window material because it is transparent in

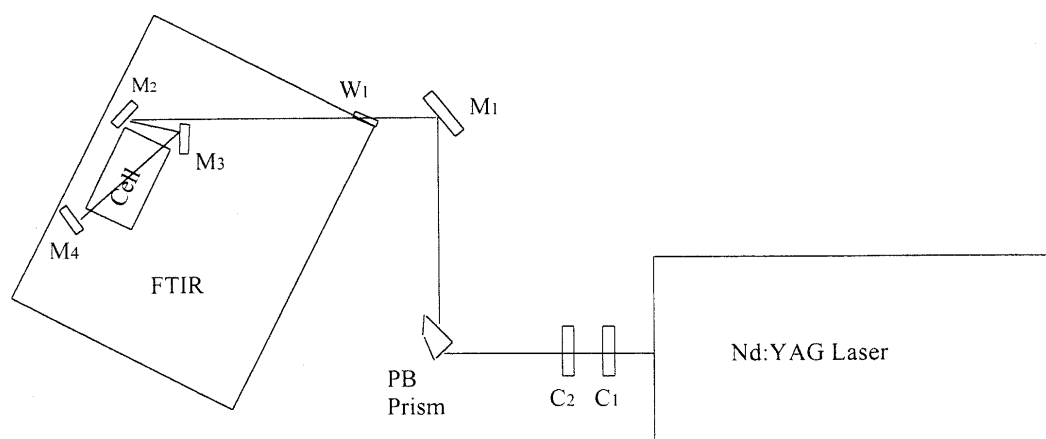


Figure 2.15: Light from a Nd:YAG laser is directed into the sample compartment of an FTIR spectrometer via a side port. Gas samples are located inside the cell.

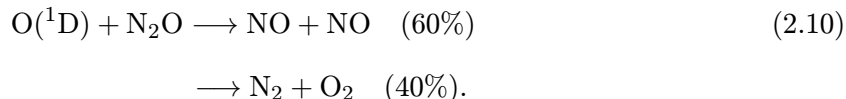
Table 2.6: Partial pressures of different gases in the sample mixtures used in the 213 nm photolysis experiments.

Exp.	$^{14}\text{N}^{14}\text{NO}$ (torr)	$^{14}\text{N}^{15}\text{NO}$ (torr)	$^{15}\text{N}^{14}\text{NO}$ (torr)	Quenching Gas (torr)
I	5	6	5.5	460 ( $\text{N}_2$ ) 280 ( $\text{CO}_2$ )
II	6	4	-	750 ( $\text{N}_2$ )
III	6	-	5	750 ( $\text{N}_2$ )

both the IR and UV. The two windows are glued on to the cell with Torr Seal (Varian) at slightly different wedge angles to minimize etaloning.

Three isotopically labeled  $\text{N}_2\text{O}$  samples are used. A pure  $\text{N}_2\text{O}$  sample with natural isotopic abundance is used for  $^{14}\text{N}^{14}\text{N}^{16}\text{O}$  (99%+). Separate samples of  $^{14}\text{N}^{15}\text{N}^{16}\text{O}$  (98%+) and  $^{15}\text{N}^{14}\text{N}^{16}\text{O}$  (98%+) mixed with  $\text{N}_2$  (99.999%) at an  $\text{N}_2:\text{N}_2\text{O}$  ratio of 40 are purchased from Cambridge Isotopes. The partial pressures of the different gases in the sample mixtures used for the three photolysis experiments are listed in Table 2.6. All the experiments are conducted at a total pressure of approximately 760 torr and at room temperature.

Photolysis (2.9) of  $\text{N}_2\text{O}$  produces  $\text{O}(^1\text{D})$ , which reacts with  $\text{N}_2\text{O}$  (2.10):



To prevent  $\text{N}_2\text{O}$  from being oxidized (2.10),  $\text{O}(^1\text{D})$  quenching by  $\text{N}_2$  or  $\text{CO}_2$  is necessary:



In Exp. II and III, only one rare  $\text{N}_2\text{O}$  isotopomer is involved and  $\text{N}_2$  serves as the quenching gas. For an  $\text{N}_2:\text{N}_2\text{O}$  ratio of 75, less than 3% of  $\text{O}(^1\text{D})$  atoms are expected to undergo reaction (2.10) due to quenching by  $\text{N}_2$  (2.11) (7). In Exp. I,  $\text{N}_2$  quenching is limited by the total cell pressure and the  $\text{N}_2:\text{N}_2\text{O}$  ratio of 40 in both the  $^{14}\text{N}^{15}\text{N}^{16}\text{O}$  and  $^{15}\text{N}^{14}\text{N}^{16}\text{O}$  samples. In this case,  $\text{CO}_2$ , which is four times more efficient than  $\text{N}_2$  at quenching  $\text{O}(^1\text{D})$ , is used as an additional quencher.

The concentration of  $\text{N}_2\text{O}$  is monitored via the Q-branch of the  $\nu_2+\nu_3$  combination band, which lies at  $2798 \text{ cm}^{-1}$  for  $^{14}\text{N}^{14}\text{N}^{16}\text{O}$ . Shown in Figure 2.16 are the  $\nu_2+\nu_3$  spectra of the three  $\text{N}_2\text{O}$  isotopomers. They are taken at  $0.5 \text{ cm}^{-1}$  resolution with an MCT/A liquid nitrogen cooled detector. This band is chosen for several reasons. First, it sits in a region free of interference from ambient  $\text{H}_2\text{O}$  and  $\text{CO}_2$  absorption (the spectrometer is

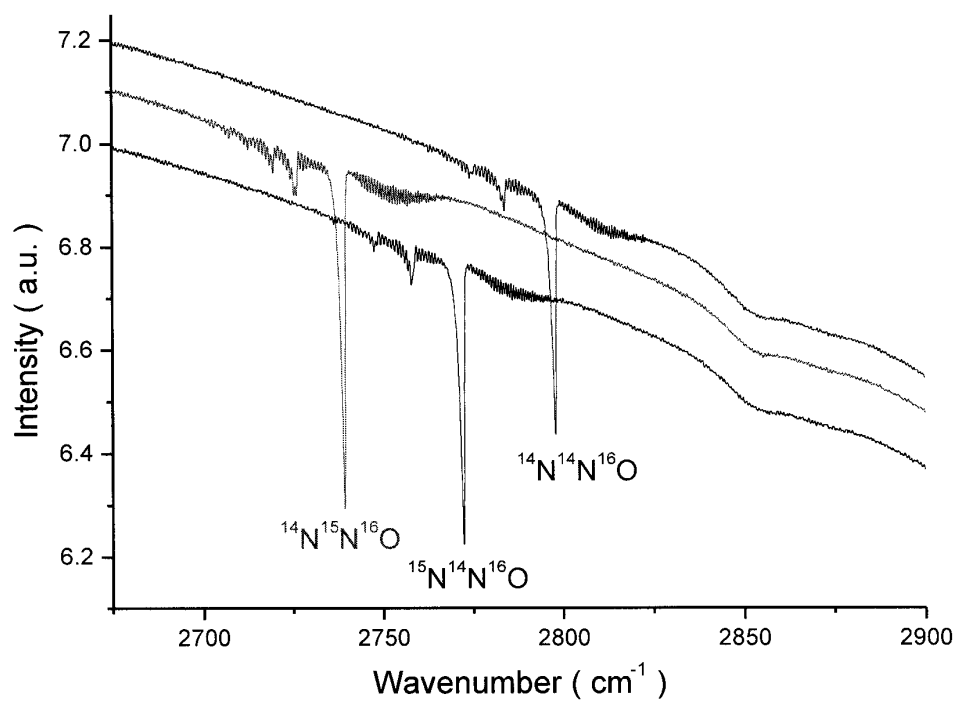


Figure 2.16: FTIR spectra of the three N<sub>2</sub>O isotopomers, taken between 2650 cm<sup>-1</sup> and 2900 cm<sup>-1</sup>, at 0.5 cm<sup>-1</sup> resolution.

nitrogen purged). Second, the peaks for the isotopomers are shifted with respect to each other by  $\sim 30 \text{ cm}^{-1}$  and the small amount of cross interference among them can be easily accounted for. Third, at one atmosphere pressure, the Q-branch is collision-broadened and is fully resolved at  $0.5 \text{ cm}^{-1}$  resolution. This leads to linear Beer's law behavior, which is demonstrated in this apparatus by preparing  $\text{N}_2\text{O}$  samples of known concentration using manometry. At  $0.5 \text{ cm}^{-1}$  resolution, a high S/N can be achieved in approximately 30 minutes (see below for an explanation of the photolysis time scale). For example, in Exp. II, the S/N is more than 100 for the initial spectrum. The signal level is calculated at the center of the Q-branch for  $^{14}\text{N}^{14}\text{N}^{16}\text{O}$ , while the noise is the root-mean-square (RMS) noise in the baseline between 2850 and 2900  $\text{cm}^{-1}$ . Similar S/N is achieved in the other two experiments.

Approximately 60 mW (2 mJ at 30 Hz pulse repetition rate) of 213 nm light are used. Over  $\sim 11$  hours, 70% of the initial  $\text{N}_2\text{O}$  is removed. FTIR scans are co-added, producing one data point every 30 minutes. In addition, spectra are taken before the photolysis to test the spectral processing protocol and data fitting. To monitor any post-photolysis processes, IR spectra are recorded after the photolysis laser is turned off. For the background, spectra of the same pressure of pure  $\text{N}_2$  (in Exp. II and III) or the same mixture of  $\text{N}_2$  and  $\text{CO}_2$  (in Exp. I) are acquired.

The concentration of the isotopomers is derived by first normalizing the co-added spectra against the background. The integrated absorbance of the Q-branch is determined and the retrieved signal is corrected for the small amount of absorption from the other isotopomers.

### 2.3.2 Results and Discussion

Figure 2.17 illustrates the observed fractionation. The slope of the linear fit to the data gives the fractionation factor in a Rayleigh model (10). The results from the three experiments are as follows:  $\epsilon(^{14}\text{N}^{15}\text{N}^{16}\text{O} / ^{14}\text{N}^{14}\text{N}^{16}\text{O}) = -73 \pm 5$  per mil and  $\epsilon(^{15}\text{N}^{14}\text{N}^{16}\text{O} / ^{14}\text{N}^{14}\text{N}^{16}\text{O}) = -41 \pm 10$  per mil. The uncertainty results primarily from systematic error introduced in defining the spectral baseline during data processing. The  $\text{N}_2\text{O}$  band is on a sloping region of the IR intensity as shown in Figure 2.16. A  $\text{NO}_2$  band, discussed below, is superimposed nearby on the short-wavelength side of the  $\text{N}_2\text{O}$   $\nu_2 + \nu_3$  band. These complicate the spectral analysis. Different techniques for inferring the baseline have been performed and various reasonable assumptions have produced the assigned uncertainty.

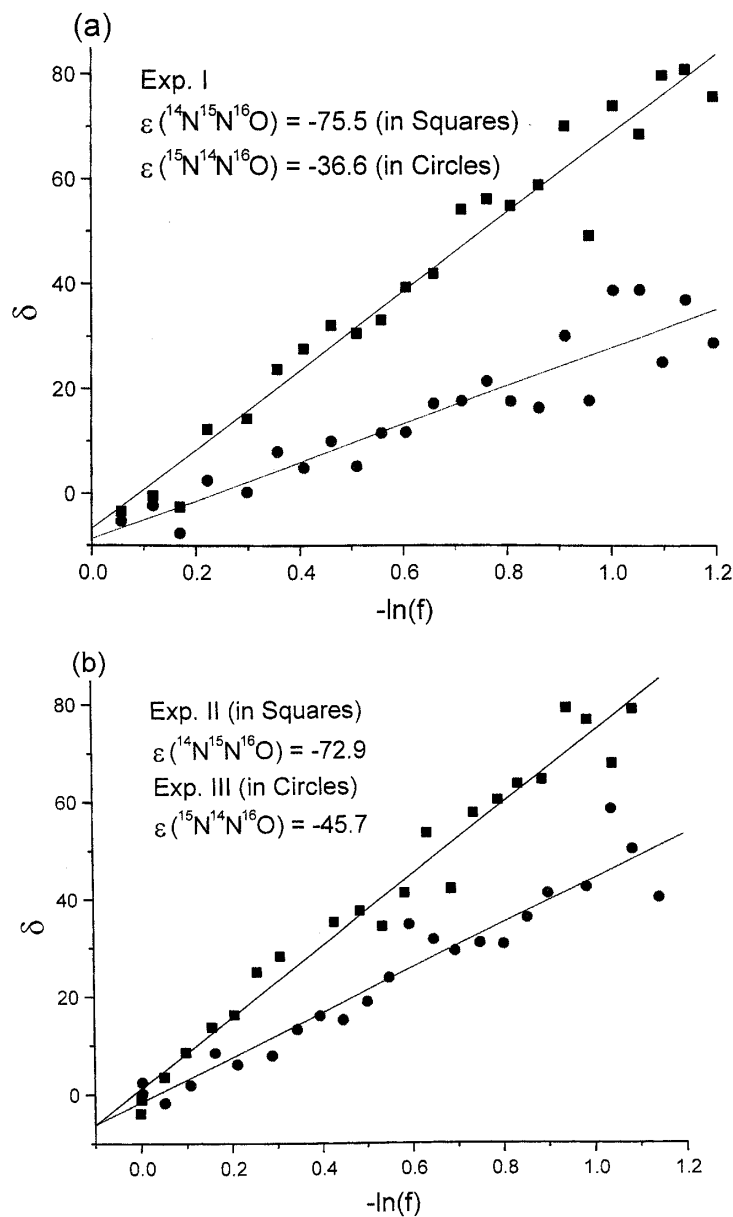


Figure 2.17: The fractionation data from 213 nm photolysis, fitted to a Rayleigh fractionation model.  $\delta = (R_i / R_{\text{std}} - 1) \times 1000$ , where the R's are the slow-to-fast photolysis isotopic ratios.  $R_{\text{std}}$  is for the pre-photolysis samples and  $R_i$  is for the photolyzed samples.  $f$  is the fraction of  $\text{N}_2\text{O}$  remaining.  $\epsilon(^{15}\text{N}^{14}\text{N}^{16}\text{O}) = \epsilon(^{15}\text{N}^{14}\text{N}^{16}\text{O} / ^{14}\text{N}^{14}\text{N}^{16}\text{O})$  and  $\epsilon(^{14}\text{N}^{15}\text{N}^{16}\text{O}) = \epsilon(^{14}\text{N}^{15}\text{N}^{16}\text{O} / ^{14}\text{N}^{14}\text{N}^{16}\text{O})$ . (a) In Experiment I, three  $\text{N}_2\text{O}$  isotopomers are photolyzed; (b) In Experiment II, a mixture of  $^{14}\text{N}^{15}\text{N}^{16}\text{O}$  and  $^{14}\text{N}^{14}\text{N}^{16}\text{O}$  is photolyzed; while in Experiment III, a mixture of  $^{15}\text{N}^{14}\text{N}^{16}\text{O}$  and  $^{14}\text{N}^{14}\text{N}^{16}\text{O}$  is photolyzed.

The arithmetic average of  $\epsilon(^{14}\text{N}^{15}\text{N}^{16}\text{O} / ^{14}\text{N}^{14}\text{N}^{16}\text{O})$  and  $\epsilon(^{15}\text{N}^{14}\text{N}^{16}\text{O} / ^{14}\text{N}^{14}\text{N}^{16}\text{O})$  gives  $-57 \pm 15$  per mil for  $\epsilon(^{15}\text{N} / ^{14}\text{N})$  at 213 nm. This result is consistent with those reported by Rahn *et al.* (34), who observed for  $\epsilon(^{15}\text{N} / ^{14}\text{N})$  values of -18.4 per mil at 193 nm and -48.7 per mil at 207 nm.

We have assumed that all  $\text{N}_2\text{O}$  loss is due to reaction (2.9); processes other than reaction (2.9) that destroy  $\text{N}_2\text{O}$  would affect our interpretation. One possible interference is reaction (2.10), the reaction of  $\text{O}(^1\text{D})$  with  $\text{N}_2\text{O}$  producing  $\text{NO}$ . The  $\text{NO}$  can undergo further conversion to  $\text{NO}_2$  in the cell. We have observed the formation of small amounts of  $\text{NO}$  and  $\text{NO}_2$  in each of the three experiments.  $\text{NO}$  is monitored via its absorption band near  $1875 \text{ cm}^{-1}$ ,  $\text{NO}_2$  is monitored at  $2907 \text{ cm}^{-1}$  and  $1617 \text{ cm}^{-1}$ . The photolysis of  $\text{NO}_2$ , whose cross section at 213 nm is more than 1000 times larger than that of  $\text{N}_2\text{O}$  (7), keeps its concentration low while the cell is illuminated with laser light. Once the photolysis ends, however, the  $\text{NO}$  is converted into  $\text{NO}_2$  on the time scale of a few hours. Post-photolysis spectra reveal that the conversion of  $\text{NO}$  into  $\text{NO}_2$  is close to unity. By comparing the photolysis spectra with reference spectra of  $\text{NO}$  and  $\text{NO}_2$ , we determine that less than 2% of the  $\text{N}_2\text{O}$  destruction in our experiments has occurred via reaction (2.10). This is consistent with the expected quenching rates. Other processes that form  $\text{N}_2\text{O}$  have also been considered. Among them, the three-body reaction of  $\text{N}_2 + \text{O}(^1\text{D})$  to re-form  $\text{N}_2\text{O}$  is extremely slow (7). Exp. II and III provide a test of whether the photolysis of  $^{14}\text{N}^{15}\text{N}^{16}\text{O}$  produces  $^{15}\text{N}^{14}\text{N}^{16}\text{O}$  and vice versa. At over 70% photolysis yield, no formation of  $^{15}\text{N}^{14}\text{N}^{16}\text{O}$  is observed from the photolysis of  $^{14}\text{N}^{15}\text{N}^{16}\text{O}$  and vice versa.

Qualitatively, the observed isotopomer-specific fractionations scale with the ZPE differences noted by YM97. The magnitude of the fractionations found in this experiment (and Rahn *et al.*'s (34)), however, is significantly larger than predicted by YM97. It appears that the simple ZPE model does not fully account for the observed fractionation. There are a number of reasons why this might be the case. At 298 K, close to 90% of the  $\text{N}_2\text{O}$  is in the ground vibrational state (000) while about 10% is in the first excited bending mode (010). Photodissociation dynamics studies ((28) and refs therein) have shown that the photolysis of  $\text{N}_2\text{O}$  (reaction (2.9)) occurs mainly via an orbitally forbidden but vibronically allowed transition through a bent excited state. Therefore, the vibrationally excited bending states of  $\text{N}_2\text{O}$  have much larger Franck-Condon overlap with the dissociative state than does the (000) mode. This is corroborated by the large observed temperature dependence of the

$\text{N}_2\text{O}$  cross section ((20) and refs therein). By deconvolving the cross section data at 225 and 296 K (37) into contributions from the (000) and (010) modes, we calculate that the 213 nm cross section of  $\text{N}_2\text{O}$  (010) is approximately 15 times larger than that of  $\text{N}_2\text{O}$  (000). This implies that, although only 10% of the  $\text{N}_2\text{O}$  molecules are in the first excited bending mode (010) at 298 K, more than 50% of the photolysis at 213 nm occurs via the excited vibrational states. The changes in the potential energy surface for various  $\text{N}_2\text{O}$  isotopomers are different for the two vibrational modes, which leads to different wavelength shifts of the cross sections according to YM97. Therefore, including the vibrationally “hot” molecules in the fractionation calculation is necessary for a quantitative comparison to the experimental results.

The preceding argument implicitly assumes that the photodissociation of  $\text{N}_2\text{O}$  occurs via the repulsive  $\text{B}^1\Delta$  electronic state, as YM97 did in light of the available data at that time. As Neyer *et al.* (28) have demonstrated, however, the dynamics of this photodissociation are more complex than previously thought, with more than one electronic state involved in the excitation/dissociation. It is possible that the two different ground state vibrational modes may have distinct coupling with the upper states, which will further complicate the spectroscopy.

The large differences in the UV cross sections of the various  $\text{N}_2\text{O}$  isotopomers observed in this study support YM97’s suggestion that this mechanism is responsible for the isotopic fractionation observed in the stratosphere. A fully quantitative test of this theory, however, requires accurate wavelength and temperature dependent differential cross sections for these compounds; the use of simple theoretical models for prediction of these cross sections has been ruled out by this study and the previous work of Rahn *et al.* (34). The difference in the cross sections of the isotopomers examined here is large enough that a classical Beer’s law study of the isotopomers (which are available commercially in high purity) can provide the required spectroscopic data.

### 2.3.3 Comparison with Recent Results from Other Groups

In recent years, there have been a flurry of studies on the  $\text{N}_2\text{O}$  isotopic fractionations sparked by the work of YM97. In this section, we compare our experimental results on the fractionation of  $^{14}\text{N}^{15}\text{N}^{16}\text{O}$  and  $^{15}\text{N}^{14}\text{N}^{16}\text{O}$  with those from other groups.

In Figure 2.18,  $\epsilon(^{14}\text{N}^{15}\text{N}^{16}\text{O} / ^{14}\text{N}^{14}\text{N}^{16}\text{O})$  and  $\epsilon(^{15}\text{N}^{14}\text{N}^{16}\text{O} / ^{14}\text{N}^{14}\text{N}^{16}\text{O})$  measured at

different wavelengths are presented. Rockmann *et al.* uses the fragment ion technique to study the  $^{15}\text{N}$  positional fractionation of  $\text{N}_2\text{O}$  during photolysis at 193 nm (36). Turatti *et al.* have analyzed the photolysis samples collected in this thesis with high resolution FTIR spectroscopy (41). These data have confirmed the isotopomer-specific fractionations and its wavelength dependence predicted by YM97. In general, our measurement is consistent with other work; however, it is clear that there are large uncertainties in the ratio of  $\epsilon(456)/\epsilon(546)$ . Further measurements and exchange of calibration standards between different groups should help resolve the differences.

General agreement between different measurements can also be seen in Figure 2.19 where  $\epsilon(^{15}\text{N}^{14}\text{N}^{16}\text{O} / ^{14}\text{N}^{15}\text{N}^{16}\text{O})$  is plotted along with the calculated values. All the laboratory measurements are about twice as large as the calculation except the measurement by Rockmann *et al.*, who observed fractionation factors approximately three times those calculated (36). There have also been two observations of the  $^{15}\text{N}$  positional fractionation in the atmosphere (12; 47). The observations of lower stratospheric air by Yoshida *et al.* (47) give  $\epsilon(^{15}\text{N}^{14}\text{N}^{16}\text{O} / ^{14}\text{N}^{15}\text{N}^{16}\text{O}) = 18.7$  per mil, while Griffith *et al.* (12) report a value of 29.8 per mil based on data obtained at higher altitudes. Clearly, the measurements of  $^{15}\text{N}$  positional fractionation have added one more useful isotopic signature that can be used to constrain the global budget of  $\text{N}_2\text{O}$ .

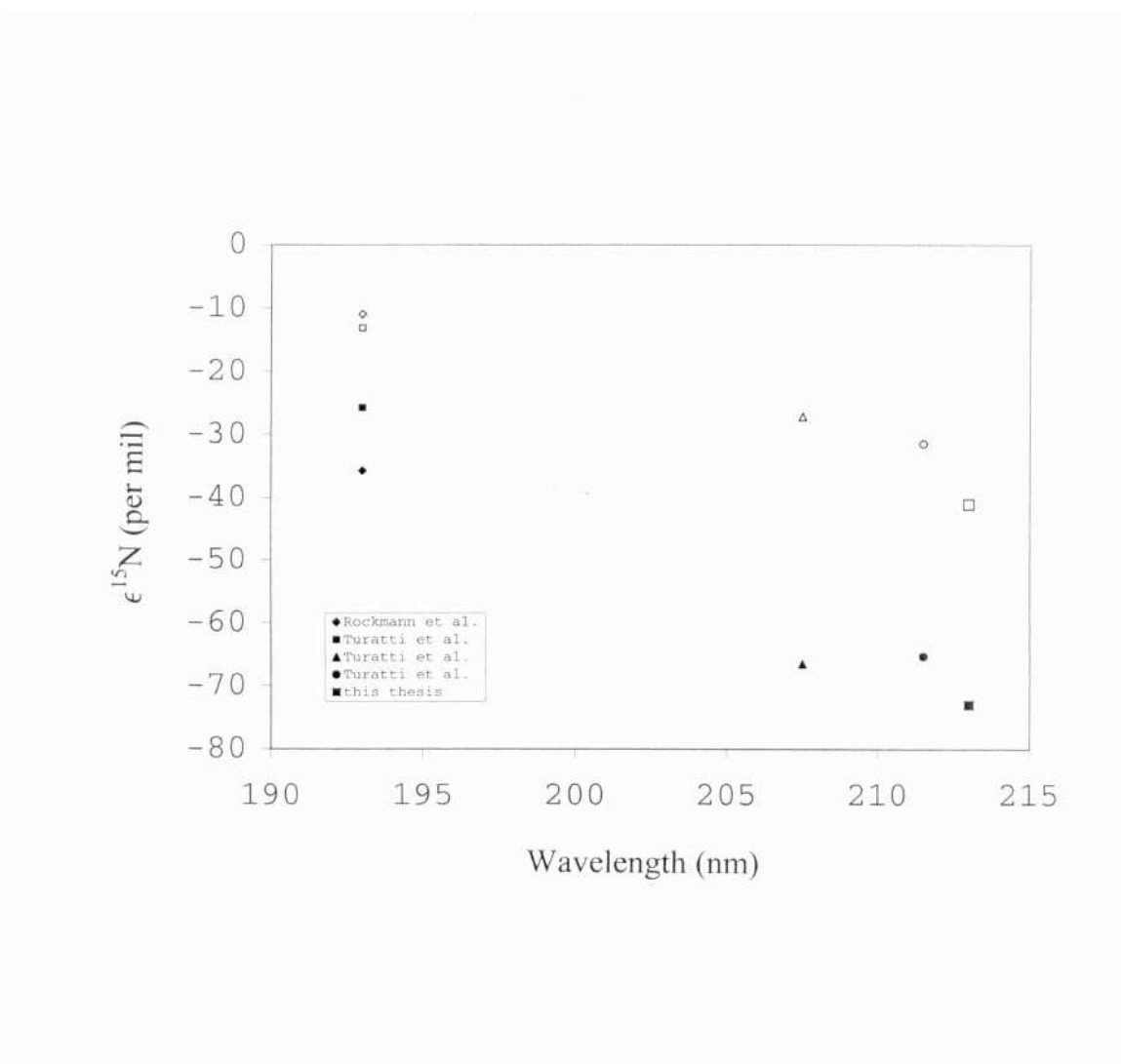


Figure 2.18: The observed fractionation data at different wavelengths. Filled symbols are for  $\epsilon(^{14}\text{N}^{15}\text{N}^{16}\text{O} / ^{14}\text{N}^{14}\text{N}^{16}\text{O})$ , and the corresponding open symbols are for  $\epsilon(^{15}\text{N}^{14}\text{N}^{16}\text{O} / ^{14}\text{N}^{14}\text{N}^{16}\text{O})$ .

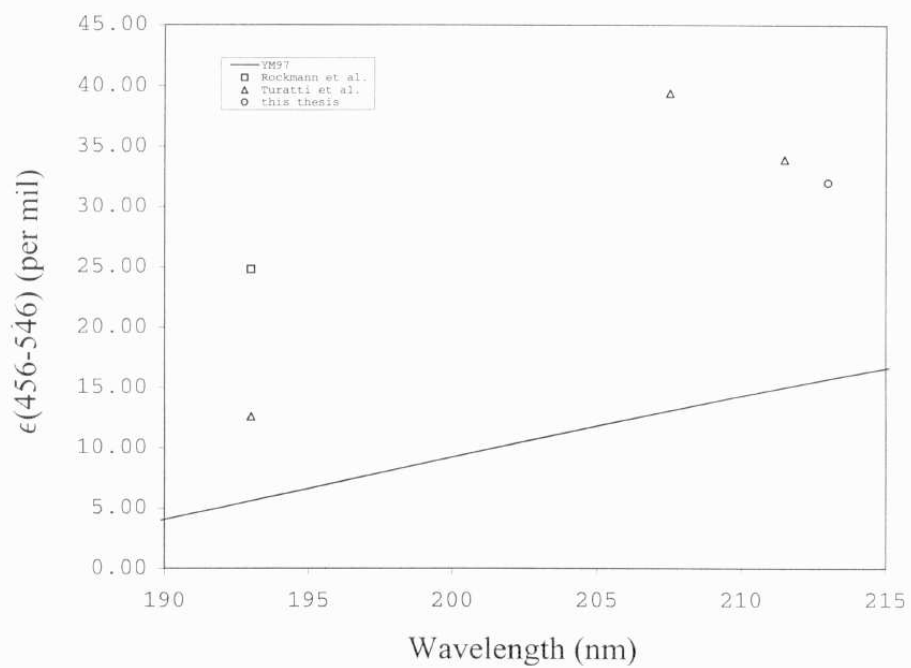


Figure 2.19: The observed and calculated  $\epsilon(^{15}\text{N}^{14}\text{N}^{16}\text{O} / ^{14}\text{N}^{15}\text{N}^{16}\text{O})$  at different wavelengths.

## Bibliography

- [1] Berges, M. G. M., and P. J. Crutzen, “Estimates of global N<sub>2</sub>O emissions from cattle, pig and chicken manure, including a discussion of CH<sub>4</sub> emissions”, *J. Atmos. Chem.*, 24 (1996) 241-269.
- [2] Brenninkmeijer, C. A. M., and T. Rockmann, “Mass spectrometry of the intramolecular nitrogen isotope distribution of environmental nitrous oxide using fragmentation analysis”, *Rap. Comm. Mass. Spec.*, 13 (1999) 2028-2033.
- [3] Cliff, S. S., and M. H. Thiemens, “The <sup>18</sup>O/<sup>16</sup>O and <sup>17</sup>O/<sup>16</sup>O ratios in atmospheric nitrous oxide: A mass-independent anomaly”, *Science*, 278 (1997) 1774-1776.
- [4] Cliff, S. S., C. A. M. Brenninkmeijer, and M. H. Thiemens, “First measurements of the <sup>18</sup>O/<sup>16</sup>O and <sup>17</sup>O/<sup>16</sup>O ratios in stratospheric nitrous oxide: A mass-independent anomaly”, *J. Geophys. Res.*, 104 (1999) 16171-16175.
- [5] Craig, H., “Isotopic standards for carbon and oxygen and correction factors for mass-spectrometric analysis of carbon dioxide”, *Geochim. Cosmochim. Act.*, 12 (1957) 133-149.
- [6] DeMore, W. B., S. P. Sander, D. M. Golden, R. F. Hampson, M. J. Kurylo, C. J. Howard, A. R. Ravishankara, C. E. Kolb, and M. J. Molina, *Chemical kinetics and photochemical data for use in stratospheric modeling, JPL Publication 94-26*, NASA/JPL, Pasadena, California, 1996.
- [7] DeMore, W. B., S. P. Sander, D. M. Golden, R. F. Hampson, M. J. Kurylo, C. J. Howard, A. R. Ravishankara, C. E. Kolb, and M. J. Molina, *Chemical kinetics and photochemical data for use in stratospheric modeling, JPL Publication 97-4*, NASA/JPL, Pasadena, California, 1997.
- [8] Elkins, J. W., J. H. Butler, T. M. Thompson, S. A. Montzka, R. C. Myers, J. M. Lobert, S. A. Yvon, P. R. Wamsley, F. L. Moore, J. M. Gilligan, D. F. Hurst, A. D. Clarke, T. H. Swanson, C. M. Volk, L. T. Lock, L. S. Geller, G. S. Dutton, R. M. Dunn, M. F.

- Dicorleto, T. J. Baring, and A. H. Hayden, "5. Nitrous oxide and halocompounds", *Climate monitoring and diagnostics laboratory - No. 23, Summary report 1994-1995*, U.S. Department of Commerce, NOAA/ERL, Boulder, Colorado, 1996.
- [9] Eriksson, E., "Deuterium and oxygen-18 in precipitation and other natural waters: Some theoretical considerations", *Tellus*, XXVI (1965) 498-512.
- [10] Fritz, P., and J. Ch. Fontes (Eds.), *Handbook of environmental isotope geochemistry, volume 1, the terrestrial environment, A*, 545 pp., Elsevier, New York, 1980.
- [11] Froidevaux, L., and Y. L. Yung, "Radiation and chemistry in the stratosphere: Sensitivity to O<sub>2</sub> absorption cross sections in the Hertzberg continuum", *Geophys. Res. Lett.*, 9 (1982) 854-857.
- [12] Griffith, D. W. T., G. C. Toon, B. Sen, J.-F. Blavier, and R. A. Toth, "Vertical profiles of nitrous oxide isotopomer fractionation measured in the stratosphere", *Geophys. Res. Lett.*, 27 (2000), 2485-2488.
- [13] Hartmann, D. L., L. E. Heidt, M. Loewenstein, J. R. Podolske, J. Vedder, W. L. Starr and S. E. Strahan, "Transport into the south polar vortex in early spring", *J. Geophys. Res.*, 94 (1989) 16779-16795.
- [14] Houghton, J. T., L. G. Meira Filho, J. Bruce, H. Lee, B. A. Callander, E. Haites, N. Harris and K. Maskell (Eds.), *Intergovernmental panel on climate change, climate change 1994: radiative forcing of climate change and an evaluation of the IPCC IS92 emission scenarios*, Cambridge University Press, New York, 1995.
- [15] Johnston, J. C., S. Cliff, and M. Thiemens, "Measurement of multioxygen isotopic ( $\delta^{18}\text{O}$  and  $\delta^{17}\text{O}$ ) fractionation factors in the stratospheric sink reactions of nitrous oxide", *J. Geophys. Res.*, 100 (1995) 16801-16804.
- [16] Kim, K.-R., and H. Craig, "Two isotope characterization of N<sub>2</sub>O in the Pacific Ocean and constraints on its origin in deep water", *Nature*, 347 (1990) 58-61.
- [17] Kim, K.-R., and H. Craig, "Nitrogen-15 and oxygen-18 characteristics of nitrous oxide: A global perspective", *Science*, 262 (1993) 1855-1857.

- [18] Maric, D., and J. P. Burrows, "Formation of N<sub>2</sub>O in the photolysis/photoexcitation of NO, NO<sub>2</sub> and air", *J. Photochem. Photobiol. A*, 66 (1992) 291-312.
- [19] McElroy, M. B., and D. B. A. Jones, "Evidence for an additional source of atmospheric N<sub>2</sub>O", *Glob. Biogeochem. Cycles*, 10 (1996) 651-659.
- [20] Merienne, M. F., B. Coquart, and A. Jenouvrier, "Temperature effect on the ultraviolet absorption of CFCl<sub>3</sub>, CF<sub>2</sub>Cl<sub>2</sub> and N<sub>2</sub>O", *Planet. Space Sci.*, 38 (1990) 617-625.
- [21] Miller, C. E., and Y. L. Yung "Photo-induced isotopic fractionation of stratospheric N<sub>2</sub>O", *Chemosphere: Global Change Science, Atmospheric Nitrous Oxide Special Issue*, in press, 2001.
- [22] Minschwaner, K., R. J. Salawitch, and M. B. McElroy, "Absorption of solar radiation by O<sub>2</sub>: Implications for O<sub>3</sub> and lifetimes of N<sub>2</sub>O, CFCl<sub>3</sub>, and CF<sub>2</sub>Cl<sub>2</sub>", *J. Geophys. Res.*, 98 (1993) 10543-10561.
- [23] Minschwaner, K., R. W. Carver, B. P. Briegleb, and A. E. Roche, "Infrared radiative forcing and atmospheric lifetimes of trace species based on observations from UARS", *J. Geophys. Res.*, 103 (1998) 23243-23253.
- [24] Moore, H., "Isotope measurement of atmospheric nitrogen compounds", *Tellus*, XXVI (1974) 169-174.
- [25] Mosier, A., and C. Kroeze, "A new approach to estimate emissions of nitrous oxide from agriculture and its implications to the global N<sub>2</sub>O budget", *IGBP Global Change Newsletter*, 34, 8-13 June 1998.
- [26] Naqvi, S. W. A., T. Yoshinari, D. A. Jayakumar, M. A. Altabet, P. V. Narvekar, A. H. Devol, J. A. Brandes, and L. A. Codispoti, "Budgetary and biogeochemical implications of N<sub>2</sub>O isotope signatures in the Arabian Sea", *Nature*, 394 (1998) 462-464.
- [27] Nevison, C. D., and E. A. Holland, "A re-examination of the impact of anthropogenically fixed nitrogen on atmospheric N<sub>2</sub>O and the stratospheric O<sub>3</sub> layer", *J. Geophys. Res.*, 102 (1997) 25519-25536.

- [28] Neyer, D. W., A. J. R. Heck, and D. W. Chandler, “Photodissociation of  $\text{N}_2\text{O}$ : J-dependent anisotropy revealed in  $\text{N}_2$  photofragment images”, *J. Chem. Phys.*, 110 (1999) 3411-3417.
- [29] Pearman, G. I., D. Etheridge, F. Desilva, and P. J. Fraser, “Evidence of changing concentrations of atmospheric  $\text{CO}_2$ ,  $\text{N}_2\text{O}$  and  $\text{CH}_4$  from air bubbles in Antarctic ice”, *Nature*, 320 (1986) 248-250.
- [30] Prasad, S. S., “Natural atmospheric sources and sinks of nitrous oxide. 1. An evaluation based on 10 laboratory experiments”, *J. Geophys. Res.*, 99 (1994) 5285-5294.
- [31] Prasad, S. S., “Potential atmospheric sources and sinks of nitrous oxide. 2. Possibilities from excited  $\text{O}_2$ , “embryonic”  $\text{O}_3$ , and optically pumped excited  $\text{O}_3$ ”, *J. Geophys. Res.*, 102 (1997) 21527-21536.
- [32] Prasad, S. S., E. C. Zipf, and X. P. Zhao, “Potential atmospheric sources and sinks of nitrous oxide 3: Consistency with the observed distributions of the mixing ratios”, *J. Geophys. Res.*, 102 (1997) 21537-21541.
- [33] Rahn, T., and M. Wahlen, “Stable isotope enrichment in stratospheric nitrous oxide”, *Science*, 278 (1997) 1776-1778.
- [34] Rahn, T., H. Zhang, M. Wahlen, and G. A. Blake, “Stable isotope fractionation during ultraviolet photolysis of  $\text{N}_2\text{O}$ ”, *Geophys. Res. Lett.*, 25 (1998) 4489-4492.
- [35] Rockmann, T., and C. A. M. Brenninkmeijer, “The error in conventionally reported  $^{13}\text{C}/^{12}\text{C}$  ratios of atmospheric CO due to the presence of mass independent oxygen isotope enrichment”, *Geophys. Res. Lett.*, 25 (1998) 3163-3166.
- [36] Rockmann, T., C. A. M. Brenninkmeijer, M. Wollenhaupt, J. N. Crowley and P. J. Crutzen, “Measurement of the isotopic fractionation of  $^{15}\text{N}^{14}\text{N}^{16}\text{O}$ ,  $^{14}\text{N}^{15}\text{N}^{16}\text{O}$  and  $^{14}\text{N}^{14}\text{N}^{18}\text{O}$  in the UV photolysis of nitrous oxide”, *Geophys. Res. Lett.*, 27 (2000) 1399-1402.
- [37] Selwyn, G., J. Podolske, and H. S. Johnston, “Nitrous oxide ultraviolet absorption spectrum at stratospheric temperatures”, *Geophys. Res. Lett.*, 4 (1977) 427-430.

- [38] Selwyn, G., and H. S. Johnston, “Ultraviolet absorption spectrum of nitrous oxide as function of temperature and isotopic substitution”, *J. Chem. Phys.*, 74 (1981) 3791-3803.
- [39] Thiemens, M. H., “Mass-independent isotope effects in planetary atmospheres and the early solar system”, *Science*, 283 (1999) 341-345.
- [40] Toyoda, S., and N. Yoshida, “Determination of nitrogen isotopomers of nitrous oxide on a modified isotope ratio mass spectrometer”, *Anal. Chem.*, 71 (1999) 4711-4718.
- [41] Turatti, F., D. W. T. Griffith, S. R. Wilson, M. B. Esler, T. Rahn, H. Zhang, and G. A. Blake, “Positionally dependent  $^{15}\text{N}$  fractionation factors in the UV photolysis of  $\text{N}_2\text{O}$  determined by high resolution FTIR spectroscopy”, *Geophys. Res. Lett.*, 27 (2000), 2489-2492.
- [42] Wahlen, M., and T. Yoshinari, “Oxygen isotope ratios in  $\text{N}_2\text{O}$  from different environments”, *Nature*, 313 (1985) 780-782.
- [43] World Meteorological Organization, *Scientific assessment of ozone depletion: 1994, global ozone research and monitoring project-report 37*, Geneva, Switzerland, 1995.
- [44] World Meteorological Organization, *Scientific assessment of ozone depletion: 1998, global ozone research and monitoring project-report 44*, Geneva, Switzerland, 1999.
- [45] Yoshida, N., and S. Matsuo, “Nitrogen isotope ratio of atmospheric  $\text{N}_2\text{O}$  as a key to the global cycle of  $\text{N}_2\text{O}$ ”, *Geochemical . J.*, 17 (1983) 231-239.
- [46] Yoshida, N., “N-15-depleted  $\text{N}_2\text{O}$  as a product of nitrification”, *Nature*, 335 (1988) 528-529.
- [47] Yoshida, N., and S. Toyoda, “Constraining the atmospheric  $\text{N}_2\text{O}$  budget from intramolecular site preference in  $\text{N}_2\text{O}$  isotopomers”, *Nature*, 405 (2000) 330-334.
- [48] Yoshinari, T., and M. Wahlen, “Oxygen isotope ratios in  $\text{N}_2\text{O}$  from nitrification at a wastewater treatment facility”, *Nature*, 317 (1985) 349-350.
- [49] Yoshinari, T., M. A. Altabet, S. W. A. Naqvi, L. Codispoti, A. Jayakumar, M. Kuhland, and A. Devol, “Nitrogen and oxygen isotopic composition of  $\text{N}_2\text{O}$  from suboxic waters

of the eastern tropical north pacific and the arabian sea - measurement by continuous-flow isotope-ratio monitoring”, *Marine Chem.*, 56 (1997) 253-264.

- [50] Yoshino, K., D. E. Freeman, and W. H. Parkinson, “High resolution absorption cross section measurements of  $N_2O$  at 225-299 K in the wavelength region 170-222 nm”, *Planetary Space Science*, 32 (1984) 1219-1222.
- [51] Yung, Y. L., and C. E. Miller, “Isotopic fractionation of stratospheric nitrous oxide”, *Science*, 278 (1997) 1778-1780.
- [52] Zhang, H., P. O. Wennberg, V. H. Wu, and G. A. Blake, “Fractionation of  $^{14}N^{15}N^{16}O$  and  $^{15}N^{14}N^{16}O$  During Photolysis at 213 nm”, *Geophys. Res. Lett.*, 27 (2000), 2481-2484.
- [53] Zipf, E. C., and S. S. Prasad, “Experimental evidence that excited ozone is a source of nitrous oxide”, *Geophys. Res. Lett.*, 25 (1998) 4333-4336.

## Chapter 3 Photodissociation of $\text{HNO}_4$ in the near IR

### 3.1 Introduction

The distribution of ozone,  $O_3$ , in the stratosphere reflects a balance between its local production and loss modified by atmospheric transport. Ozone production is dominated by the photodissociation of molecular oxygen. It has been established that the removal of ozone is through catalytic cycles involving a suite of free radical families such as odd hydrogen  $HO_x$  ( $= H + OH + HO_2$ ) and odd nitrogen  $NO_x$  ( $= NO + NO_2$ ). Though they exist as trace constituents (typically less than 1 ppbv) in the atmosphere, these species strongly influence stratospheric ozone chemistry. Illustrated in Figure 3.1 is the photochemical loss rates for  $O_3$  due to each of these chemical families, and to the halogens, inferred from *in situ* measurements of radical concentrations on May 1, 1993 (48). Under these conditions, the largest ozone loss is due to  $HO_x$  ( $> 40\%$ );  $NO_x$  contributes a smaller but significant fraction (20%). Halogens are known to become most important in ozone loss processes in the perturbed polar regions in the early spring (see, e.g., (43)).

The ozone-destroying radicals can be temporarily removed from the atmosphere after being sequestered into non-radical, reservoir compounds. The existence of these reservoir species is central to ozone chemistry. A reactive free radical, sequestered as a relatively unreactive reservoir species, does not contribute to  $O_3$  loss. Because the concentration of reservoir species is often much larger than the concentration of their parent free radicals, small changes in the abundance of reservoir species can have a profound impact on the catalytic destruction rate of ozone. This chapter is focused on one such compound, peroxyntic acid ( $HNO_4$ , also called PNA), an important species coupling the  $HO_x$  and  $NO_x$  families in the upper troposphere and stratosphere. Presented is the study of the photodissociation of peroxyntic acid in the red/near infrared (NIR) spectral region.

In this study, the cleavage of the  $HOO-NO_2$  bond in  $HNO_4$  (Figure 3.2) via absorption of NIR solar radiation is investigated. It is shown that this process is important and this study improves our understanding of what controls the  $HO_x$  concentration in both the lower stratosphere and upper troposphere. Such knowledge is at the core of understanding the chemistry of the Earth's atmosphere.

$HNO_4$  was first observed in the gas phase when Niki and his co-workers examined the product of the reaction of  $HO_2$  and  $NO_2$ , "one of the potentially important reactions" in the photochemical formation of ozone in the troposphere (29). FTIR solar occultation

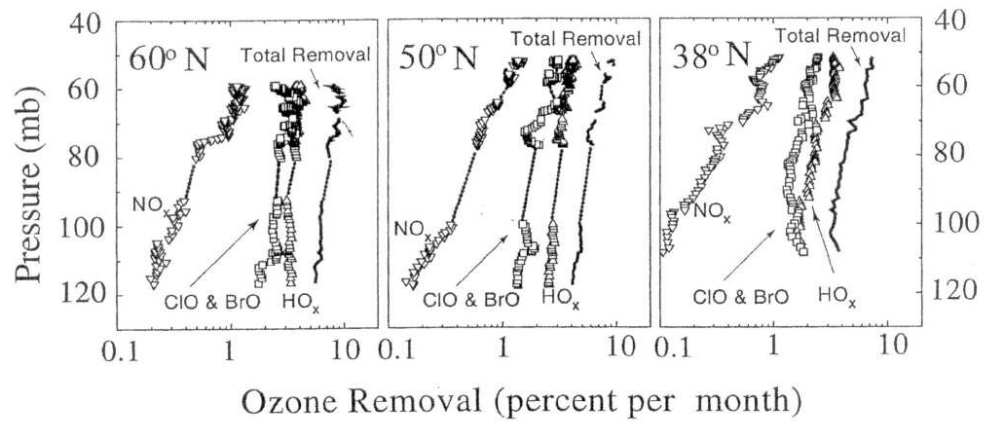


Figure 3.1: Photochemical loss rates of ozone for the major chemical cycles in the lower stratosphere from ER-2 measurements in May 1993. Adapted from (48).

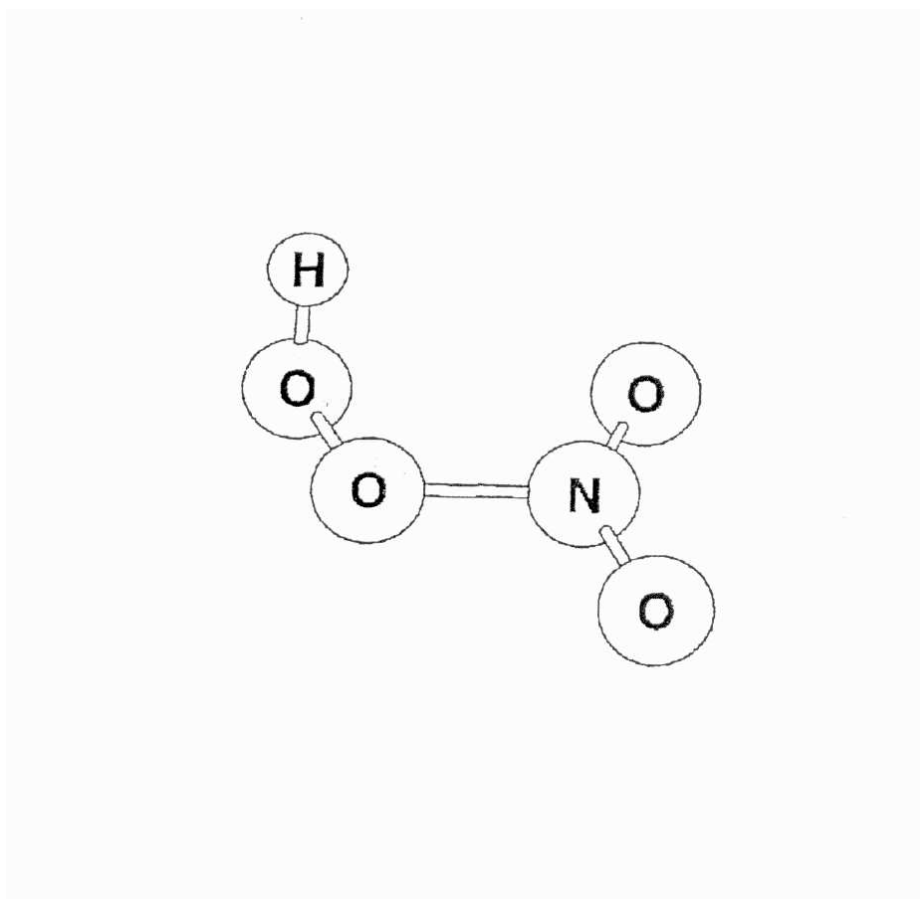


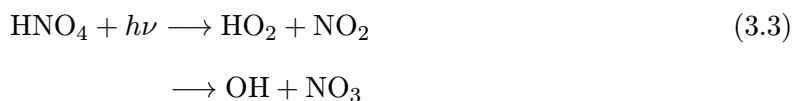
Figure 3.2: A depiction of the optimized HNO<sub>4</sub> structure. The heavy atom frame is nearly planar, with the H atom oriented perpendicular to the plane. From (25).

spectra obtained using space shuttle-borne and balloon-borne spectrometers have revealed spectral features near  $803\text{ cm}^{-1}$  that are attributed to stratospheric  $\text{HNO}_4$  (15; 35). Using spectroscopic parameters measured in the laboratory (23), the atmospheric mixing ratio of  $\text{HNO}_4$  is estimated to be on the order of 200 ppt at 27 km for sunset at  $35^\circ\text{N}$  (39).

$\text{HNO}_4$  is included in most atmospheric chemical transport models. It is the current understanding that  $\text{HNO}_4$  is formed in the atmosphere exclusively by the three-body recombination of the hydroperoxyl radical and nitrogen dioxide:



and is removed by reaction with hydroxyl radicals and via photodissociation:



and by thermal decomposition:



Reaction (3.4) is negligible to the daytime chemistry of  $\text{HNO}_4$  above 7 km because of the low temperature and pressure (16), but it still contributes significantly to the nighttime loss of  $\text{HNO}_4$ . Assuming (3.2) yields  $\text{H}_2\text{O}$ ,  $\text{O}_2$ , and  $\text{NO}_2$ , the net result of (3.1) and (3.2) is to remove odd hydrogen radicals  $\text{HO}_x$ :



On the other hand, the photodissociation of  $\text{HNO}_4$  (3.3) produces a null cycle for  $\text{HO}_x$ . The importance of  $\text{HNO}_4$  as a  $\text{HO}_x$  sink or a  $\text{HO}_x$  reservoir is thus controlled by its formation rate (3.1) and the competition between the reaction with OH (3.2) and  $\text{HNO}_4$  photodissociation (3.3).

The photolysis of  $\text{HNO}_4$  has been studied in the UV region to determine both cross sections (6; 17; 26; 27; 40) and branching ratios (22; 37). There have been three direct measurements of the gas phase spectrum at wavelengths relevant to the upper troposphere

( $\lambda > 305$  nm) (17; 26; 40). The measured cross sections determined in these studies differ by approximately a factor of 10 in this region of the spectrum, leading to significantly different calculated photodissociation rates in the upper troposphere and lower stratosphere. The JPL Panel Recommendation (7), which is based on two of the studies (26; 40), does not give advice for  $\lambda > 325$  nm. The large uncertainties in the cross sections at longer wavelengths thus warrant further investigation.

Interest in the potential role of NIR photolysis of  $\text{HNO}_4$  was stimulated by the ongoing attempt to reconcile model-observation discrepancies in the concentrations of stratospheric  $\text{HO}_x$  measured at high solar zenith angles (SZAs). During the 1993 Stratospheric Photochemistry, Aerosols, and Dynamics Expedition (SPADE), the observed concentration of  $\text{HO}_x$  was higher than predicted throughout the day (38). High SZA measurements revealed a significant  $[\text{HO}_x]$  increase in the early morning, consistent with nighttime buildup of a photo-labile hydroxyl-containing species. Since solar UV photons were strongly attenuated at high SZA due to the large ozone optical depth, photochemical processes generating  $\text{HO}_x$  from light at visible and NIR wavelengths were proposed (3; 18; 38). Donaldson *et al.* (9) presented calculations that indicate that excitation of vibrational overtones of the OH stretch in  $\text{HNO}_3$ ,  $\text{HNO}_4$ , and  $\text{H}_2\text{O}_2$  may lead to their dissociation, and that this process could potentially contribute to the production of  $\text{HO}_x$  in the lower stratosphere at high SZAs. Of these species,  $\text{HNO}_4$  is considered most likely to enhance the  $\text{HO}_x$  production because energetically only three quanta of excitation of OH vibrational stretch ( $3\nu_{\text{OH}}$ ) are required to break the O- $\text{NO}_2$  bond in  $\text{HNO}_4$ . For  $\text{HNO}_3$  or  $\text{H}_2\text{O}_2$ , four or five quanta, respectively, are required to deliver energy in excess of the strength of the weakest bond, and therefore the cross sections will be orders of magnitude smaller.

Recent twilight observations of  $[\text{HO}_x]$  obtained during the 1997 Photochemistry of Ozone Loss in the Arctic Region In Summer (POLARIS) campaign also imply the existence of long wavelength photolytic sources of  $\text{HO}_x$  (50). Measurements of  $\text{HO}_2$  for SZAs of 80-94° were found to be much higher than calculated. Based on a radiative transfer calculation, Wennberg *et al.* suggested that the photolysis must occur at a wavelength  $> 650$  nm and therefore the strength of the bonds being broken must be  $< 45$  kcal mole<sup>-1</sup>.  $\text{HNO}_4$  was speculated to be the likely source and a photolysis rate of  $1.2 \times 10^{-5}$  sec<sup>-1</sup>, corresponding to an integrated band strength of  $2\text{-}3 \times 10^{-20}$  cm<sup>2</sup> molecule<sup>-1</sup> nm ( $650 < \lambda < 1250$  nm), is required to reconcile the calculation with the observed values of  $[\text{HO}_2]$  (50). The longward

wavelength limit of 1250 nm is based on the photodissociation threshold value of  $\text{HNO}_4$  reported by Zabel *et al.* (51).

The proposal for the NIR photodissociation of  $\text{HNO}_4$  has gained support from recent interpretations of other stratospheric measurements. Observations obtained by the JPL MkIV balloon-borne interferometer during POLARIS have shown that the inclusion of this process in a stratospheric model leads to agreement between calculated and observed  $[\text{HNO}_4]$ . Using standard chemistry, the concentration of  $\text{HNO}_4$  was predicted to be approximately two times larger than that observed (30).

NIR photodissociation of  $\text{HNO}_4$  may also play an important role in the  $\text{HO}_x$  chemistry of the upper troposphere where most of the UV solar radiation is filtered out by stratospheric  $\text{O}_3$ . In recent years, considerable attention has been given to the potential role of aircraft emissions of  $\text{NO}_x$  on the ozone production rate in the upper troposphere (32). These efforts have revealed the need for much greater scrutiny of  $\text{HNO}_4$  kinetics and photochemistry (5). During October/November 1997, simultaneous observations of  $\text{NO}$ ,  $\text{HO}_2$  and other species were obtained by instruments on the NASA DC-8 aircraft as part of the Subsonic Assessment: Ozone and Nitrogen Oxide Experiment (SONEX) campaign in the upper troposphere (41; 46). These measurements have revealed a significant model-observation discrepancy for  $[\text{HO}_x]$  at high SZAs (5; 12; 19). According to these studies, the inclusion of the  $\text{HO}_x$  source speculated by Wennberg *et al.* (50) would reconcile models and observations for  $[\text{HO}_x]$ .

The only previous laboratory measurement relevant to NIR photodissociation of  $\text{HNO}_4$  was performed by Fono *et al.* (13). They measured the  $3\nu_{\text{OH}}$  band intensities of both  $\text{HNO}_4$  and  $\text{HNO}_3$  in concentrated sulfuric acid solutions, and estimated the gas phase intensity by linearly scaling the  $\text{HNO}_4$  solution spectrum according to the ratio of the gas and solution phase intensity observed for  $\text{HNO}_3$  (13). The authors noted that “because of solvent effects on the overtone intensities, the solution phase results should not be directly compared with gas phase values” (13). The overtone measurement for gas phase  $\text{HNO}_4$  is difficult due to the low vapor pressure ( $\sim 1$  torr at 273 K) and short thermal lifetime of  $\text{HNO}_4$  ( $\sim 12$  sec at 298 K and 760 torr).

This thesis adopts an approach that seeks key information directly relevant to the photodissociation processes of  $\text{HNO}_4$  in the atmosphere. Section 3.2 describes three experiments that are designed to determine the cross sections and quantum yields for gas phase  $\text{HNO}_4$ .  $\text{HNO}_4$  is found to dissociate at wavelengths as long as 1600 nm. It is argued that molecular

internal energy available for thermal excitation in addition to the photon energy can explain the observed dissociation of  $\text{HNO}_4$  beyond its thermodynamic dissociation threshold. Accordingly, a temperature-dependent quantum yield is predicted. The 1<sup>st</sup> OH stretching overtone is found to be partially dissociative. Because it is significantly brighter than the 2<sup>nd</sup> overtone, it contributes significantly to the photodissociation of  $\text{HNO}_4$ . Section 3.3 presents the implications of these experimental results. The strength of the HOO- $\text{NO}_2$  bond is constrained and compared to literature values. The atmospheric significance of the NIR photodissociation of  $\text{HNO}_4$  is then discussed.

## 3.2 Experiments and Results

### 3.2.1 Overview of the Experimental Design

In order to estimate the photodissociation rate of  $\text{HNO}_4$ ,  $J_{\text{HNO}_4}$ , it is necessary to obtain both the cross sections,  $\sigma$ , and quantum yields,  $\Phi$ :

$$J_{\text{HNO}_4} = \int \Phi(\nu)\sigma(\nu)I(\nu)d\nu \quad , \quad (3.6)$$

where  $I(\nu)$  is the actinic flux at frequency  $\nu$ . Experiments have been designed to investigate the photodissociation of  $\text{HNO}_4$  at  $700 \text{ nm} < \lambda < 2000 \text{ nm}$ . Specifically, the integrated cross sections, or  $\int \sigma(\nu) d\nu$ , have been measured for  $\text{HNO}_4$  rovibrational transitions using two-color absorption and FTIR spectroscopy. The quantum yields of these bands were then determined from study of their action spectra.

This part of the thesis is structured as follows:

- Section 3.2.2 describes a two-color direct absorption survey of the 700 - 1000 nm spectral region. The strengths of the  $3\nu_{\text{OH}}$  and  $4\nu_{\text{OH}}$  of  $\text{HNO}_4$  (and those of  $\text{HNO}_3$  and  $\text{H}_2\text{O}_2$ ) are obtained. Spectra at  $\lambda > 1100 \text{ nm}$  are not obtained due to the rapid fall-off in the sensitivity of the silicon array detector.
- In Section 3.2.3, the absorption spectrum of  $\text{HNO}_4$  is extended to longer wavelengths using an FTIR spectrometer. The relative strengths of various  $\text{HNO}_4$  IR bands over the spectral region 1,200 - 10,500  $\text{cm}^{-1}$  (i.e., 952 - 8,333 nm) are determined. These relative cross sections are then placed on an absolute scale by reference to the earlier work presented in Section 3.2.2 and a study previously published by May and Friedl (23).

- Section 3.2.4 presents the method used to determine the dissociation efficiency, the so-called “action spectrum” experiment. In this method, the photodissociation product,  $\text{HO}_2$ , is converted to OH via reaction with NO. The OH product is then monitored by laser-induced fluorescence (LIF). A number of vibrational transitions of  $\text{HNO}_4$  are found to be dissociative using this technique and their quantum yields, relative to  $3\nu_{\text{OH}}$ , are determined.  $3\nu_{\text{OH}}$  is assumed to be fully dissociative because it lies  $\sim 25$  kJ/mole above the dissociation threshold (see Section 3.3.1 for more discussion on energetics of  $\text{HNO}_4$ ).

### 3.2.2 $\text{HNO}_4$ $3\nu_{\text{OH}}$ and $4\nu_{\text{OH}}$ Cross Sections from Absorption Spectroscopy

[The work described in this section was conducted using the facilities of the Kinetics and Atmospheric Chemistry Group at JPL. The content of this section is part of “Intensity of the Second and Third OH Overtones of  $\text{H}_2\text{O}_2$ ,  $\text{HNO}_3$ , and  $\text{HO}_2\text{NO}_2$ ” by Zhang, H., C. M. Roehl, S. P. Sander, and P. O. Wennberg, *J. Geophys. Res.*, 105, 14593-14598, 2000. Copyright by the American Geophysical Union.]

#### Experimental

In this two-color direct absorption experiment, both UV and near-IR absorbances are simultaneously measured in a flow tube. The recommended UV cross sections of  $\text{H}_2\text{O}_2$ ,  $\text{HNO}_3$ , and  $\text{HNO}_4$  (7) are used to quantify the concentrations of these species so that the measured near-IR optical depths can then be directly converted to absolute cross sections.

**1. Instrumentation** The optical/vacuum apparatus used in this study has been described previously (47). The configuration used here is shown in Figure 3.3. The system is composed of two lamp sources, an absorption cell/vacuum system, and UV and near-IR detectors.

Collimated light from a 250 W Quartz-tungsten-halogen lamp (Oriel, part 6334) and a deuterium lamp (Hamamatsu, model L1314X) are combined at dichroic mirror 1 (Oriel, part 66217), which reflects  $260 < \lambda < 320$  nm and transmits  $\lambda > 350$  nm. The beam is then folded by two  $45^\circ$  reflectors into a multipass absorption cell through a 4 mm aperture. Both the  $45^\circ$  reflectors and the White cell mirrors are  $\text{MgF}_2$ -coated aluminum.

The Pyrex absorption cell is 90 cm long and has an inner diameter of 30 mm. Light passes through it eight times. The cell has an outer cooling jacket where chilled methanol is circulated to maintain thermal control. The temperature is monitored with a thermocouple probe located 7 cm from the cell end. The pressure in the cell is monitored with a thermocouple pressure gauge and a capacitance manometer (MKS Instruments). The absorption cell can be evacuated to less than 10 mtorr by a mechanical pump with an in line liquid nitrogen trap. Two 1-inch quartz windows are fused onto two quartz tubes, which are sealed to the two ends of the absorption cell with O-ring joints. When the cell is cooled, the windows are purged from the outside with dry nitrogen gas to prevent condensation. Light exits the absorption cell, and the UV and the visible/near-IR probe beams are then

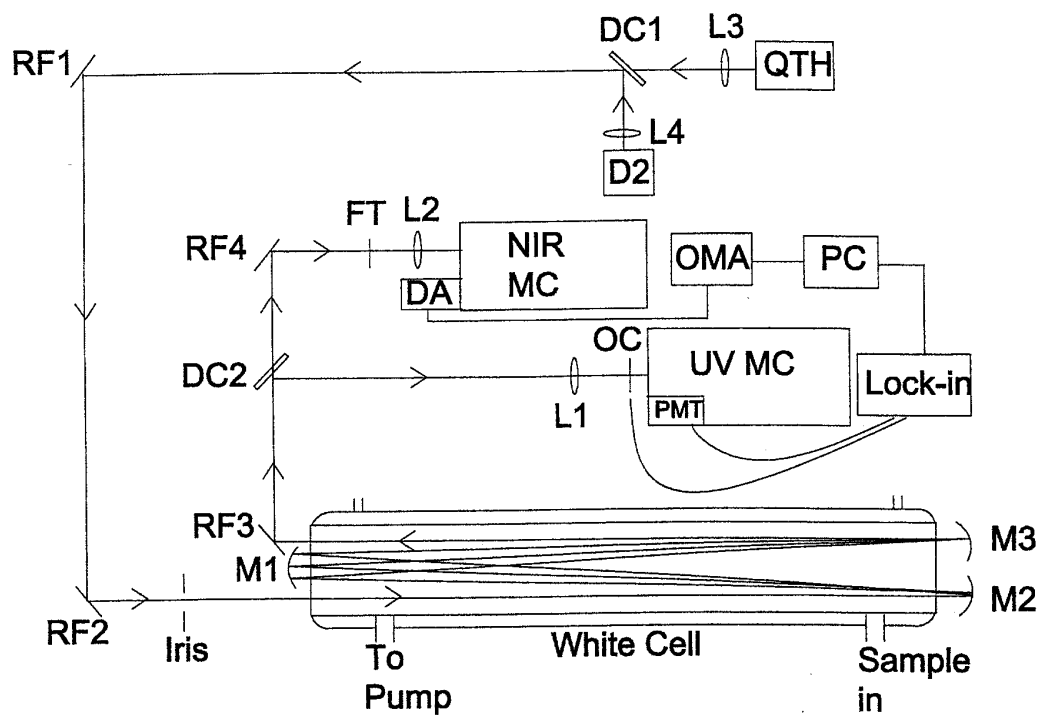


Figure 3.3: Schematic diagram of the two-color absorption experiment setup. D2, deuterium lamp; DA, diode array detector; DC1, DC2, dichroic mirrors; FT, long-pass filter; L1, L2, focusing lenses; L3, L4, collimating lenses; M1, M2, M3, White Cell mirrors; NIR MC, near-IR monochromator; OC, optical chopper; OMA, optical multichannel analyzer; PMT, photon multiplier tube; QTH, quartz tungsten halogen lamp; RF1, RF2, RF3, RF4, reflectors; UV MC, UV monochromator.

separated at a second dichroic mirror that has the same spectral characteristics as dichroic mirror 1.

The UV light is focused into a 0.5 m UV monochromator (216.5 GCA/McPherson) equipped with a 2400 grooves/mm grating blazed at 240 nm. The light is detected by a multialkali photocathode photomultiplier tube (Hamamatsu R955) operated at  $\sim 750$  V. Just before entering the monochromator, the UV beam is modulated at 2 kHz with an optical chopper (New Focus). The PMT current is processed by a lock-in amplifier (Stanford Research Systems). The widths of both the entrance and the exit slits on the monochromator are set at 500  $\mu\text{m}$ . Scattered light is negligible for the UV system at the wavelength region used in this experiment. The monochromator wavelength scale is calibrated with a Hg lamp. This lamp is also used to confirm the spectral resolution of 0.3 nm.

The visible/NIR light is dispersed with a 0.32 m monochromator (ISA, HR320) equipped with a 1024-element silicon photodiode array detector (EG & G, model 1412). A long-pass filter (Corion, LL700) is placed in the collimated beam to minimize the interference from the higher-order modes. The 300 grooves/mm grating (blazed at 1.0  $\mu\text{m}$ ) combined with the entrance slit of 50  $\mu\text{m}$  produces a spectral resolution of 0.5 nm (full width at half maximum (FWHM)). This performance is confirmed by recording the spectrum of a low-pressure Argon pen ray lamp.

The visible/near-IR absorption spectra were recorded in segments of about 250 nm, while the UV absorbance is monitored at a single wavelength. For comparison, measurements were made at both 250 nm and 260 nm. The smallest near-IR absorbance detectable is  $2 \times 10^{-4}$ . Besides noise in the electronics and lamp drift, interference from water adsorbed to the cell windows limits the smallest UV detection to absorbance of  $\sim 1 \times 10^{-2}$ . In addition, scattered light in the White cell causes curvature in the Beer's law plot at optical depths as low as 3, and so all the data reported here were taken at lower optical depths.

**2. HNO<sub>4</sub> Synthesis** HNO<sub>4</sub> was prepared in a nitrogen-purged glove box according to the method described by Kenley *et al.* [1981] (20). Briefly,  $\sim 1$  g BF<sub>4</sub>NO<sub>2</sub> (Aldrich, 95+%) was slowly added into  $\sim 5$  mL of 95+ wt% H<sub>2</sub>O<sub>2</sub> in  $\sim 50$  mg increments. The highly concentrated H<sub>2</sub>O<sub>2</sub> was obtained by vacuum distillation of 70 wt% H<sub>2</sub>O<sub>2</sub> (FMC). The mixture was vigorously stirred in a jacketed glass vessel with water, cooled to  $\sim 273$  K, circulating around it. Once the synthesis was finished, the mixture was quickly transferred

to a glass bubbler, and then the bubbler was immediately immersed into an ice/water bath.

Impurities were always found in the prepared  $\text{HNO}_4$ . Among them,  $\text{HNO}_3$ ,  $\text{H}_2\text{O}_2$ , and  $\text{NO}_2$  are problematic because they absorb at the UV wavelengths used to quantify  $[\text{HNO}_4]$ . The strengths of  $3\nu_{\text{OH}}$  for  $\text{H}_2\text{O}_2$  (95+ wt%) and  $\text{HNO}_3$  (Fisher, minimum 69.0%, maximum 71.0%, used without further purification) were determined in separate experiments using their known cross sections (7) at 250 nm and 260 nm. The spectrum of  $\text{NO}_2$  over the visible/near-IR region was also measured. Throughout the experiment, the concentrations of these impurities were monitored using their distinct visible and near-IR absorption features in order to estimate their contributions to the observed UV absorption. The typical impurities levels are  $[\text{H}_2\text{O}_2] \sim (6-7) \times 10^{15} \text{ cm}^{-3}$ ,  $[\text{HNO}_3] < 4 \times 10^{14} \text{ cm}^{-3}$ , and  $[\text{NO}_2] \sim (1-1.5) \times 10^{14} \text{ cm}^{-3}$  for typical  $[\text{HNO}_4]$  concentrations of  $(2.5-10) \times 10^{15} \text{ cm}^{-3}$ .

**3. Spectrum Acquisition and Analysis** All data were obtained by flowing argon (UHP/Zero Grade, Air Products) through a bubbler to carry the sample into the absorption cell. The glass sample bubbler was connected as closely as possible to the inlet of the absorption cell with only glass in between to avoid decomposition of the samples.  $\text{HNO}_4$  data were obtained with both the bubbler and the absorption cell kept at  $273 \pm 1 \text{ K}$  and the carrier gas pre-cooled by passing it through a copper coil immersed in an ice-water mixture. Data for  $\text{HNO}_3$  and  $\text{H}_2\text{O}_2$  were obtained near room temperature ( $297 \pm 2 \text{ K}$ ). In addition, data for  $\text{H}_2\text{O}_2$  at  $\sim 273 \text{ K}$  were obtained to study the temperature dependence of its near-IR cross section.

Two flow configurations were used. For  $\text{HNO}_3$  and  $\text{H}_2\text{O}_2$ , the argon flow over the sample was combined with a larger flow of pure argon as a means of varying the concentration of the analyte. The concentration of  $\text{HNO}_4$  in the sample gradually decreased during the experiment, hence it was not necessary to vary the concentration by dilution. A solenoid control valve was employed to maintain a constant pressure ( $\sim 35 \text{ torr}$ ) inside the cell between the background and the sample spectra.

The absorption spectrum of  $\text{HNO}_4$  was recorded in the 700-1000 nm region and smoothed subsequently to a resolution of  $\sim 1 \text{ nm}$ . We found that for some  $\text{HNO}_4$  samples the amount of  $\text{HNO}_3$  and  $\text{NO}_2$  was negligible. For others, however,  $\text{HNO}_3$  and  $\text{NO}_2$  were elevated initially, but after bubbling argon through the sample for 5-10 min, the concentration of  $\text{HNO}_3$  and  $\text{NO}_2$  was reduced significantly. This is illustrated in Figure 3.4 by two typical

raw spectra taken from the same  $\text{HNO}_4$  sample. Identified on the spectra are  $3\nu_{\text{OH}}$  for  $\text{HNO}_4$ ,  $\text{HNO}_3$ , and  $\text{H}_2\text{O}_2$ , as well as  $\text{H}_2\text{O}$ . The grating was moved from time to time to the stronger  $\text{NO}_2$  visible band (21) to monitor its concentration. For the  $\text{HNO}_4$  data reported here,  $\text{HNO}_3$  and  $\text{NO}_2$  impurities contribute less than 0.2% of the total UV optical depth and thus are not considered further in the spectral analysis.

$\text{H}_2\text{O}_2$  was present as a significant impurity in all our  $\text{HNO}_4$  samples. In the analysis it is assumed that no species other than  $\text{HNO}_4$  and  $\text{H}_2\text{O}_2$  contribute to the UV absorbance:

$$A_{\text{UV}, \text{H}_2\text{O}_2} + A_{\text{UV}, \text{HNO}_4} = A_{\text{total UV}} \quad (3.7)$$

The contribution of  $\text{H}_2\text{O}_2$  is subtracted from the UV absorbance using the ratio of the UV to overtone intensities determined in this study:

$$A_{\text{UV}, \text{H}_2\text{O}_2} = (\sigma_{\text{UV}, \text{H}_2\text{O}_2} / \sigma_{\text{NIR}, \text{H}_2\text{O}_2}) \times A_{\text{NIR}, \text{H}_2\text{O}_2} \quad (3.8)$$

The absolute intensity of the  $\text{HNO}_4$  overtone is then calculated from the measured near-IR absorbance and its known UV cross section (7):

$$\sigma_{\text{NIR}, \text{HNO}_4} = (A_{\text{NIR}, \text{HNO}_4} / A_{\text{UV}, \text{HNO}_4}) \times \sigma_{\text{UV}, \text{HNO}_4} \quad (3.9)$$

For the data reported here, only those measurements where  $\text{HNO}_4$  contributes more than 60% of the UV optical depth are used. The baseline fluctuation seen in Figure 3.4 is due to unknown origin. Corrections have been made to the baseline as part of the spectral processing.

## Results

Shown in Figure 3.5 is the plot of the integrated optical depth of  $3\nu_{\text{OH}}$  as a function of column density for  $\text{H}_2\text{O}_2$ ,  $\text{HNO}_3$ , and  $\text{HNO}_4$ . The slope of the least squares fit gives the integrated cross section. The data for  $\text{H}_2\text{O}_2$  includes samples at both room temperature and 273 K; within the precision of these measurements there is no temperature dependence of the IR cross section. The spectra of the  $3\nu_{\text{OH}}$  band for  $\text{HNO}_3$ ,  $\text{H}_2\text{O}_2$ , and  $\text{HNO}_4$  are shown in Figure 3.6. Essentially the OH stretch is of similar strength in these three molecules. The  $4\nu_{\text{OH}}$  features from  $\text{H}_2\text{O}_2$ ,  $\text{HNO}_3$ , and  $\text{HNO}_4$  are also observed. Table 3.1 summarizes the observed peak positions, the band strengths, and the oscillator strengths for these overtones.

The uncertainty in the reported cross section has two components: our experimental

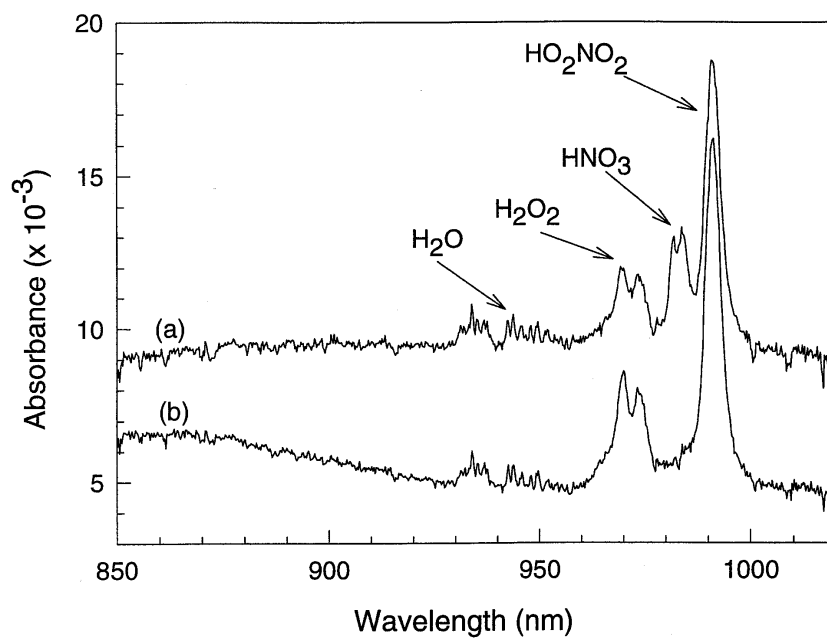


Figure 3.4: Raw spectra of  $\text{HNO}_4$ . (curve a) Initial spectrum; (curve b) after about 5 min of flow, when the  $\text{HNO}_3$  impurity has been significantly reduced. The negative-going spikes may be due to the nonlinearity of the detector.

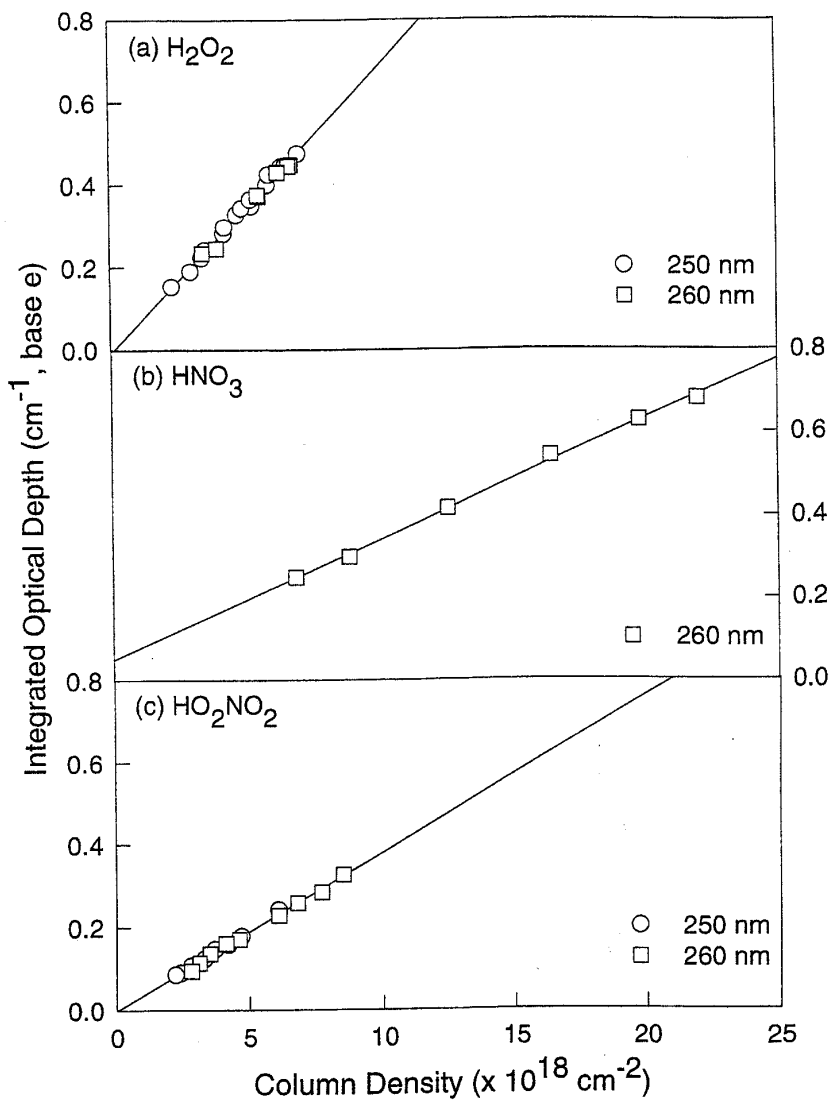


Figure 3.5: Plot of the band strength for  $3\nu_{\text{OH}}$  as a function of column density derived from the absorbance measurements at 250 nm and/or 260 nm. (a) H<sub>2</sub>O<sub>2</sub>, including samples taken at both room temperature and  $\sim 273$  K; (b) HNO<sub>3</sub>; and (c) HNO<sub>4</sub>, after accounting for H<sub>2</sub>O<sub>2</sub>.

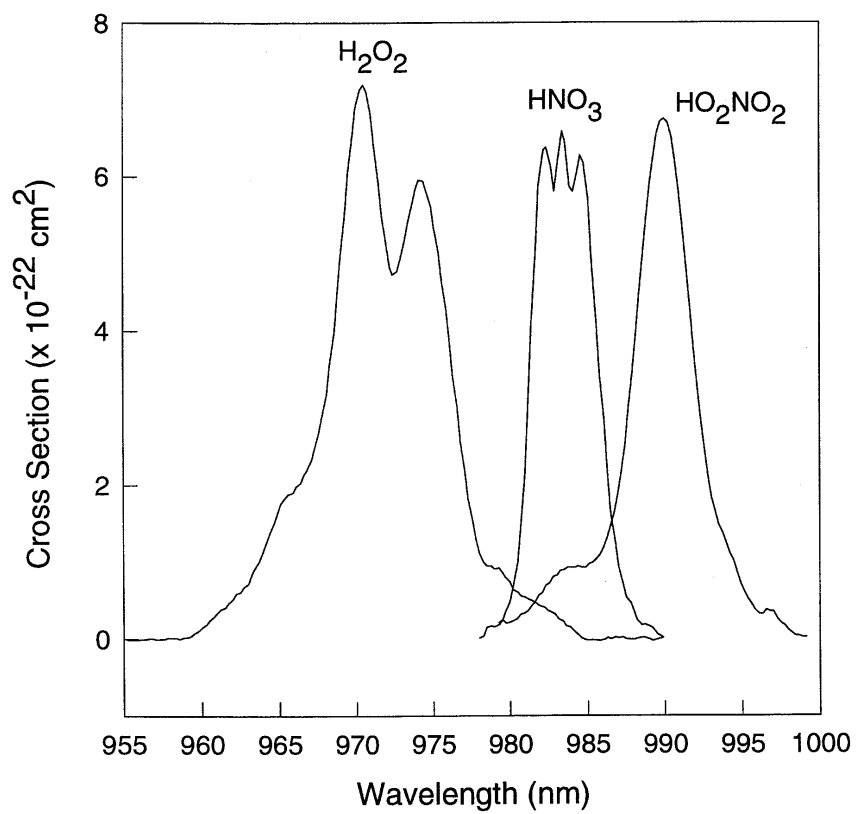


Figure 3.6: Spectrum of  $3\nu_{\text{OH}}$  for  $\text{H}_2\text{O}_2$ ,  $\text{HNO}_3$ , and  $\text{HNO}_4$  at a resolution of  $\sim 1$  nm, taken at room temperature for  $\text{H}_2\text{O}_2$  and  $\text{HNO}_3$  and at  $\sim 273$  K for  $\text{HNO}_4$ .

Table 3.1: OH Overtones in H<sub>2</sub>O<sub>2</sub>, HNO<sub>3</sub>, and HNO<sub>4</sub>.

	Peak Position, nm			Band Strength, $\times 10^{21}$ cm <sup>2</sup> molecules <sup>-1</sup> cm <sup>-1</sup>				Oscillator Strength, $\times 10^{-9}$		
	This Work	Ab Initio	Previous Work	A <sup>a</sup>	B <sup>a</sup>	C <sup>a</sup>	$1\sigma$ , <sup>b</sup> %	This Work	Ab Initio	Previous Work
<sup>3</sup> <sub>VOH</sub>										
H <sub>2</sub> O <sub>2</sub>	970	-	972 <sup>c</sup>	70	69	70	15	79	-	-
HNO <sub>3</sub>	983	-	983 <sup>d</sup>	-	29	29	15	33	-	26.3 <sup>d</sup>
HO <sub>2</sub> NO <sub>2</sub>	991	990 <sup>e</sup>	-	40	38	38	20	43	56.6 <sup>e</sup>	-
<sup>4</sup> <sub>VOH</sub>										
H <sub>2</sub> O <sub>2</sub>	747	-	748 <sup>f</sup>	4.3	4.5	4.5	25	5.0	-	-
HNO <sub>3</sub>	755	-	755 <sup>d</sup>	-	2.8	2.8	25	3.2	-	2.37 <sup>d</sup>
HO <sub>2</sub> NO <sub>2</sub>	763	762 <sup>e</sup>	-	-	-	3.0 <sup>g</sup>	50	3.4	4.0 <sup>e</sup>	-

<sup>a</sup>“A” is from UV measurements at 250 nm, “B” is from the 260 nm data, and “C” is to fit all the data points. UV cross sections used in data analysis from (7) in  $10^{-20}$  cm<sup>2</sup> molecules<sup>-1</sup> are as follows:

at 250 nm, 298 K, 8.3, 1.97, and 41.2 for  $\sigma_{\text{H}_2\text{O}_2}$ ,  $\sigma_{\text{HNO}_3}$ , and  $\sigma_{\text{HNO}_4}$ , respectively;

at 250 nm, 273 K, 8.3, 1.91, and 41.2 for  $\sigma_{\text{H}_2\text{O}_2}$ ,  $\sigma_{\text{HNO}_3}$ , and  $\sigma_{\text{HNO}_4}$ , respectively;

at 260 nm, 298 K, 5.3, 1.91, and 28.5 for  $\sigma_{\text{H}_2\text{O}_2}$ ,  $\sigma_{\text{HNO}_3}$ , and  $\sigma_{\text{HNO}_4}$ , respectively;

at 260 nm, 273 K, 5.2, 1.86, and 28.5 for  $\sigma_{\text{H}_2\text{O}_2}$ ,  $\sigma_{\text{HNO}_3}$ , and  $\sigma_{\text{HNO}_4}$ , respectively.

On the basis of the original papers for the JPL assessment we estimate the uncertainty ( $1\sigma$ ) is 10% for the UV cross sections.

<sup>b</sup>One standard deviation not including uncertainty in the UV cross sections.

<sup>c</sup>From (53).

<sup>d</sup>From (10).

<sup>e</sup>From (13). See text for details.

<sup>f</sup>From (11).

<sup>g</sup>Estimation based on only two measurements.

uncertainty and the uncertainty of the UV cross sections from previous studies. The former is mainly composed of the observed S/N (5% for  $3\nu_{\text{OH}}$  and 15% for  $4\nu_{\text{OH}}$ ), uncertainties in the baseline (10%), and, in the case of  $\text{HNO}_4$ , errors in our estimate of the contributions due to  $\text{H}_2\text{O}_2$ ,  $\text{NO}_2$ , and  $\text{HNO}_3$  (5%). On the basis of the original papers used in the JPL97 assessment (7), we estimate the uncertainty in the UV cross sections is 10% for all the three species at 250 nm and 260 nm.

The band strength for  $\text{HNO}_3$  is in good agreement with the measurements of Donaldson *et al.* (10). The locations of the  $\text{H}_2\text{O}_2$  bands agree with previous measurements (53; 11). For  $\text{HNO}_4$ , the observed peak position for both  $3\nu_{\text{OH}}$  and  $4\nu_{\text{OH}}$  is in excellent agreement with the ab initio calculation of Fono *et al.* (13), while the measured oscillator strength is within 25% for  $3\nu_{\text{OH}}$  and 15% for  $4\nu_{\text{OH}}$  of the same calculation. Interestingly, despite the puzzling fact that the solution spectrum of  $3\nu_{\text{OH}}$  is blue-shifted by as much as  $\sim 20$  nm for  $\text{HNO}_4$  while for  $\text{HNO}_3$  it is red-shifted by  $\sim 32$  nm, the relative intensity scaling between gas and solution spectrum predicts gas-phase  $\text{HNO}_4$  cross sections in good agreement with our measurements.

Excitation of  $3\nu_{\text{OH}}$  and  $4\nu_{\text{OH}}$  will play only a small role in the atmospheric photochemistry of  $\text{HNO}_4$  even if this process is dissociative. The solar flux near  $10,000\text{ cm}^{-1}$  (1000 nm) is approximately  $4 \times 10^{13}\text{ photons cm}^{-2}\text{ sec}^{-1}/\text{cm}^{-1}$  (28). Because the atmosphere is essentially transparent at this wavelength, the actinic flux is approximately the same as the solar flux and will not vary with solar zenith angle (SZA) during the daytime (neglecting the planetary albedo). Thus, by simply multiplying our measured integrated band strength by the solar flux, we obtain a photolysis rate for  $\text{HNO}_4$  via excitation of  $3\nu_{\text{OH}}$  of  $\sim 1.5 \times 10^{-6}\text{ sec}^{-1}$ , essentially independent of SZA. This is nearly an order of magnitude smaller than the photolysis rate of the missing source calculated by Wennberg *et al.* (50).

While the photolysis of  $\text{HNO}_4$  via the excitation of  $3\nu_{\text{OH}}$  is essentially independent of SZA, UV photolysis does depend strongly on the ozone optical depth and thus drops off rapidly with increasing SZA. Excitation of  $3\nu_{\text{OH}}$  significantly increases the photolysis rate of  $\text{HNO}_4$  in the lower stratosphere only for  $\text{SZA} > 80^\circ$  (R. J. Salawitch, personal communication). Therefore, only at high latitudes, where the Sun remains at high SZA for a significant fraction of the day, will inclusion of this overtone-induced dissociation process alter the calculated concentration of  $\text{HNO}_4$  (50). For equinox conditions at  $60^\circ$  latitude the overtone excitation increases the 24-hour average photolysis rate of  $\text{HNO}_4$  by

approximately 20% in the lower stratosphere. At lower latitudes the increase is much smaller (a few percent).

### 3.2.3 FTIR Spectrum of HNO<sub>4</sub>

To extend our measurements to longer wavelengths, FTIR spectroscopy was used to obtain HNO<sub>4</sub> cross sections over the spectral region of 1,200 - 10,500 cm<sup>-1</sup> (952 - 8,333 nm). The FTIR spectrometer used in this study was a nitrogen-purged Magna-IR 560 from Nicolet. It was equipped with a white light source, a CaF<sub>2</sub> beamsplitter and an MCT detector. HNO<sub>4</sub> was prepared by the same method described in Section 3.2.2. A quartz cell with CaF<sub>2</sub> windows was used at room temperature inside the spectrometer. Gaseous HNO<sub>4</sub> was introduced into the cell by passing pre-cooled N<sub>2</sub> through the PNA sample, which was contained in a reservoir placed in an ice/water bath. The pressure inside the cell and the bubbler was maintained at ~30 torr by adjusting a needle valve between the cell and the vacuum pump. Spectra were taken at 8 cm<sup>-1</sup> resolution with 3000 scans obtained over 30 minutes co-added. Shown in Figure 3.7 to 3.10 are HNO<sub>4</sub> spectra in four segments. They were derived by subtracting features from the impurities H<sub>2</sub>O<sub>2</sub>, H<sub>2</sub>O and HNO<sub>3</sub>, whose spectra were taken separately under similar conditions. Subtraction of NO<sub>2</sub> bands were not conducted, therefore some NO<sub>2</sub> bands can be seen (e.g., the feature near 1600 cm<sup>-1</sup>).

The notation used for the HNO<sub>4</sub> IR fundamental bands are taken from Zabel *et al.* (51) and reproduced here in Table 3.2. The following HNO<sub>4</sub> bands can be seen in the FTIR spectrum: in Fig. 3.7,  $\nu_2$ ,  $\nu_3$ ,  $\nu_4$ ; in Fig. 3.8,  $\nu_1$  and a band near 3015 cm<sup>-1</sup>, which is probably  $\nu_2 + \nu_4$ , analogous to a similar band assignment in HNO<sub>3</sub> (44). In Fig. 3.9, two bands are observed at 4907 and 6255 cm<sup>-1</sup>, in addition to  $2\nu_1$  (6950 cm<sup>-1</sup>); in Fig. 3.10, a band at 8242 cm<sup>-1</sup> is observed and an assignment of  $2\nu_1 + \nu_3$  is suggested.  $3\nu_1$  band can be seen near 10,090 cm<sup>-1</sup> on the FTIR spectrum (not shown here), but the S/N is close to unity.

To test our ability to quantitatively determine the band intensities of overtones in the NIR using this technique, the spectrum of methanol (CH<sub>3</sub>OH) was examined. The measured relative strengths of  $\nu_1$ ,  $2\nu_1$  and  $3\nu_1$  (1 : 6.2 : 20) obtained for methanol are in excellent agreement with those reported in the literature (33).

The relative strengths of  $\nu_1$ ,  $\nu_2$ ,  $\nu_3$  and  $\nu_4$  of HNO<sub>4</sub> observed in our FTIR spectra are also in good agreement with those reported by May and Friedl (23), as shown in Table 3.3.

Table 3.2: Vibrational frequencies of HNO<sub>4</sub>.

Wavenumber (cm <sup>-1</sup> )	Vibration	Notation
3538	OH stretch	v <sub>1</sub>
1725	NO <sub>2</sub> asym stretch	v <sub>2</sub>
1396	OH bend	v <sub>3</sub>
1304	NO <sub>2</sub> sym stretch	v <sub>4</sub>
880	OO stretch	v <sub>5</sub>
803	NO stretch	v <sub>6</sub>
735	NO <sub>2</sub> deform	v <sub>7</sub>
633	NO <sub>2</sub> wag	v <sub>8</sub>
500		v <sub>9</sub>
400		v <sub>10</sub>
175	torsion	v <sub>11</sub>
80	torsion	v <sub>12</sub>

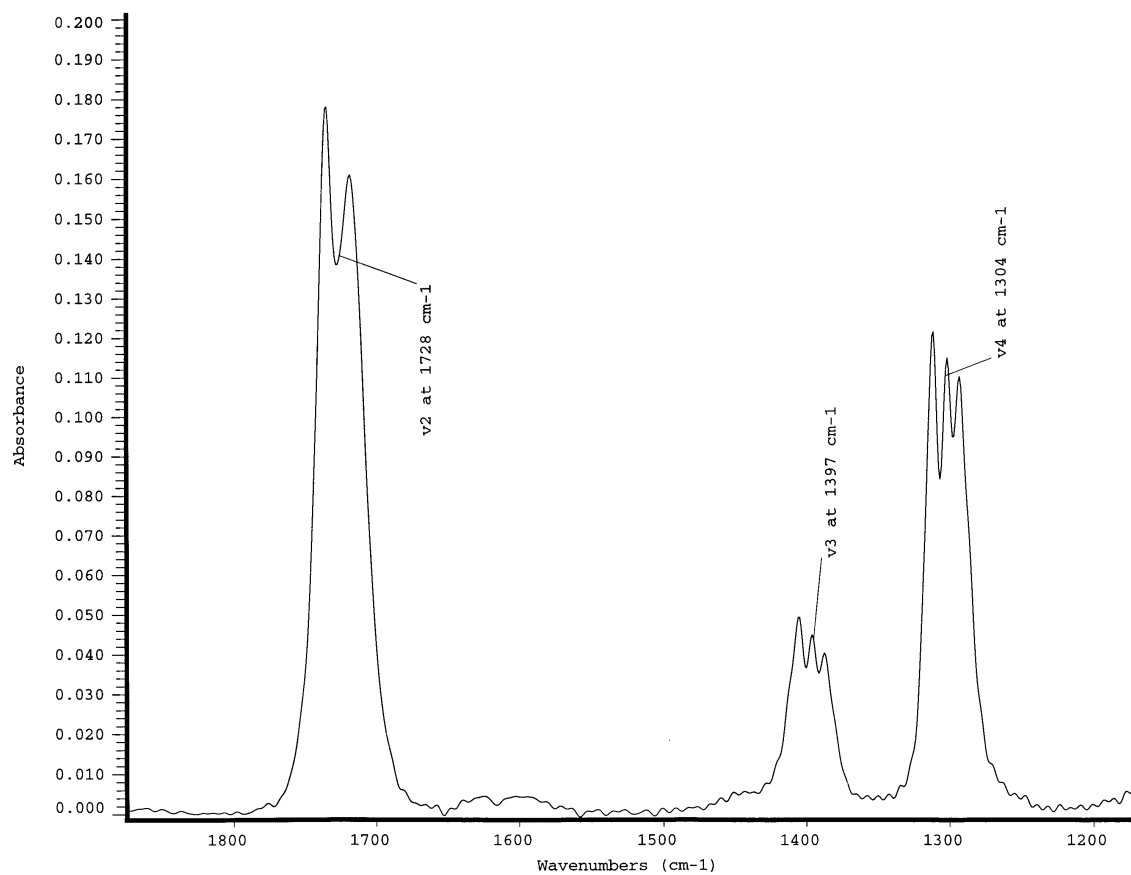


Figure 3.7: FTIR spectrum of HNO<sub>4</sub> from 1200 - 1900 cm<sup>-1</sup>.

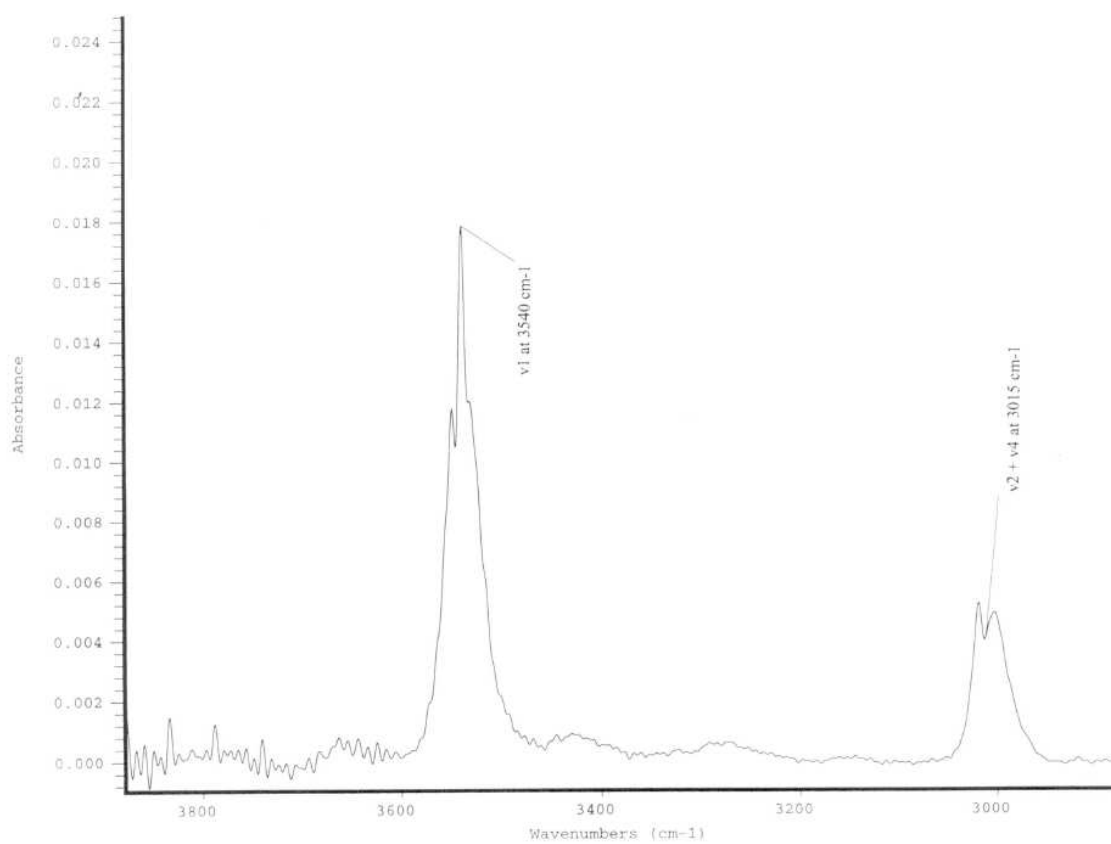


Figure 3.8: FTIR spectrum of HNO<sub>4</sub> from 2850 - 3850 cm<sup>-1</sup>.

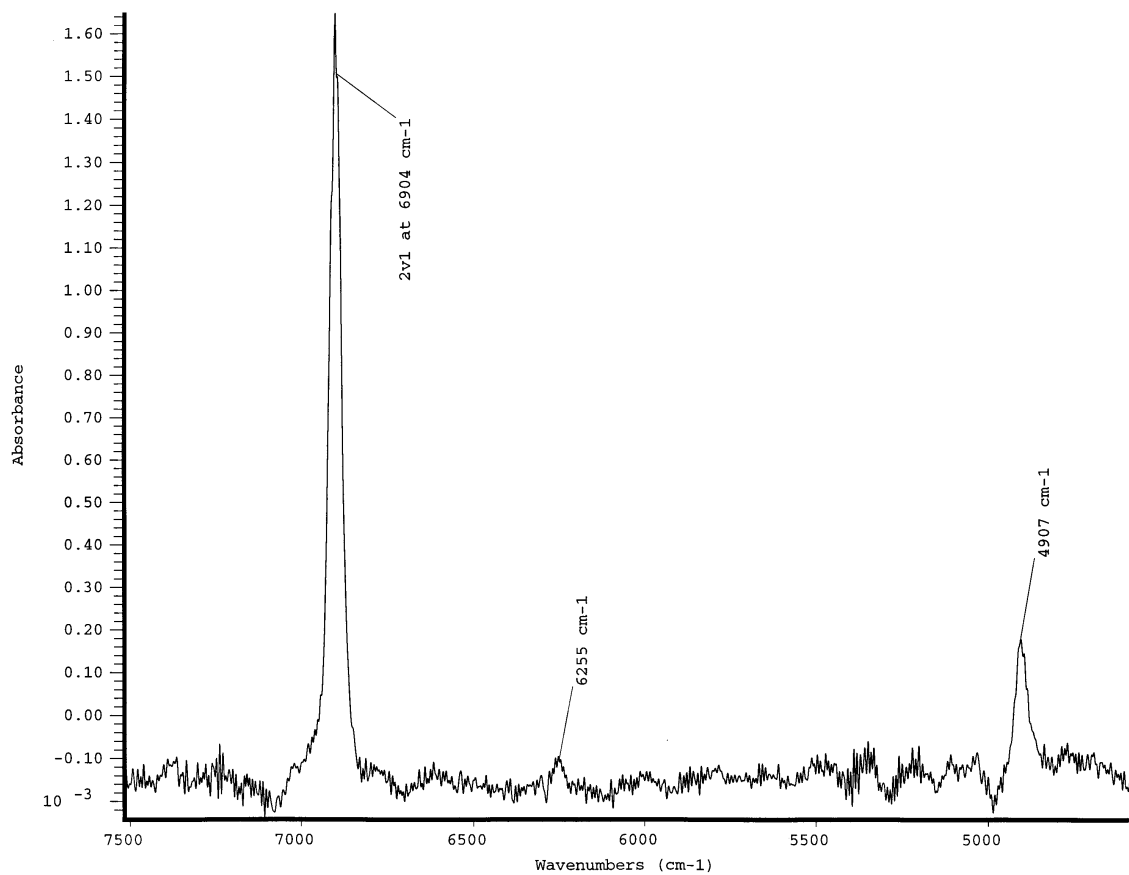


Figure 3.9: FTIR spectrum of HNO<sub>4</sub> from 4550 - 7540 cm<sup>-1</sup>.

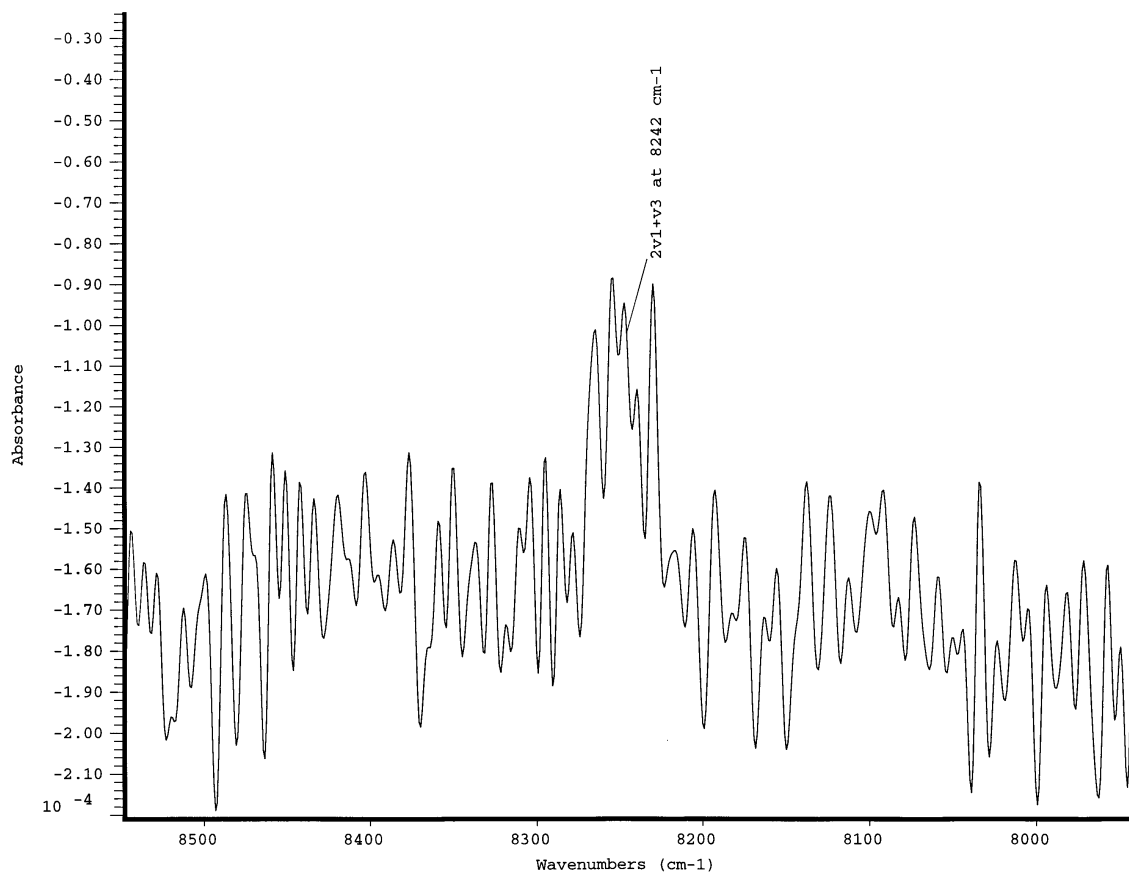
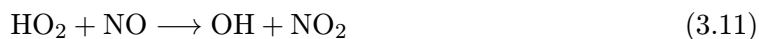


Figure 3.10: FTIR spectrum of HNO<sub>4</sub> from 7900 - 8600 cm<sup>-1</sup>.

The measurement by May and Friedl was conducted at 220 K and our FTIR spectra were collected at room temperature. Also listed in Table 3.3 is the intensity of  $3\nu_1$  relative to  $\nu_1$ . The S/N in the region near  $3\nu_1$  in FTIR spectra is too low to enable quantitative measurement of its relative strength. Instead, it is assumed here that the absolute measurements of  $3\nu_1$  determined above and those for  $\nu_1 \rightarrow \nu_4$  determined by May and Friedl (23) are both accurate. This assumption is likely correct as the methods used in these two studies are essentially the same. The largest source of uncertainty in both studies is the assumed UV cross sections of  $\text{HNO}_4$ . Such errors will cancel in determining the *relative* cross sections, however, because both studies employed the same UV cross sections. With this assumption, the ratio of integrated band strengths for  $\nu_1$  and  $3\nu_1$  is determined to be 160. The relative scaling in band strengths is conducted for all other bands relative to  $3\nu_1$ , and their absolute intensities are then calculated. The results are shown in Table 3.4.

### 3.2.4 Quantum Yields

To obtain photodissociation quantum yields for the vibrational transitions discussed in Section 3.2.2, a tunable IR source has been coupled with a highly sensitive detection method of the photodissociation product.  $\text{HO}_2$  produced from the NIR photodissociation of  $\text{HNO}_4$  is detected via OH LIF after chemical titration to OH with NO:



The production rate of  $\text{HO}_2$ , normalized by the IR laser fluence, has been measured for all rovibrational transitions of  $\text{HNO}_4$  between 950 and 2000 nm. The quantum yield, relative to that of  $3\nu_1$ , is determined from the ratio of this normalized signal to the measured band absorption cross sections obtained in Section 3.2.2 and 3.2.3.

## Experimental

The apparatus used in this experiment is schematically depicted in Figure 3.11. It consists of a flow tube/reaction cell, two laser systems for photolyzing  $\text{HNO}_4$  and exciting OH, respectively, and an OH LIF detection axis. The photolysis and LIF laser beams cross the gas flow colinearly.

Table 3.3: Relative strength of the  $\nu_1$ ,  $\nu_2$ ,  $\nu_3$  and  $\nu_4$  modes of  $\text{HNO}_4$ .

	$\nu_1$	$\nu_2$	$\nu_3$	$\nu_4$	$3\nu_1$
Band Center ( $\text{cm}^{-1}$ )	3540	1728	1397	1304	10090
From FTIR spectrum: $\int$ Band Intensity / $\int$ Band Intensity of $\nu_1$	1	8.05	2.06	4.85	
From May & Friedl (1995): $\int$ Band Intensity / $\int$ Band Intensity of $\nu_1$	1	8.03	2.05	5.05	1/160 <sup>a</sup>

<sup>a</sup>Based on the absolute intensity of  $3\nu_1$  determined in Section 3.2.2 and that of  $\nu_1$  measured by May and Friedl (23).

Table 3.4: Integrated strength of NIR HNO<sub>4</sub> bands from the FTIR spectrum.

	$\nu_1$	$\nu_2 + \nu_4$	c.b.	c.b.	$2\nu_1$	$2\nu_1 + \nu_3$	$3\nu_1$
Band Center (cm <sup>-1</sup> )	3540	3015	4907	6255	6904	8242	10090
$\int$ Band Intensity / $\int$ Band Intensity of $3\nu_1$	160±15	41±4	3.7±0.4	0.9±0.2	16±2	0.6±0.2	1
Intensity (10 <sup>-20</sup> cm <sup>2</sup> molec <sup>-1</sup> cm <sup>-1</sup> )	610±57	160±16	14±1.5	3.4±0.8	61±8	2.2±0.7	3.8

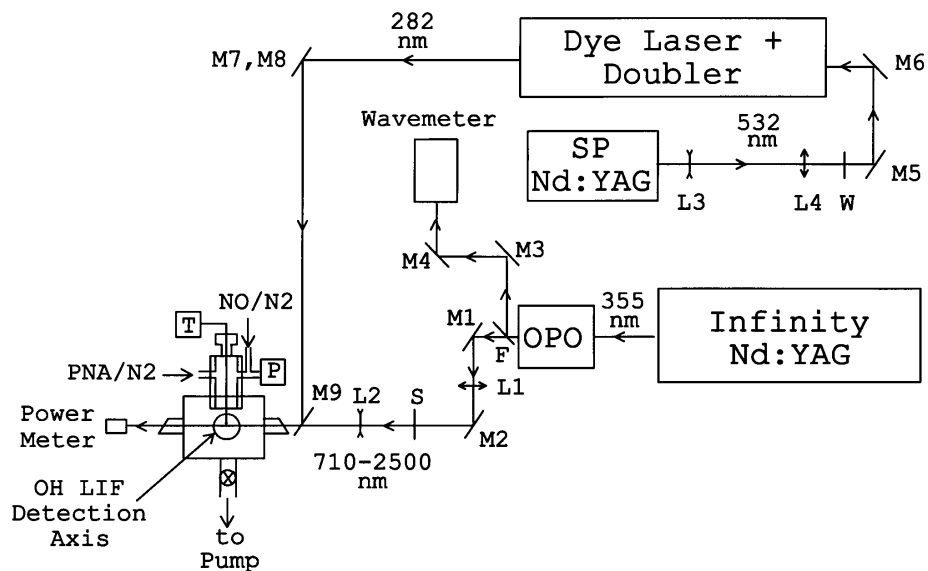


Figure 3.11: Schematic diagram of the action spectrum experimental apparatus. F: long-pass filter; L1, L2, L3, L4: lenses; M1, M2, M3, M4: vis/NIR reflectors; M5, M6: 532 nm reflectors; M7, M8, M9: 266 nm reflectors; P: pressure transducer; S: shutter; T: thermister; and W: waveplate.

**1. Flow System** Two o-ring interfaced cells together form the flow tube. A pyrex cell (1" I.D.) with a cooling jacket extends to within  $\sim 0.5$  cm of the center of a second aluminum cell. The second cell (called the LIF chamber) allows the laser beams to pass across the flow at its center and supports the LIF detection apparatus on an axis perpendicular to the gas flow and laser propagation. The jacketed cell is designed to keep the gas mixture cold as it passes into the photolysis zone thereby, minimizing the thermal decomposition of  $\text{HNO}_4$ .

The preparation of  $\text{HNO}_4$  samples is performed as described in Section 3.2.2, and the resulting  $\text{HNO}_4$  sample is kept in an ice/water bath throughout the experiment. Dry nitrogen evolved from liquid nitrogen is used as the carrier gas in this study. Three major gas flows are employed: nitrogen passing through the  $\text{HNO}_4$  reservoir ( $\sim 40$  sccm);  $\sim 100$  sccm nitric oxide (2000 ppm NO in UHP  $\text{N}_2$ , Matheson) for titration of  $\text{HO}_2$ ; and a flow of  $\sim 40$  sccm nitrogen to facilitate the adjustment of the total pressure and flow conditions within the photolysis region. In addition, a minor nitrogen flow (20 sccm) is used to purge the side arms of the LIF chamber to keep  $\text{HNO}_4$  from entering. Flow settings are adjusted with MKS flow meters using an in-house made control box. All the flows except the minor purge flow are pre-cooled by passing through ice/water baths.

The pressure in the PNA reservoir (30-100 torr) is adjusted using a Teflon needle valve located between the reservoir and the LIF cell and is monitored with a 1000 torr MKS pressure transducer. Pressure measurements in the LIF chamber are obtained with two MKS pressure transducers (10 and 50 torr full scale, respectively), covering the range of pressures used in this work (i.e., 2 - 30 torr). Temperature in the photolysis region is measured with a calibrated thermister inserted from the end port on the jacketed cell to the center of the LIF chamber. When the cell is cooled by circulating water from an ice/water bath, the temperature at the LIF chamber center stabilizes at 278 K. Special care is taken to make sure that the thermister is close to the center of the chamber but out of the UV laser beams to avoid producing large laser scatter.

**2. Tunable Photolysis Laser** The photolysis of  $\text{HNO}_4$  is conducted with the idler output of the type II BBO OPO described in Chapter 1. A longpass filter (RG715, Schotts), F, is placed after the output coupler of the OPO. This filter serves two purposes, it removes the residual 355 nm and reflects the signal output of the OPO. The signal is directed toward a wavemeter in order to accurately determine the OPO frequency.

Initially, the wavelength separation was accomplished with a Pellin Broca prism. Because of the dispersion of the prism, it was rotated simultaneously as the OPO was tuned to maintain the same pointing direction for the NIR beam. The optimal position of the prism was determined by maximizing the laser power exiting the LIF chamber. It was found, however, that the LIF signal produced from  $\text{HNO}_4$  photodissociation is very sensitive to the prism position while the observed laser power transmitted is relatively insensitive, as demonstrated in Figure 3.12. This sensitivity is attributed to the spatial overlap of the photolysis and LIF laser beams. To eliminate the beam overlap uncertainty caused by the use of a prism, a longpass filter is used instead along with two visible/NIR reflectors, M1 and M2, to direct the NIR beam toward the LIF chamber. The output pointing direction of the walkoff compensated OPO remains fixed as the wavelength is scanned and thus minimal error is introduced in the measurement of the relative quantum yield. The drawback of this solution is that some of the NIR light is lost in the filter.

A pair of quartz lenses (OptoSigma), L1 of 250 mm f.l. (focal length) and L2 of -500 mm f.l., is used to overcome the large divergence of the IR and to collimate the beam to a size of approximately  $0.5 \text{ cm} \times 0.5 \text{ cm}$ . A shutter, S, is employed to chop the photolysis beam, thus allowing differentiation between the NIR photolysis signal from those produced by laser scatter, photolysis of  $\text{HNO}_4$  by the UV laser, and  $\text{HNO}_4$  thermal decomposition. The shutter is computer-automated through a TTL signal from a Data Acquisition Board (PCI-MIO-16E-4, National Instruments).

**3. LIF Detection of OH** The LIF technique has long been used to make sensitive and selective measurements of concentration of the OH radicals both in the laboratory and in the atmosphere. An energy diagram of the fluorescence process employed in this study is shown in Figure 3.13. The  $Q_1(2)$  transition is pumped near 282 nm, leaving the OH molecules in the first vibrationally excited level of the excited electronic state ( $\tilde{A}^2\Sigma^+ (\nu' = 1) \leftarrow \tilde{X}^2\Pi_{3/2} (\nu'' = 0)$ ). Following collisional energy transfer, the excited OH molecules are quenched to the ground vibrational state of the excited electronic state ( $\nu' = 0$ ). Fluorescence near 309 nm is then observed from many rotational states ( $\tilde{A}^2\Sigma^+ (\nu' = 0) \rightarrow \tilde{X}^2\Pi (\nu'' = 0)$ ).

**A. UV Laser System** UV laser radiation near 282 nm is generated by frequency doubling the fundamental of a dye laser pumped by the 532 nm output from a diode-pumped, Q-

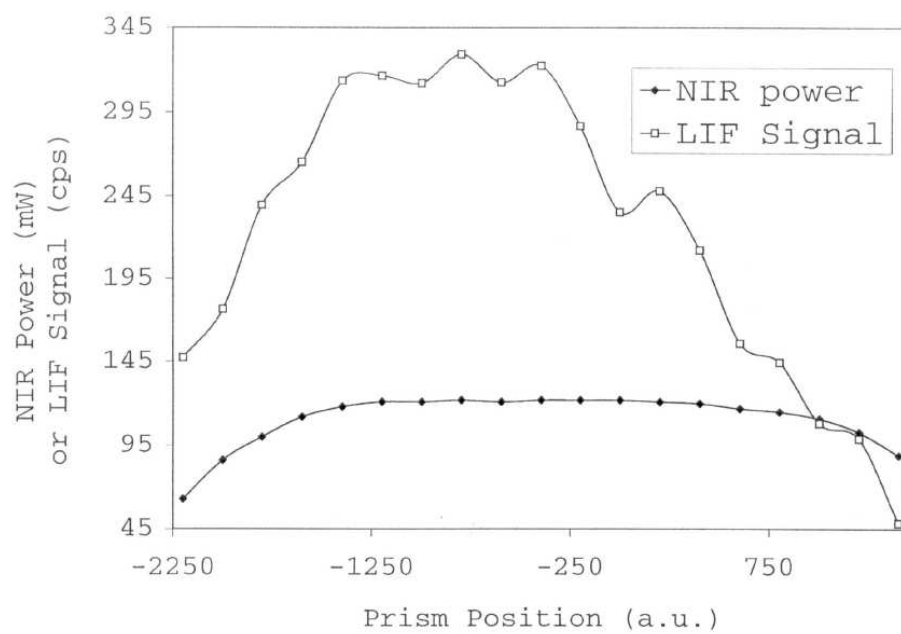


Figure 3.12: Sensitivity test for NIR/UV beam overlap with the Pellin Broca prism.

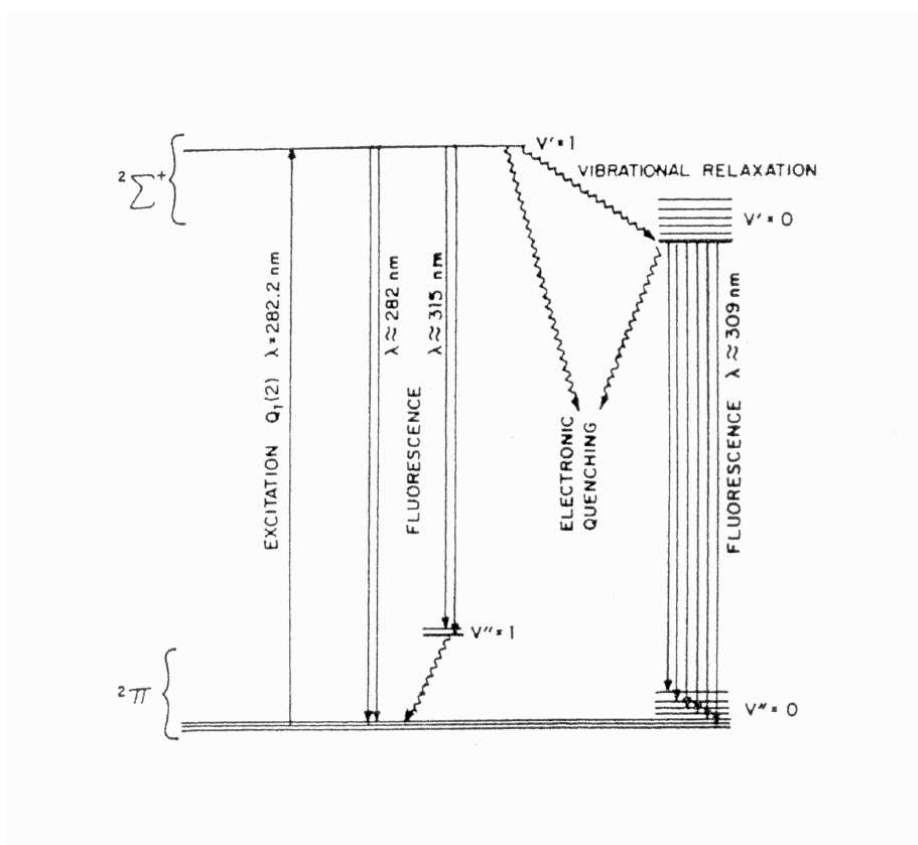


Figure 3.13: Spectroscopy and energy transfer in the LIF detection scheme used for OH. From (49).

switched Nd:YAG laser. The Nd:YAG laser (T40-X30-532QA, Spectra Physics) is pumped by two 20 W laser diode bars emitting near 800 nm, which are fiber coupled to the laser head. The Nd:YAG laser is Q-switched at 5 kHz and the 1064 nm emission undergoes second harmonic generation (with a LBO crystal) to produce 532 nm pulses. Two BBAR coated (for 430-700 nm) BK7 lenses, L3 of -50 mm f.l. and L4 of 500 mm f.l. (Newport), are used to expand the beam size to approximately  $\varnothing$ 1 cm in order to optimize the pumping area on the dye laser cuvette. A 532 nm AR-coated half waveplate (Coherent), W, is used to maximize the vertical polarization of the 532 nm light, which is optimal for the oscillation of this dye laser. The collimated 532 nm laser beam is then coupled into the dye laser by means of two 532 nm reflectors (OptoSigma), M3 and M4.

The dye laser (FL3001, Lambda Physik) operates on one dye cell that acts as both an oscillator and amplifier. The LP etalon option is not installed. Rhodamine 6G (LP) in methanol (0.1 g/l), with a fluorescence maximum at 560 nm, serves as the dye solution. A cooler (RTE-110, Neslab) is used to keep the dye solution at a constant temperature ( $\sim 23^\circ$  C) while the laser is in operation. The 564 nm fundamental output of the dye laser is focused into a KDP crystal and subsequently doubled to 282 nm. Separation of the UV output from the fundamental is achieved via reflecting the UV beam off three 266 nm mirrors (Optosigma), M5, M6 and M7, which together adjust its height and direct it into the reaction cell. Mirror M7 also serves as the combining mirror for the IR photolysis and the UV beams.

Due to possible damage of the doubling crystal inside the laser head of the SP Nd:YAG laser, the total 532 nm pumping power is presently about 1.2 W at 5 kHz ( $\sim 240 \mu\text{J}/\text{pulse}$ ), which is approximately 40% of the factory specification. Despite the extremely low pulse energy and the non-TEM<sub>00</sub> mode structure of the pump source, stable lasing of the dye laser occurs with  $\sim 0.5 - 1$  mW average power levels at 282 nm. This is achieved because of the optimized allocation of pump energy into the oscillator and amplifier, and the excellent alignment of the dye laser cavity. The 564 nm output exhibits a linewidth (FWHM) of  $\sim 0.20 \text{ cm}^{-1}$ , well matched to the OH absorption linewidth ( $0.10 - 0.15 \text{ cm}^{-1}$ ).

Wavelength calibration of the dye laser is accomplished by scanning across the 562 - 566 nm region (i.e., 281 - 283 nm in the UV) with OH produced by flowing moist air over a glowing NiChrome filament (49), and comparing the observed OH fluorescence lines to known spectra (8). Figure 3.14 shows a portion of such scan near 282 nm. The  $Q_1(2)/Q_{21}(2)$

doublet, which is used for OH detection in this study, has a separation of  $\sim 0.6 \text{ cm}^{-1}$  and is partially resolved in this spectrum, demonstrating the narrow linewidth of the UV light ( $\sim 0.3 - 0.4 \text{ cm}^{-1}$ ).

**B. LIF Detection of OH** The design of the LIF detection axis is directly copied from the ER2 HO<sub>x</sub> instrument minus the use of a multi-pass White cell for the excitation laser (49). Figure 3.15 shows a cross sectional diagram of this design. The NIR and the UV beams are sent colinearly into the side arm of the LIF chamber through a plain quartz window (ESCO Products) mounted at Brewster's angle. Before entering the detection region, the laser beams pass through a set of optical baffles with a  $1 \text{ cm} \times 1 \text{ cm}$  aperture to reduce the laser scatter. They then transverse the flow tube before exiting via series of baffles and another quartz window (ESCO Products). The NIR power is measured with a thermopile power meter (Scientech) at the exit port. Since the UV intensity is much lower than that of the NIR, the lack of separation of the NIR from the UV light does not significantly influence our determination of the NIR power.

The OH fluorescence is detected perpendicularly to the direction of propagation of the exciting radiation and the gas flow. The solid angle of the fluorescence collection system is roughly doubled with a retro-reflecting mirror (Newport) opposite the collection lens. The radius of curvature of this mirror is equal to its spacing from the center of the LIF chamber. After a plain quartz window (ESCO Products), which forms the flow tube seal, a series of optics is used to provide adequate spectral filtering while maintaining a high transmission at the desired wavelength (310 nm). First, the light is pseudo-collimated using a plain quartz lens (40 mm diameter and 60 mm f.l., OptoSigma) chosen assuming the fluorescence originates from a point source at the center of the LIF chamber. The light then passes through a narrow-band interference filter with a bandwidth (FWHM) of 4.8 nm centered at 308.9 nm and peak transmission of 65% (Barr Associates). Light between 200 - 750 nm outside of the transmission region is blocked to  $< 10^{-5}$ . Transmission at 302 nm is  $< 10^{-3}$  and that at 282 nm is  $< 10^{-8}$ , according to the manufacturer. The light is next folded by a dielectric-coated turning mirror (Broomer Research) which transmits more than 99% of red/NIR wavelengths and reflects light at 300 - 350 nm. A final plain quartz lens (40 mm diameter and 60 mm f.l., OptoSigma) focuses the fluorescence onto the photosensitive area of a photo-multiplier tube (PMT).

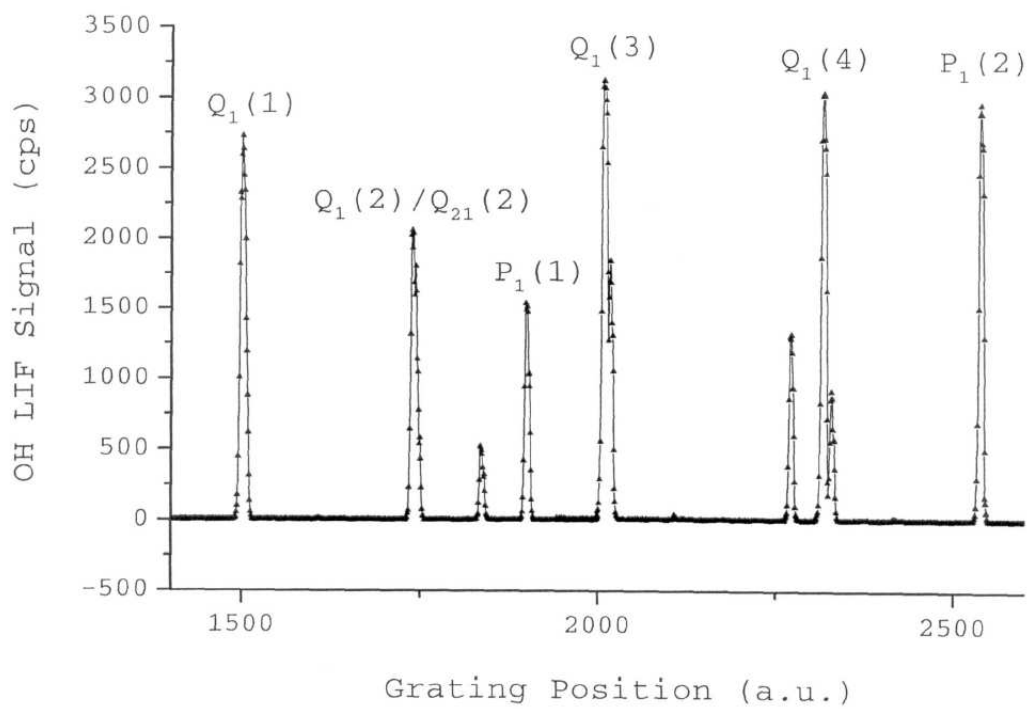


Figure 3.14: OH transitions observed with the LIF apparatus. The  $Q_1(2)/Q_{21}(2)$  doublet is used for OH detection in this study.

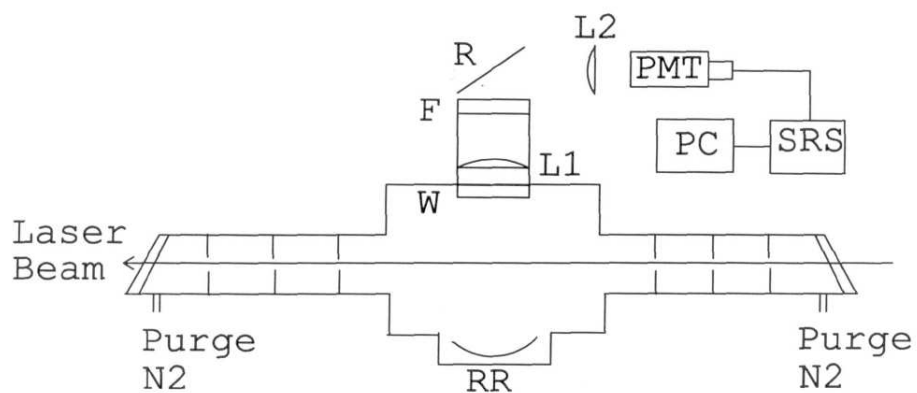


Figure 3.15: Cross sectional diagram of the LIF detection axis used in this study. In this view, the gas flow is pointing out of the paper. RR: retro-reflector; W: quartz window; L1 and L2: lenses; F: interference filter; R: UV reflector. The signal from PMT is registered with a SRS photon counter and the data are stored in a PC.

The PMT (541N bialkali, EMR) is packaged in a single assembly that includes the high voltage power supply and pulse amplifier/discriminator (PAD). Unfortunately the PAD no longer works, so a charge-sensitive preamplifier (A-101, AMPTEK) has been added close to the PMT output. The output pulse from the AMPTEK amplifier has a width of  $\sim 150$  nsec, which can be increased to greater than  $1 \mu\text{sec}$  by the addition of a capacitor.

A gated photon counter (SR400, Stanford Research Systems) is used to record the pulses from the AMPTEK amplifier. The counter gate is triggered by a TTL (logic) signal from the Spectra Physics Nd:YAG laser, which is synchronized with the laser Q-switch. Since the OH excited state lifetime at pressures between 2 and 30 torr is between 500 and 30 nsec, the majority of the fluorescence signal is observed within a short time following the laser pulse. In these experiments, the gate is set to open shortly after the laser pulse and close after a period of approximately twice the OH fluorescence lifetime. The advantage of this scheme is that it reduces the background signal due to other sources, such as laser scatter, PMT dark counts and room light. A second channel of the counter is used to record the onset of the TTL signal that controls the shutter in the path of the photolysis beam. This channel can also be used to simultaneously count the signal from the detector in continuous (ungated) mode, thereby providing a measure of the total fluorescence and the background signal impinging on the detector. The photon counter is controlled from a PC computer via an RS-232 connection. Data from both channels can be saved and plotted in real time using a data acquisition program developed in the application environment provided by the SRS's DDDA system.

**C. The Conversion of HO<sub>2</sub> to OH and the Temporal Evolution of OH** When the photodissociation of HNO<sub>4</sub> occurs as a result of the absorption of NIR radiation, only HO<sub>2</sub> is formed along with NO<sub>2</sub>. OH signal is sometimes seen without the presence of NO but this is not systematic and is attributed to the occasional presence of a large amount of NO<sub>x</sub> impurity in the HNO<sub>4</sub> sample mixture. The lack of OH as a dissociation product is expected since photons with  $\lambda > 950$  nm do not possess enough energy to break the HO-ONO<sub>2</sub> bond ( $\sim 14,230 \text{ cm}^{-1}$  or 703 nm).

The time constant for the production of OH from HO<sub>2</sub> titration is calculated according

to

$$t = 1/k_{\text{HO}_2+\text{NO}} [\text{NO}],$$

where  $t$  is the reaction time (49). In this experiment,  $[\text{NO}]$  is varied to maximize the OH LIF signal. The concentration of NO is found to be optimized at  $10^{14}$  molec/cm<sup>3</sup>, corresponding to a HO<sub>2</sub> to OH conversion timescale of  $\sim 1$  msec ( $k_{\text{HO}_2+\text{NO}} = 8.6 \times 10^{-12}$  cm<sup>3</sup>/molec-sec at 278 K (7)). The fast conversion of HO<sub>2</sub> is needed, in part, because of the fast advection rate in the flow tube. Under our experimental conditions, at 3.5 torr the gases flow across the NIR photolysis beam at  $\sim 150$  cm/sec, yielding a residence time of only  $\sim 3$  msec. The resulting high  $[\text{NO}]$  level not only increases the photolysis signal, but also reduces the background signal due to thermal decomposition, as the OH produced is scavenged by HNO<sub>4</sub> (Reaction 3.2) before arriving to the detection region.

The temporal evolution of the OH LIF signal is also studied. Figure 3.16 shows the OH LIF signal measured as a function of time after the NIR laser fires. The OH appears promptly, consistent with the short HO<sub>2</sub>  $\rightarrow$  OH conversion timescale discussed above. It is apparent from the figure that the OH signal drops rapidly compared to the interval between two consecutive NIR laser pulses (i.e., 10 msec). A weighted linear fit gives a decay constant of  $\sim 1.6$  msec. Besides the advection process in the flow tube, reaction with HNO<sub>4</sub> (Reaction 3.2) also depletes [OH] in the LIF region. From offline FTIR measurements obtained under identical flow conditions,  $[\text{HNO}_4]$  in our flow tube is estimated to be  $1 - 5 \times 10^{14}$  molec/cm<sup>3</sup>. Therefore, the lifetime of OH is  $\sim 0.4 - 2$  msec before it is lost due to Reaction 3.2 ( $k_{\text{OH}+\text{HNO}_4} = 5.1 \times 10^{-12}$  cm<sup>3</sup>/molec-sec at 278 K (7)). Thus, the temporal decay of the OH signal reflects both the physical transport and chemical loss. Future studies where  $[\text{HNO}_4]$  is systematically varied would be warranted.

**D. Linearity of OH LIF System** The linearity of the OH LIF system is key to obtaining accurate measurements of the relative quantum yields. In the detector's linear regime, the observed OH signal,  $S_{\text{OH}}$ , can be expressed as

$$S_{\text{OH}} = \text{CEQ}[\text{OH}] \tag{3.12}$$

where  $C$  is a constant,  $E$  is the average power of the 282 nm laser (product of the laser pulse energy and the repetition rate) and  $Q$  is the fluorescence efficiency, which is a function

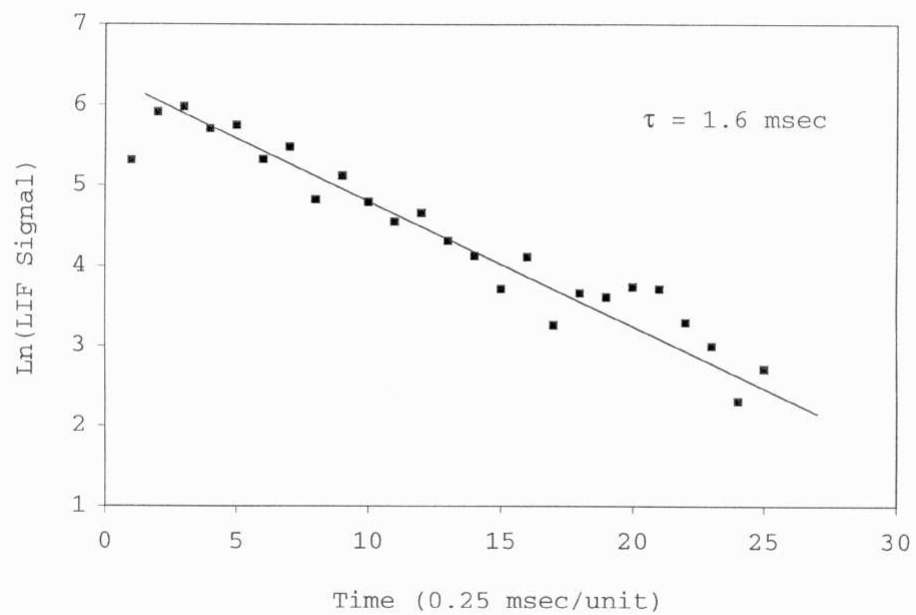


Figure 3.16: Temporal profile of the OH LIF signal from NIR photolysis obtained at 3.5 torr. The decay time constant is found to be  $\sim 1.6$  msec.

of pressure. The constant  $C$  accounts for factors such as the spectral overlap of the UV laser and OH absorption line, the spatial overlap of the UV and NIR beams, the optical transmission efficiency, and the PMT quantum yield. Linear counting can be only achieved up to a certain signal rate due to counting saturation. The UV pulse energy employed in this study is too low for optical saturation effects to be important.

The linearity of the LIF system is first studied with the filament OH source described above. Figure 3.17 illustrates how the LIF signal varies as a function of UV power at different pressures. Each curve is obtained by varying the power of the UV laser at constant  $[OH]$  and at constant pressure. The laser power is monitored with a UV-sensitive silicon photodiode (UDT-555UV, UDT) operated in the linear regime. Two of the curves are obtained at the same pressure (10 torr) but with different  $[OH]$ . At sufficiently low signal levels, these results are consistent with a linear relationship between signal and UV power. It is worthwhile to note two other points. First, the maximum count level can exceed the laser repetition rate (i.e., 5000 Hz). The gate width is set several times longer than the dead time ( $\sim 150$  nsec) of the AMPTEK amplifier, thus more than one count can be registered for each laser shot. Secondly, the upper limit of linear counting decreases with increased pressure. At higher pressure, the OH lifetime is shortened and the fluorescence occurs over a shorter period after excitation. This affects the counting in two ways. The prompt fluorescence precludes observation of more than one photon per laser shot. In addition, because the gate opens 60 nsec after the laser pulse, a photon arriving before the gate opens effectively blocks the gate for other events. This effect explains the observed reduction in signal with UV power at high signal rates.

In the NIR photolysis of  $HNO_4$ , the non-linearity occurs at much lower absolute count rates than with the filament OH source. This is not surprising given the pulsed nature of the photolysis signal (see Figure 3.16). The significant non-linearity is reflected in the photolysis power dependence tests performed for  $2\nu_1$ , as presented in Figure 3.18, 3.19 and 3.20. In Figure 3.18, spectra of  $HNO_4$   $2\nu_1$  band are taken at different photolysis laser powers while other conditions, such as the pressure and the UV power level, remain the same. It shows non-linearity of the LIF signal when it approaches 1000 cps (counts per second). This occurs when the NIR laser power is higher than  $\sim 88$  mW at the center wavelength of this band. The onset of non-linearity occurs at a much lower signal rate than observed for the continuous OH sources at similar pressure (5 torr in this test). The LIF signals are

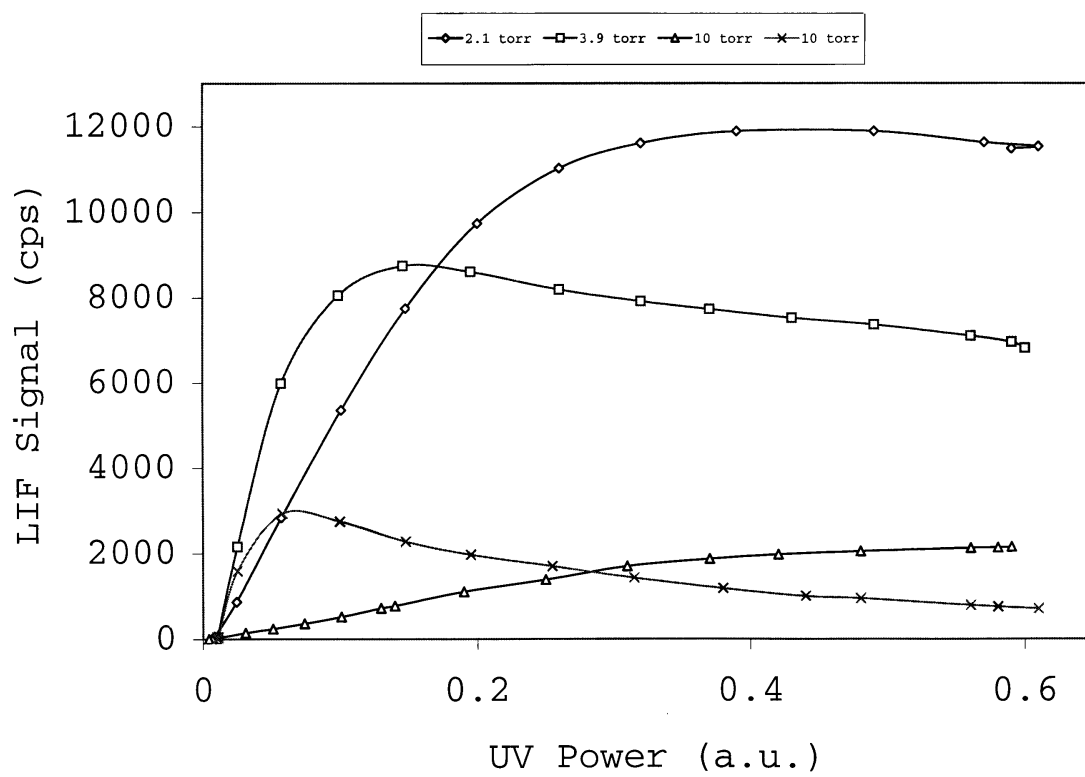


Figure 3.17: Tests of the linearity of the counting system with a continuous OH source.

normalized with NIR power and plotted in Figure 3.19. It can be seen that the signal is non-linear at center but linear with the NIR power at the wings of this  $\text{HNO}_4$  band, where the counting rate is much lower.

To investigate whether the observed non-linearity is due to saturation of the counting system or truly nonlinear optical behavior in the photolysis at  $2\nu_1$ , another test was conducted and is shown in Figure 3.20. At one photolysis wavelength close to the peak of  $2\nu_1$  (i.e.,  $\sim 1459$  nm), the LIF signal is monitored as a function of NIR power for a given UV laser power. The test is repeated at 4.3 torr for several different UV laser powers by inserting UV ND filters. An apparent non-linearity is observed at full UV power. Linear fits except for the test with full UV level are conducted and shown in the figure. The ratio between the three slopes,  $5.2 : 4.3 : 1.7 = 3 : 2.5 : 1$ , is close to the marked UV power,  $0.5 : 0.4 : 0.2 = 2.5 : 2 : 1$ . The latter is taken from the transmission of these ND filters, which is specified for 355 nm. Experiments to test the transmissions of these filters at 282 nm are yet to be performed. This set of tests has shown that the upper limit of the linear counting regime at 4.3 torr is  $\sim 500$  cps. The data presented in Figure 3.18 and 3.19 are obtained at full UV level. It is apparent from Figure 3.20 that, at  $\sim 1000$  cps, i.e., the counting level at the center of  $2\nu_1$  band for three curves in Figure 3.18, the response of the counting system is no longer linear. As a matter of fact, the linear counting regime suggests the test conducted at  $\sim 48$  mW in that figure is not linear at the band center, either. It is noted that the  $[\text{HNO}_4]$  changes over time, but the correction needed for the changes in  $[\text{HNO}_4]$  is insignificant for these tests. The observed non-linearity is due to saturation of the counting system. Similar tests performed for the  $3\nu_1$  band of  $\text{HNO}_4$  have demonstrated linearity. This is consistent with the conclusion drawn above given that the counting rate at  $3\nu_1$  of  $\text{HNO}_4$  has always been sufficiently low to be in the linear regime. For the results presented in the next section, the LIF signals are obtained in the linear regime.

## Results

Several vibrational bands are found to be dissociative in the wavelength range between 950 - 2000 nm. They include  $3\nu_1$  at 991 nm ( $10,090\text{ cm}^{-1}$ ), a combination band at 1213 nm ( $8242\text{ cm}^{-1}$ ),  $2\nu_1$  at 1448 nm ( $6904\text{ cm}^{-1}$ ), and another combination band at 1599 nm ( $6255\text{ cm}^{-1}$ ). As previously mentioned, an assignment of  $2\nu_1 + \nu_3$  is suggested for the band at 1213 nm. The combination band at  $4907\text{ cm}^{-1}$  is also probed but no OH LIF signal is

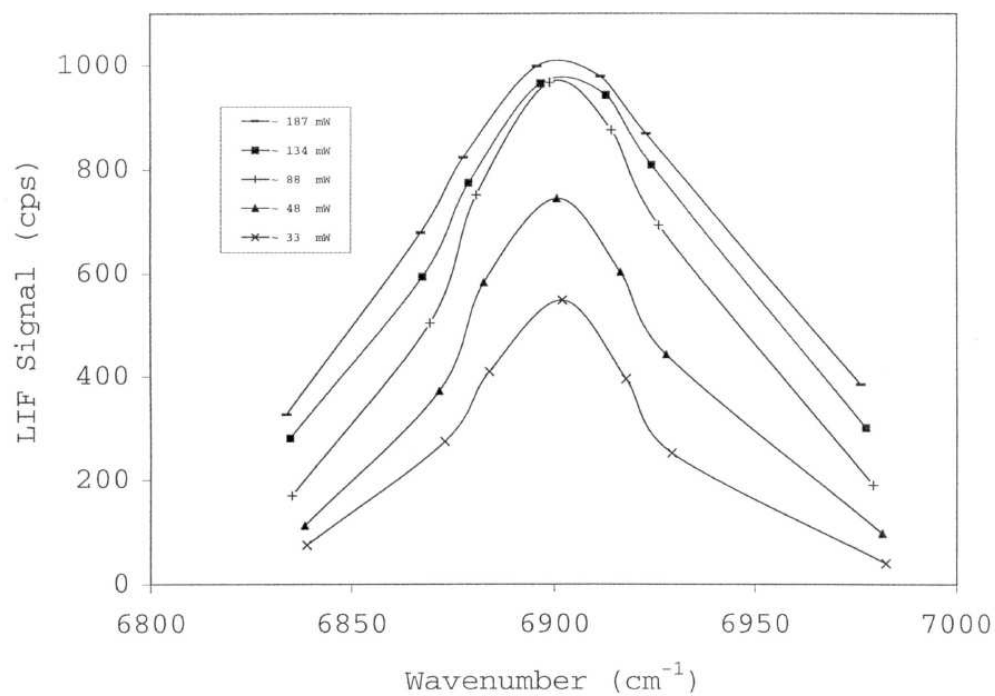


Figure 3.18: Non-linearity in the  $2\nu_1$  photolysis with increased NIR power. Marked are the laser powers at the center wavelength of the  $2\nu_1$  band. Power variation is within 15% of these values across the entire band.

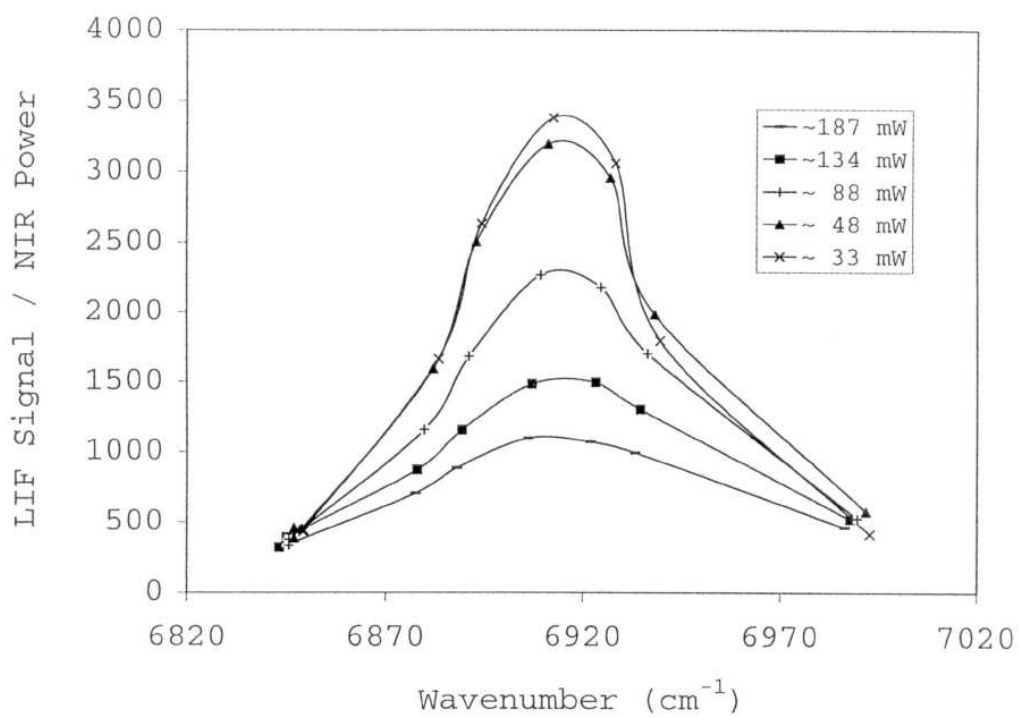


Figure 3.19: LIF signal in Figure 3.18 normalized with NIR laser power.

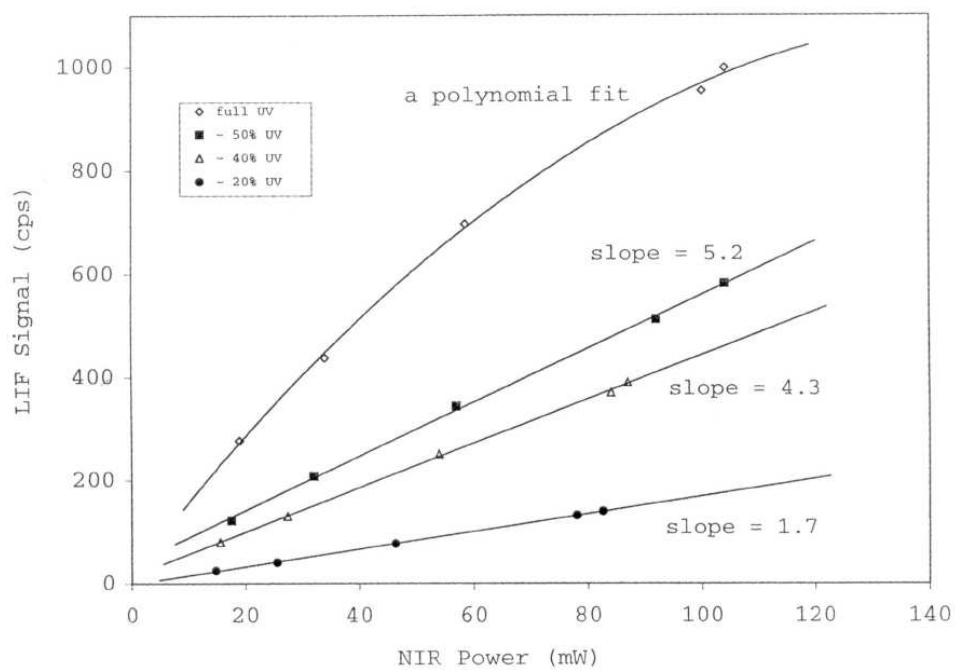


Figure 3.20: LIF signal at the  $2\nu_1$  peak as a function of the NIR and UV laser power.

observed.

The relative peak intensities of the different bands are obtained by quickly stepping the NIR frequency through the peaks of these dissociative bands. In separate experiments, band shapes for  $3\nu_1$ ,  $2\nu_1+\nu_3$  and  $2\nu_1$  are obtained by scanning the OPO wavelength in small steps over each of these bands. [For the combination band at 1599 nm, an action spectrum scanned over the entire band is yet to be obtained. Thus, the shape for this band is only available from the FTIR spectrum, which can be seen in Figure 3.8.] Linear scaling using the relative peak intensities then produces their action spectra, which are scaled to match the absorption spectra. This is shown in Figures 3.21 to 3.23. Good agreement is found. This also adds confidence to the linearity of the scaling. It is noted that at the wings of the  $2\nu_1$  band, action spectrum signals are higher than the FTIR signal. This could be due to hot band excitation/dissociation. Future experiments will scan over  $2\nu_1$  band at sufficiently low signal to ensure linearity and study possible variation in the quantum yields across this band.

Table 3.5 lists the relative intensities of these four dissociative bands from both the FTIR and action spectra. The quantum yield is calculated by dividing the action spectrum signal with the absorption intensity at peak center. Assuming the quantum yield for  $3\nu_1$  is unity, it is found that the quantum yield for  $2\nu_1+\nu_3$  is also unity within the uncertainty of this estimation, while the quantum yield for  $2\nu_1$  and the band at 1599 nm is  $0.24 \pm 0.04$  and  $0.04 +0.04/-0.02$ , respectively, at 278 K. Figure 3.24 graphically illustrates the comparison of the photodissociation strengths, i.e., product of the quantum yield and the absorption cross section, for three of these  $\text{HNO}_4$  bands at 278 K.

The pressure dependence of the quantum yields has also been investigated. Shown in Figure 3.25 is the relative quantum yield at the  $2\nu_1$  peak relative to  $3\nu_1$  at different pressures ( $3 < P < 25$  torr). The observed quantum yield is independent of pressure. The lack of significant quenching suggests that the lifetime of  $\text{HNO}_4$  excited via  $2\nu_1$  is short compared to the collisional time scale ( $\leq 10$  nsec), despite the excitation energy being essentially at threshold.

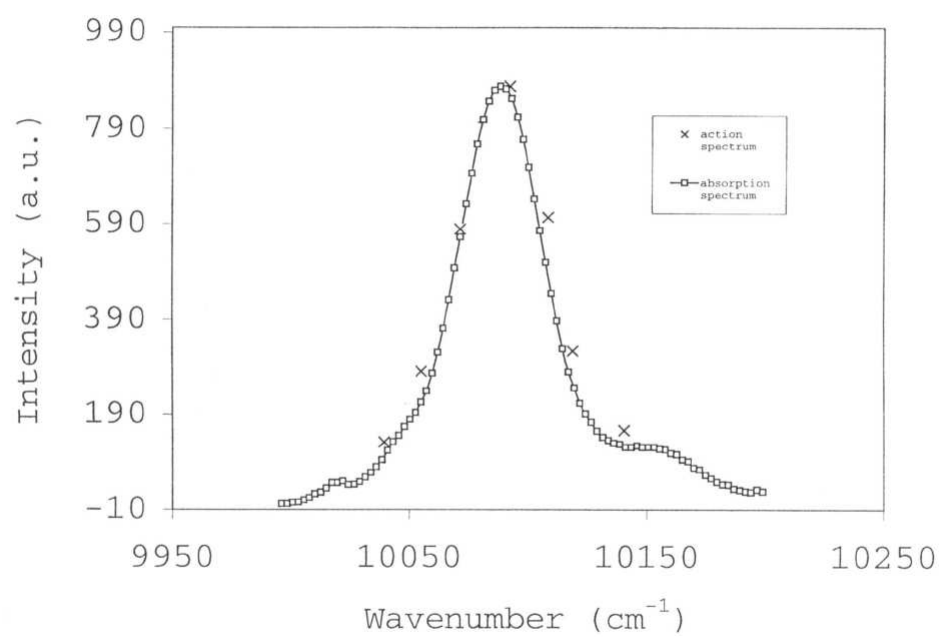


Figure 3.21: An action spectrum of  $3\nu_1$  overlaid on an absorption spectrum.

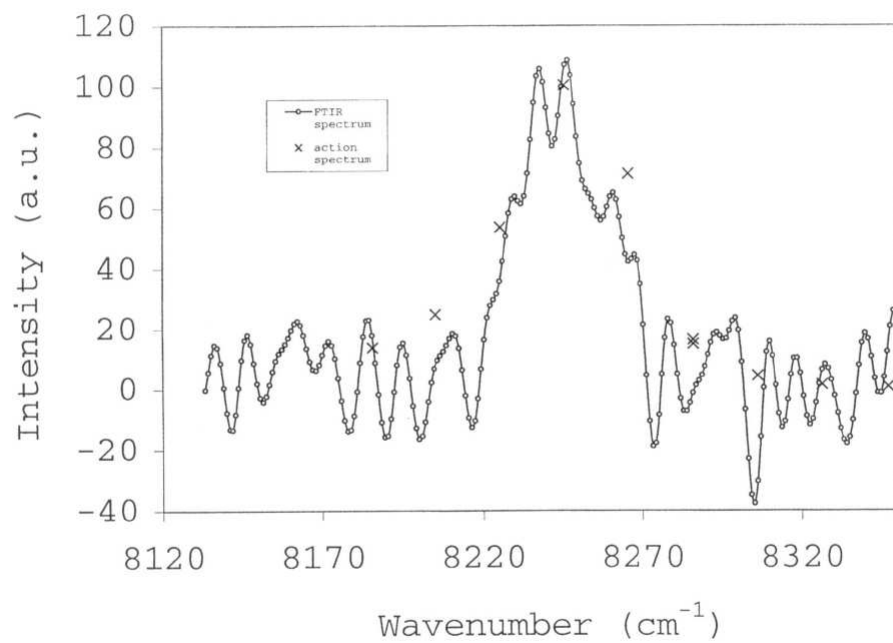


Figure 3.22: An action spectrum of  $2\nu_1 + \nu_3$  overlaid on an absorption spectrum.

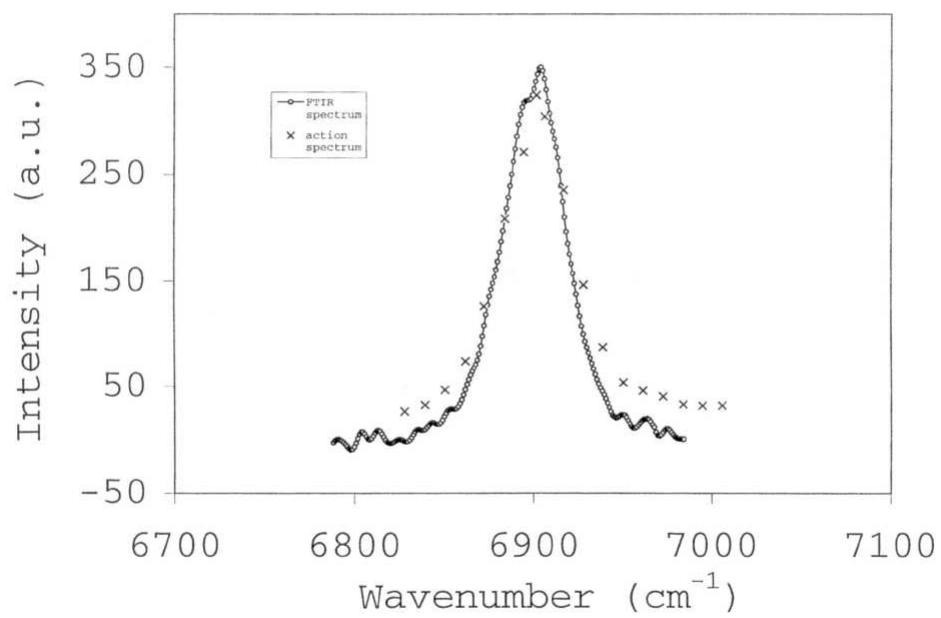


Figure 3.23: An action spectrum of  $2\nu_1$  overlaid on an absorption spectrum.

Table 3.5: Quantum yields for HNO<sub>4</sub> bands observed in action spectrum experiment.

	c.b.	$2\nu_1$	$2\nu_1 + \nu_3$	$3\nu_1$
Band Center (cm <sup>-1</sup> )	6255	6904	8242	10090
Peak Intensity Ratio from FTIR spectrum	1.46	18.13	0.38	1.00
Peak Intensity Ratio from action spectrum	0.06	4.39	0.37	1.00
Quantum Yield @278 K	0.04	0.24	0.97	1.00

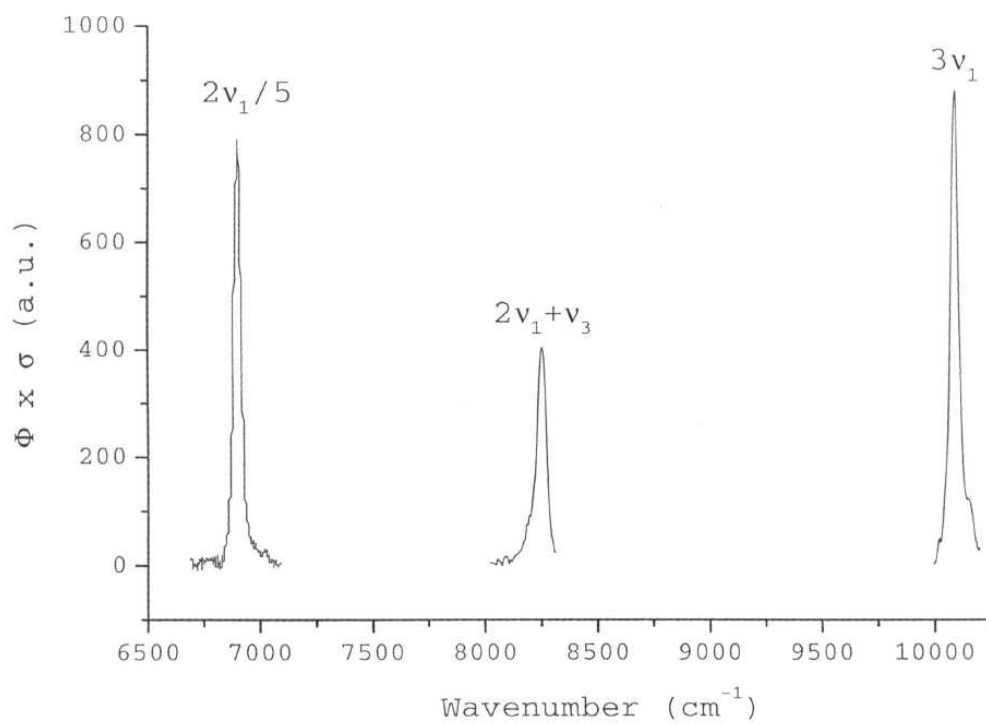


Figure 3.24: Comparison of product of the quantum yield,  $\Phi$ , and the absorption cross section,  $\sigma$ , for three  $\text{HNO}_4$  bands at 278 K. The intensity of the  $2\nu_1$  band is scaled down by a factor of 5. The band shape for  $2\nu_1$  is from an FTIR spectrum, that for  $2\nu_1+\nu_3$  is from an action spectrum, and that for  $3\nu_1$  is also from an action spectrum.

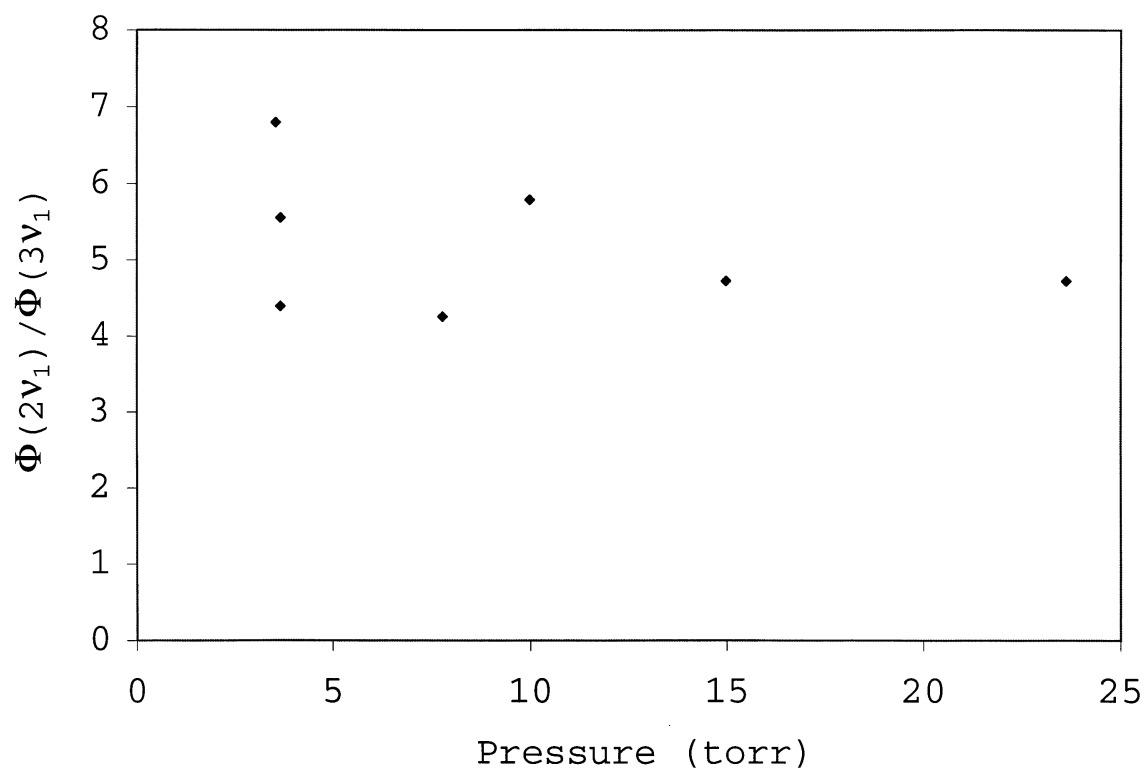


Figure 3.25: Peak-to-peak quantum yield for  $2\nu_1$  relative to  $3\nu_1$ , determined as a function of pressure.

### 3.3 Discussion and Conclusions

#### 3.3.1 Bond Energy of HOO-NO<sub>2</sub>

The observation of HNO<sub>4</sub> dissociation at wavelengths as long as 1600 nm is somewhat surprising as the dissociation threshold ( $D_0$ ) for the HOO-NO<sub>2</sub> bond in HNO<sub>4</sub> is placed at a much shorter wavelength. Previous recommendations for  $D_0$  have been based on measurements of the thermal decomposition and recombination rates for HNO<sub>4</sub> (Reaction (3.4) and (3.1)). The JPL Evaluation recommends a value of  $97 \pm 10.5$  kJ/mole for  $\Delta H_{298}$  (7), while IUPAC (International Union of Pure and Applied Chemistry) recommends 105 kJ/mole based on a larger bond formation enthalpy for HO<sub>2</sub> and a reduced value for the exothermic formation of HNO<sub>4</sub> (2). Zabel *et al.* determined  $\Delta H_{298}$  to be  $99.6 \pm 3.1$  kJ/mole and  $\Delta H_0 = 95 \pm 3$  kJ/mole (51). There is no experimental or theoretical evidence that the recombination reaction (3.1) has a potential barrier, therefore,  $D_0 \equiv \Delta U_0 = \Delta H_0$  can be assumed (51). Results from Zabel *et al.* yield a thermodynamic dissociation limit at  $1260 \pm 40$  nm. Another published work by Patrick *et al.* (31) recommends 96 kJ/mole for  $\Delta H_0$ , in good agreement with Zabel *et al.*. If we apply the same variation of  $\Delta H$  with temperature to JPL recommendation,  $\Delta H_0 = 92.4 \pm 10.5$  kJ/mole is obtained, corresponding to  $1295 \pm 140$  nm. In summary, though there exist large uncertainties, the dissociation threshold for HOO-NO<sub>2</sub> bond is placed somewhere near  $1280 \pm 100$  nm.

To account for the dissociation of HNO<sub>4</sub> beyond its thermodynamic threshold, a simple calculation, based on the thermal distribution of the vibrational and rotational energy in the ground electronic state of HNO<sub>4</sub>, is carried out. The model used in the calculation assumes that some fraction,  $C_{int}$ , of the internal energy in the HNO<sub>4</sub> molecule in its ground electronic state can supplement the photon energy, leading to dissociation:

$$\begin{aligned} \Phi &= 1 && \text{for } E(h\nu) + C_{int} \times E_{int} > D_0 \\ \Phi &= 0 && \text{for } E(h\nu) + C_{int} \times E_{int} < D_0 \end{aligned} \quad (3.13)$$

where  $\Phi$  is the quantum yield and  $C_{int} \times E_{int}$  is the available internal energy.  $E_{int}$  can be expanded such that  $C_{int} \times E_{int} = C_{vib} \times E_{vib} + C_{rot} \times E_{rot}$ , where  $C_{vib}$  and  $C_{rot}$  are the fraction of the total vibrational and rotational energy available for the dissociation, respectively.

The internal vibrational energy  $E_{vib}$  for  $\text{HNO}_4$  is calculated according to

$$E_{vib} = \frac{\sum_{s=1}^{3n-6} \theta_{vib,s}}{e^{\theta_{vib,s}/T} - 1} \quad (3.14)$$

where  $\theta_{vib,s} \equiv h\nu_s/k$ ,  $\nu_s$  is the fundamental mode of vibration,  $h$  is Planck's constant,  $k$  is Boltzmann's constant, and  $n$  is the number of nuclei in the molecule. The vibrational frequencies of the 12 fundamental modes for  $\text{HNO}_4$  are taken from Table 3.2. A calculation performed for 278 K yields  $E_{vib}$  of  $440 \text{ cm}^{-1}$  per molecule. Following the idea of Marcus in reference (24), all the vibrational energy is termed "nonfixed" and is capable of flowing into the bond to be broken. It is assumed here that all of this energy is available for dissociation, therefore,  $C_{vib} = 1$ .

A theoretical treatment employing internal rotational energy to supplement the photon energy has been previously used to explain the photodissociation of  $\text{NO}_2$  beyond its thermodynamic dissociation limit (34). In the case of  $\text{NO}_2$ , all the rovibrational energy must be considered available to explain the observed quantum yield for photodissociation. In fact, even this energy is insufficient and collisional activation of  $\text{NO}_2$  molecules excited to energies just below threshold has been suggested as the source of the extra energy (36). Using the classical formula of  $E_{rot} = 3/2 k T$  for an asymmetric top molecule,  $E_{rot}$  for  $\text{HNO}_4$  is found to be  $290 \text{ cm}^{-1}$  per molecule at 278 K. This upper limit will be quite close to the actual rotational energy given the small rotational constants of  $\text{HNO}_4$  (the rotational constants for  $\text{HNO}_4$  have been experimentally found to be:  $A = 11,994 \text{ MHz}$ ,  $B = 4665 \text{ MHz}$  and  $C = 3397 \text{ MHz}$  (45)). The optimized structure of  $\text{HNO}_4$  consists of a nearly planar heavy atom framework with the hydrogen atom rotated almost perpendicular to this plane (see Figure 3.2) (25). It is proposed that rotation along the major axis of  $\text{HNO}_4$  will not likely contribute significantly to the rupture of the  $\text{HOO-NO}_2$  bond; however, rotational energies from those two rotational degrees of freedom possessing the larger moments of inertia can couple into the reaction coordinate (i.e.,  $\nu_6$ , see Table 3.2). Therefore, it is assumed that two-thirds of the internal rotational energy contributes to the dissociation, i.e.,  $C_{rot} = 2/3$ . This allows a total of  $630 \text{ cm}^{-1}$  internal energy ( $C_{int} \times E_{int}$ ) available for breaking O-N bond at 278 K. It is also noted that conservation of angular momentum can present some barrier to intramolecular energy transfer. As a result, only the centrifugal energy from these two contributing rotations may be available (see a discussion by Marcus in reference (24)).

Based on the Boltzmann distribution, the fraction of  $\text{HNO}_4$  molecules that will dissociate

upon absorption of photon  $h\nu$ , i.e., the quantum yield  $\Phi$ , can be determined according to

$$\Phi = e^{(h\nu - D_0)/C_{int} \times E_{int}} \quad (h\nu < D_0). \quad (3.15)$$

Using the above estimated  $C_{int} \times E_{int}$  and  $\Phi$  measured for  $2\nu_1$ , the dissociation threshold,  $D_0$ , is calculated to be  $\sim 1280$  nm.  $D_0$  determined from  $\Phi$  for the 1599 nm band is 1205 nm, though the latter is quite uncertain due to the large uncertainty in  $\Phi$  (a factor of 2). Generally speaking, the above model explains the observed quantum yield within the range of  $D_0$  value recommended in literature.

The importance of internal energy for  $\Phi(2\nu_1)$  suggests that the photodissociation rate of  $\text{HNO}_4$  will be quite temperature sensitive. The above model predicts a temperature-dependent quantum yield for partially dissociative bands since less internal energy will be available for dissociation at lower temperature. For example, with  $D_0 = 1280$  nm ( $\sim 7810$   $\text{cm}^{-1}$ ),  $E_{int}$  will be reduced to  $460$   $\text{cm}^{-1}$  at 230 K, and the quantum yields for  $2\nu_1$  will drop to 0.14. Table 3.6 shows the predicted quantum yields of  $2\nu_1$  and 1599 nm band vs. temperature assuming  $D_0 = 1280$  nm. Temperature dependence experiments are yet to be performed to test this model, but will be a focus of future work.

### 3.3.2 Atmospheric Significance

The NIR photolysis rate of  $\text{HNO}_4$  at stratospheric temperatures (assumed to be 230 K here) is calculated according to Eq. (3.6) using the cross sections and quantum yields obtained in this study, and the solar flux from Neckel *et al.* (28) and Arvesen *et al.* (1). The results are shown in Table 3.7. The dissociation of the  $3\nu_1$ ,  $2\nu_1 + \nu_3$ ,  $2\nu_1$  and 1599 nm bands yield a photolysis rate of  $\sim 6.8 \times 10^{-6}$   $\text{s}^{-1}$  at 230 K (including a planetary albedo of 0.3). This accounts well for the missing  $\text{HO}_x$  source proposed by Wennberg *et al.* (50). A similar calculation carried out at 278 K shows a sum rate of  $\sim 1.0 \times 10^{-5}$   $\text{s}^{-1}$  for the  $\text{HNO}_4$  NIR photolysis.

The dissociation of  $2\nu_1$  alone contributes more than 65% of the total NIR photolysis rate of  $\text{HNO}_4$  at 278 K and more than 50% at 230 K. The atmosphere is essentially transparent at the  $2\nu_1$  absorption feature, as illustrated in Figure 3.26. This is an atmospheric transmission spectrum obtained on the top of Mauna Kea, Hawaii. The location of the  $2\nu_1$  band of  $\text{HNO}_4$  is marked on the spectrum. The absorption is due to  $2\nu_{\text{OH}}$  of water, in this case, with a column of 1.2 mm precipital  $\text{H}_2\text{O}$ .

Table 3.6: Temperature-dependent quantum yields predicted for  $2\nu_1$  and 1599 nm.

T (K)	$\Phi(2\nu_1)$	$\Phi(1599 \text{ nm})$
200	0.081	0.013
210	0.098	0.019
220	0.116	0.025
230	0.136	0.033
240	0.156	0.042
250	0.176	0.052
260	0.200	0.063
270	0.218	0.074
280	0.239	0.087
290	0.260	0.100
300	0.281	0.114

Table 3.7: NIR Photolysis Rate of HNO<sub>4</sub> at 230 K.

	c.b.	$2\nu_1$	$2\nu_1 + \nu_3$	$3\nu_1$
Band Center (cm <sup>-1</sup> )	6255	6904	8242	10090
Intensity (10 <sup>-20</sup> cm <sup>2</sup> molec <sup>-1</sup> cm <sup>-1</sup> )	3.4	61	2.2	3.8
Quantum Yield @230 K	0.033	0.136	1.0	1.0
Solar Flux (10 <sup>13</sup> photons cm <sup>-2</sup> s <sup>-1</sup> / cm <sup>-1</sup> )	3.4	3.3	3.9	4.0
Photolysis Rate (10 <sup>-6</sup> s <sup>-1</sup> ) @230 K	0.04	2.8	0.9	1.5

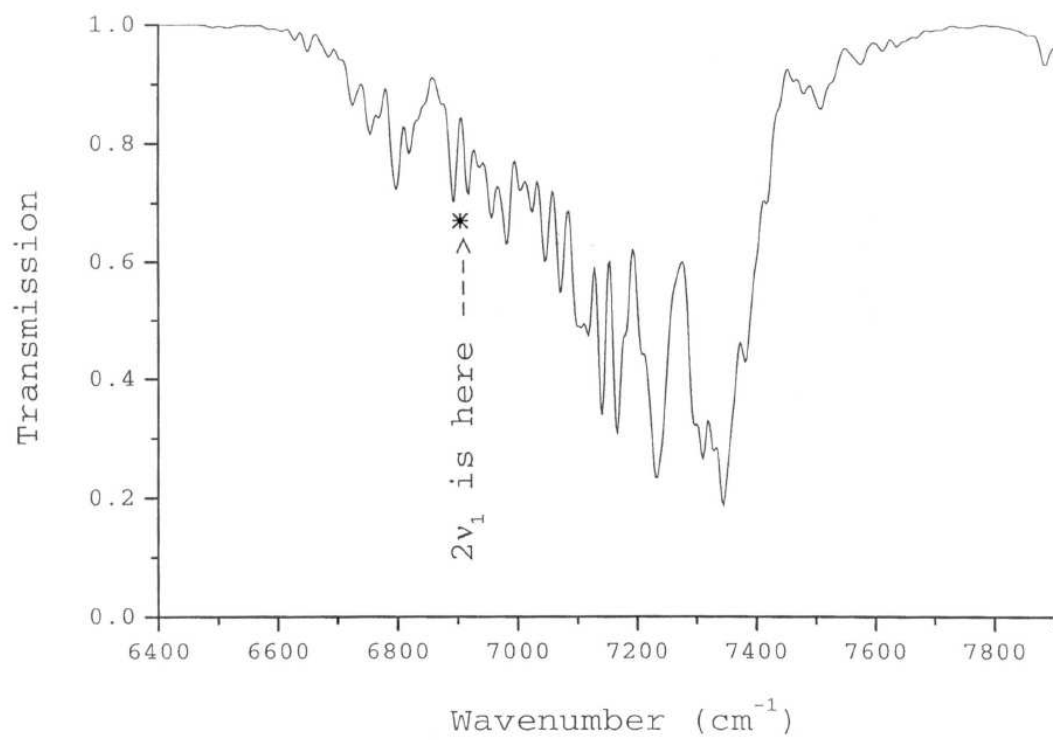


Figure 3.26: Atmospheric transmission spectrum at the top of Mauna Kea, Hawaii. The location of the HNO<sub>4</sub> 2ν<sub>1</sub> band is marked.

The 24-hour averaged atmospheric loss rates of  $\text{HNO}_4$  due to thermal decomposition, UV photolysis, and NIR photolysis are shown in Figure 3.27. This calculation is performed for equinox conditions at  $60^\circ$  N. The UV photolysis (R. J. Salawitch, personal communication) is based on UV cross sections from the JPL Panel Recommendation (7). The temperature-dependence of the  $\text{HNO}_4$  quantum yields is included in the NIR photolysis calculation. It can be seen that the NIR photodissociation processes observed in this study shortens the lifetime of  $\text{HNO}_4$  under these conditions by more than a factor of two for regions between 8 and 26 km.

At lower latitudes, the relative importance of the NIR photolysis will be reduced due to the significantly higher UV intensity. This is demonstrated in Figure 3.28, where the contribution of NIR photolysis to the total  $\text{HNO}_4$  photolysis is estimated for equinox conditions at two different latitudes. At  $60^\circ$  N,  $\sim 70\%$  of  $\text{HNO}_4$  photolysis at 20 km is due to NIR while this fraction drops to  $\sim 50\%$  at  $30^\circ$  N. The decrease in the relative importance of NIR photolysis at lower latitudes is even more pronounced at lower altitudes where this process dominates the photolysis of  $\text{HNO}_4$ .

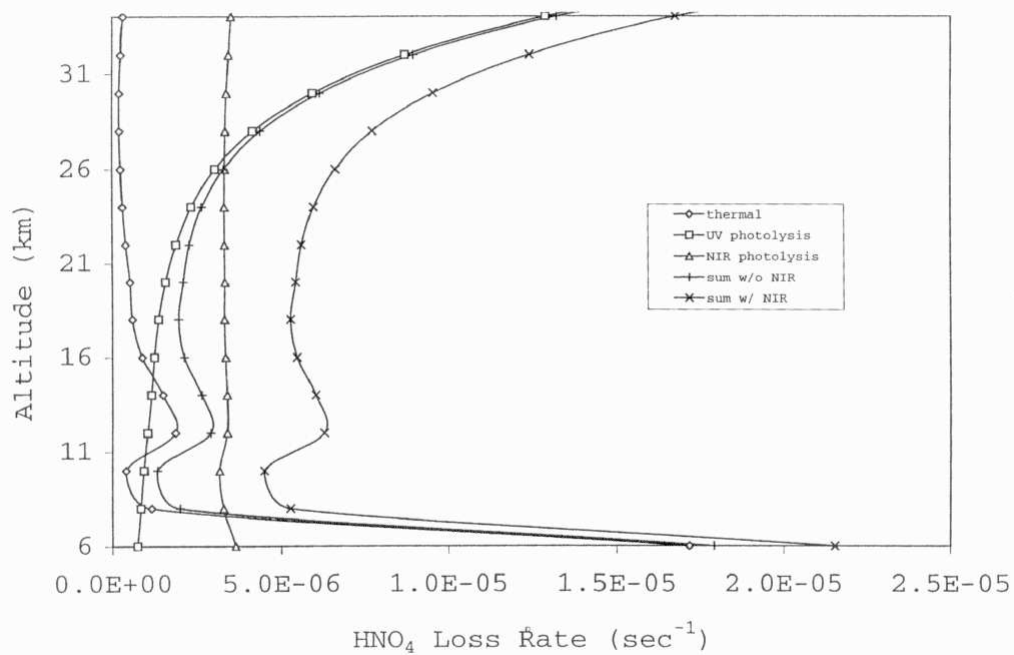


Figure 3.27: The 24-hour averaged loss rates for HNO<sub>4</sub>. The calculation is conducted at equinox for a latitude of 60° N.

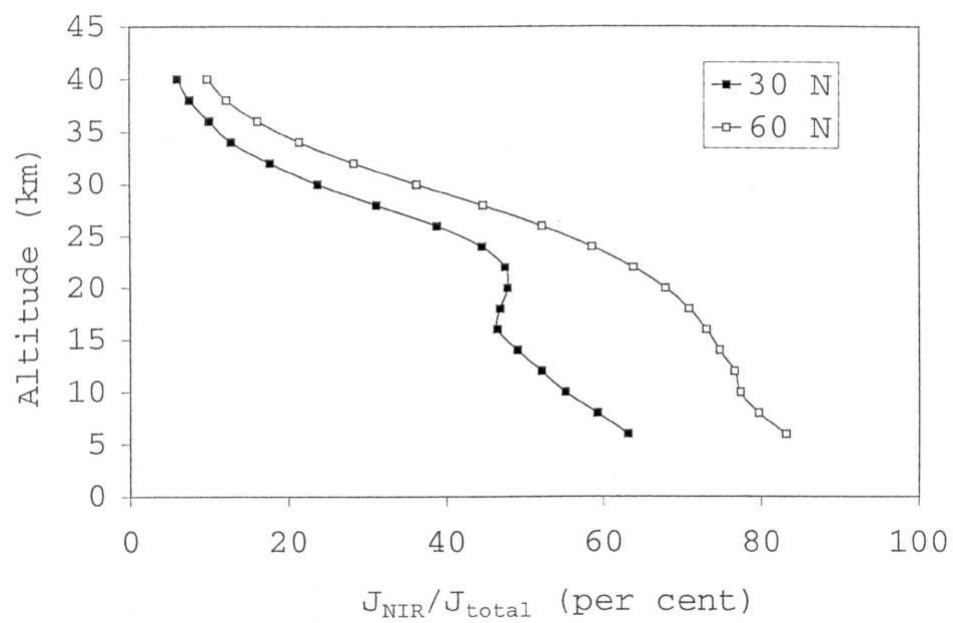


Figure 3.28: Comparison of the relative importance of the NIR photolysis of  $\text{HNO}_4$  at two different latitudes.

## Bibliography

- [1] Arvesen, J. C., R. N. Griffin, Jr., and B. D. Pearson, Jr., “Determination of extraterrestrial solar spectral irradiance from a research aircraft”, *Applied Optics*, 8 (1969) 2215-2232.
- [2] Atkinson, R, D. L. Baulch, R. A. Cox, R. F. Hampson, Jr., J. A. Kerr, M. J. Rossi, and J. Troe, “Evaluated kinetic, photochemical and heterogeneous data for atmospheric chemistry: supplement V”, *J. Phys. Chem. Ref. Data*, 26 (1997) 521-1011.
- [3] Barnes, R. J., M. Lock, J. Coleman, and A. Sinha, “Observation of a new absorption band of HOBr and its atmospheric implications”, *J. Phys. Chem.*, 100 (1996) 453-457.
- [4] Brown, S. S., R. W. Wilson, and A. R. Ravishankara, “Absolute intensities for third and fourth overtone absorptions in HNO<sub>3</sub> and H<sub>2</sub>O<sub>2</sub> measured by cavity ring down spectroscopy”, *J. Phys. Chem.*, 104 (2000), 4976-4983.
- [5] Brune, W. H., D. Tan, I. F. Faloona, L. Jaegle, D. J. Jacob, B. G. Heikes, J. Snow, Y. Kondo, R. Shetter, G. W. Sachse, B. Anderson, G. L. Gregory, S. Vay, H. B. Singh, D. D. Davis, J. H. Crawford, and D. R. Blake, “OH and HO<sub>2</sub> chemistry in the north atlantic free troposphere”, *Geophys. Res. Lett.*, 26 (1999) 3077-3080.
- [6] Cox, R. A., and R. Patrick, “Kinetics of the reaction HO<sub>2</sub> + NO<sub>2</sub> ( + M ) = HO<sub>2</sub>NO<sub>2</sub> using molecular modulation spectroscopy”, *Int. J. Chem. Kinetics*, XI (1979) 635-648.
- [7] DeMore, W. B., S. P. Sander, D. M. Golden, R. F. Hampson, M. J. Kurylo, C. J. Howard, A. R. Ravishankara, C. E. Kolb, and M. J. Molina, *Chemical kinetics and photochemical data for use in stratospheric modeling*, JPL Publication 97-4, NASA/JPL, Pasadena, California, 1997.
- [8] Dieke, G. H., and H. M. Crosswhite, “The ultraviolet band of OH: fundamental data”, *J. Quant. Spectrosc. Radiat. Transfer*, 2 (1962) 97-199.
- [9] Donaldson, D. J., G. J. Frost, K. H. Rosenlof, A. F. Tuck, and V. Vaida, “Atmospheric

- radical production by excitation of vibrational overtones via absorption of visible light”, *Geophys. Res. Lett.*, 24 (1997) 2651-2654.
- [10] Donaldson, D. J., J. J. Orlando, S. Amann, G. S. Tyndall, R. J. Proos, B. R. Henry, and V. Vaida, “Absolute intensities of nitric acid overtones”, *J. Phys. Chem. A*, 102 (1998) 5171-5174.
- [11] Douketis, C., and J. P. Reilly, “High resolution vibrational overtone spectroscopy of hydrogen peroxide in the  $\Delta\nu=4$  region”, *J. Chem. Phys.*, 91 (1989) 5239-5250.
- [12] Faloon, I., D. Tan, W. H. Brune, L. Jaegle, D. J. Jacob, Y. Kondo, M. Koike, R. Chatfield, R. Pueschel, G. Ferry, G. Sachse, S. Vay, B. Anderson, J. Hannon, and H. Fuelberg, “Observations of HO<sub>x</sub> and its relationship with NO<sub>x</sub> in the upper troposphere during SONEX”, *J. Geophys. Res.*, 105 (2000) 3771-3783.
- [13] Fono, L., D. J. Donaldson, R. J. Proos, and B. R. Henry, “OH overtone spectra and intensities of pernitric acid”, *Chem. Phys. Lett.*, 311 (1999) 131-138.
- [14] Friedl, R. R., R. D. May, and G. Duxbury, “The  $\nu_6$ ,  $\nu_7$ ,  $\nu_8$ , and  $\nu_{10}$  bands of HO<sub>2</sub>NO<sub>2</sub>”, *J. Molec. Spectrosc.*, 165 (1994) 481-493.
- [15] Goldman, A., F. J. Murcray, R. D. Blatherwick, J. J. Kusters, F. H. Murcray, and D. G. Murcray, “New spectral features of stratospheric trace gases identified from high-resolution infrared balloon-borne and laboratory spectra”, *J. Geophys. Res.*, 94 (1989) 14945-14955.
- [16] Graham, R. A., A. M. Winer, and J. N. Pitts Jr., “Temperature dependence of the unimolecular decomposition of pernitric acid and its atmospheric implications”, *Chem. Phys. Lett.*, 51 (1977) 215-220.
- [17] Graham, R. A., A. M. Winer, and J. N. Pitts, Jr., “Ultraviolet and infrared absorption cross sections of gas phase HNO<sub>4</sub>”, *Geophys. Res. Lett.*, 5 (1978) 909-911.
- [18] Hanson, D. R., and A. R. Ravishankara, “Heterogeneous chemistry of bromine species in H<sub>2</sub>SO<sub>4</sub>”, *Geophys. Res. Lett.*, 22 (1995) 385-388.
- [19] Jaegle, L., D. J. Jacob, W. H. Brune, J. Faloon, D. Tan, B. G. Heikes, Y. Kondo, G. W. Sachse, B. Anderson, G. L. Gregory, H. B. Singh, R. Pueschel, G. Ferry, D.

- R. Blake, and R. E. Shetter, "Photochemistry of  $\text{HO}_x$  in the upper troposphere at northern midlatitudes", *J. Geophys. Res.*, 105 (2000) 3877-3892.
- [20] Kenley, R. A., P. L. Trevor, and B. Y. Lan, "Preparation and thermal decomposition of pernitric acid ( $\text{HOONO}_2$ ) in aqueous media", *J. Am. Chem. Soc.*, 103 (1981) 2203-2206.
- [21] Kirmse, B., A. Delon, and R. Jost, " $\text{NO}_2$  absorption cross section and its temperature dependence", *J. Geophys. Res.*, 102 (1997) 16,089-16,098.
- [22] MacLeod, H., G. P. Smith, and D. M. Golden, "Photodissociation of pernitric acid ( $\text{HNO}_4$ ) at 248 nm", *J. Geophys. Res.*, 93 (1988) 3813-3823.
- [23] May, R. D., and R. R. Friedl, "Integrated band intensities of  $\text{HNO}_4$  at 220 K", *J. Quant. Spectrosc. Radiant. Transfer*, 50 (1993) 257-266.
- [24] Marcus, R. A., "Unimolecular dissociations and free radical recombination reactions", *J. Chem. Phys.*, 20 (1952) 359-364.
- [25] Miller, C. E., J. I. Lynton, D. M. Keevil, and J. S. Francisco, "Dissociation pathways of peroxyacetyl nitrate (PAN)", *J. Phys. Chem. A*, 103 (1999) 11451-11459.
- [26] Molina, L. T., and M. J. Molina, "UV absorption cross sections of  $\text{HNO}_4$  vapor", *J. Photochem.*, 15 (1981) 97-108.
- [27] Morel, O., R. Simonaitis, and J. Heicklen, "Ultraviolet absorption spectra of  $\text{HNO}_4$ ,  $\text{CCl}_3\text{O}_2\text{NO}_2$ ,  $\text{CCl}_2\text{FO}_2\text{NO}_2$ , and  $\text{CH}_3\text{O}_2\text{NO}_2$ ", *Chem. Phys. Lett.*, 73 (1980) 38-42.
- [28] Neckel, H., and D. Labs, "The solar radiation between 3,300-Å and 12,500-Å", *Solar Phys.*, 90 (1984) 205-258.
- [29] Niki, H., P. D. Maker, C. M. Savage, and L. P. Breitenbach, "Fourier transform IR spectroscopy observation of pernitric acid formed via  $\text{HOO} + \text{NO}_2 \rightarrow \text{HOONO}_2$ ", *Chem. Phys. Lett.*, 45 (1977) 564-566.
- [30] Osterman, G. B., R. J. Salawitch, B. Sen, G. C. Toon, J. J. Margitan, J.-F. Blavier, and P. O. Wennberg, "Measurements and model calculations of  $\text{HNO}_4$ : Implications for  $\text{HO}_x$ ", 1999 AEAP Meeting Abstract, [http://hyperion.gsfc.nasa.gov/aeap/Osterman\\_G.html](http://hyperion.gsfc.nasa.gov/aeap/Osterman_G.html).

- [31] Patrick, R., and D. M. Golden, "Third-order rate constants of atmospheric importance", *Int. J. Chem. Kinetics*, 15 (1983) 1189-1227.
- [32] Penner, J. E., D. H. Lsiter, D. J. Griggs, D. J. Dokken, and M. McFarland (Eds.), "Intergovernmental panle on climate change, aviation and the global atmosphere", Cambridge University Press, New York, 1999.
- [33] Phillips, J. A., J. J. Orlando, G. S. Tyndall, and V. Vaida, "Integrated intensities of OH vibrational overtones in alcohols", *Chem. Phys. Lett.*, 296 (1998) 377-383.
- [34] Pitts, J. N. Jr., J. H. Sharp, and S. I. Chan, "Effects of wavelength and temperature on primary processes in the photolysis of nitrogen dioxide and a spectroscopic-photochemical determination of the dissociation energy", *J. Chem. Phys.*, 42 (1964) 3655-3662.
- [35] Rinsland, C. P., R. Zander, C. B. Farmer, R. H. Norton, L. R. Brown, J. M. Russell, and J. H. Peel, "Evidence for the presence of the  $802.7\text{-cm}^{-1}$  band Q branch of  $\text{HNO}_4$  in high-resolution solar absorption-spectra of the stratosphere", *Geophys. Res. Lett.*, 13 (1986) 761-764.
- [36] Roehl, C. M., J. J. Orlando, G. S. Tyndall, R. E. Shetter, G. J. Vazques, C. A. Cantrell, and J. G. Calvert, "Temperature dependence of the quantum yields for the photolysis of  $\text{NO}_2$  near the dissociation limit", *J. Phys. Chem.*, 98 (1994) 7837-7843.
- [37] Roehl, C. M., T. L. Mazely, R. R. Friedl, Y. Li, J. S. Francisco, and S. P. Sander, " $\text{NO}_2$  quantum yield from the 248 nm photodissociation of peroxyntic acid ( $\text{HNO}_4$ )", submitted to *J. Phys. Chem.*, 2000.
- [38] Salawitch, R. J., S. C. Wofsy, P. O. Wennberg, R. C. Cohen, J. G. Anderson, D. W. Fahey, R. S. Gao, E. R. Keim, E. L. Woodbridge, R. M. Stimpfle, J. P. Koplw, D. W. Kohn, C. R. Webster, R. D. May, L. Pfister, E. W. Gottlieb, H. A. Michelsen, G. K. Yue, J. C. Wilson, C. A. Brock, H. H. Jonsson, J. E. Dye, D. Baumgardner, M. H. Proffitt, M. Loewenstein, J. R. Podolske, J. W. Elkins, G. S. Dutton, E. J. Hintsa, A. E. Dessler, E. M. Weinstock, K. K. Kelly, K. A. Boering, B. C. Daube, K. R. Chan, and S. W. Bowen, "The distribution of hydrogen, nitrogen, and chlorine radicals in

- the lower stratosphere: Implications for changes in O<sub>3</sub> due to emission of NO<sub>y</sub> from supersonic aircraft”, *Geophys. Res. Lett.*, 21 (1994) 2547-2550.
- [39] Sen, B., G. C. Toon, G. B. Osterman, J.-F. Blavier, J. J. Margitan, R. J. Salawitch, and G. K. Yue “Measurements of reactive nitrogen in the stratosphere”, *J. Geophys. Res.*, 103 (1998) 3571-3585.
- [40] Singer, R. J., J. N. Crowley, J. P. Burrows, W. Schneider, and G. K. Moortgat, “Measurement of the absorption cross-section of peroynitric acid between 210 and 330 nm in the range 253-298 K”, *J. Photochem. Photobiol. A Chemistry*, 48 (1989) 17-32.
- [41] Singh, H. B., A. M. Thompson, and H. Schlager, “SONEX airborne mission and coordinated POLINAT-2 activity: overview and accomplishments”, *Geophys. Res. Lett.*, 26 (1999) 3053-3056.
- [42] Sinha, A., R. L. Vander Wal, and F. F. Crim, “State-resolved unimolecular reactions: the vibrational overtone initiated decomposition of nitric acid”, *J. Chem. Phys.*, 92 (1990) 401-410.
- [43] Solomon, S., “Progress towards a quantitative understanding of Antarctic ozone depletion”, *Nature*, 347 (1990) 347-354.
- [44] Stern, S. A., J. T. Mullhaupt, and W. B. Kay, “The physicochemical properties of pure nitric acid”, *Chem. Reviews*, 60 (1960), 185-207.
- [45] Suenram, R. D., F. J. Lovas, and H. M. Pickett, “The microwave-spectrum and molecular-conformation of peroynitric acid (HOONO<sub>2</sub>)”, *J. Mol. Spectrosc.*, 116 (1986) 406-421.
- [46] Thompson, A. M., H. B. Singh, and H. Schlager, “Introduction to special section: subsonic assessment ozone and nitrogen oxide experiment (SONEX) and pollution from aircraft emissions in the north atlantic flight corridor (POLINAT 2)”, *J. Geophys. Res.*, 105 (2000) 3595-3603.
- [47] Watson, R. T., S. P. Sander, and Y. L. Yung, “Pressure and temperature dependence kinetics study of the NO + BrO → NO<sub>2</sub> + Br reaction: Implications for stratospheric bromine photochemistry”, *J. Phys. Chem.*, 83 (1979) 2936-2944.

- [48] Wennberg, P. O., R. C. Cohen, R. M. Stimpfle, J. P. Koplow, J. G. Anderson, R. J. Salawitch, D. W. Fahey, E. L. Woodbridge, E. R. Keim, R. S. Gao, C. R. Webster, R. D. May, D. W. Toohey, L. M. Avallone, M. H. Proffitt, M. Loewenstein, J. R. Podolske, K. R. Chan, and S. C. Wofsy, "Removal of stratospheric O<sub>3</sub> by radicals: In situ measurements of OH, HO<sub>2</sub>, NO, NO<sub>2</sub>, ClO, and BrO", *Science*, 266 (1994) 398-404.
- [49] Wennberg, P. O., R. C. Cohen, N. L. Hazen, L. B. Lapson, N. T. Allen, T. F. Hanisco, J. F. Oliver, N. W. Lanham, J. N. Demusz, and J. G. Anderson, "Aircraft-borne, laser-induced fluorescence instrument for the *in situ* detection of hydroxyl and hydroperoxyl radicals", *Rev. Sci. Instrum.*, 65 (1994) 1858-1876.
- [50] Wennberg, P. O., R. J. Salawitch, D. J. Donaldson, T. F. Hanisco, E. J. Lanzendorf, K. K. Perkins, S. A. Lloyd, V. Vaida, R. S. Gao, E. J. Hinsta, R. C. Cohen, W. H. Swartz, T. L. Kusterer, and D. E. Anderson, "Twilight observations suggest unknown sources of HO<sub>x</sub>", *Geophys. Res. Lett.*, 26 (1999) 1373-1376.
- [51] Zabel, F., "Unimolecular decomposition of peroxy nitrates", *Zeitschrift fur Physikalische Chemie*, 188 (1995) 119-142.
- [52] Zhang, H., C. M. Roehl, S. P. Sander, and P. O. Wennberg, "Intensity of the second and third OH overtones of H<sub>2</sub>O<sub>2</sub>, HNO<sub>3</sub>, and HNO<sub>4</sub>", *J. Geophys. Res.*, 105 (2000) 14593-14598.
- [53] Zumwalt, L. R., and P. A. Giguere, "The infra-red bands of hydrogen peroxide at λ9720 and the structure and torsional oscillation of hydrogen peroxide", *J. Chem. Phys.*, 9 (1941) 458-462.